

Synthetic Aperture Radar Discrimination of Diffuse and Specular Target Returns

by

Gilbert Leung

Submitted to the Department of Electrical Engineering and Computer Science
in Partial Fulfillment of the Requirements for the Degrees of

Master of Engineering in Electrical Engineering and Computer Science

and

Bachelor of Science in Electrical [Computer] Science and Engineering

at the

Massachusetts Institute of Technology

May 1997
[June 1997]

Student received
B.S. in Electrical
Engineering in
February 1997

© Massachusetts Institute of Technology 1997. All rights reserved.

Author.....
Department of Electrical Engineering and Computer Science
March 7, 1997

Certified by.....
Jeffrey H. Shapiro
Professor of Electrical Engineering
Thesis Supervisor

Accepted by.....
Arthur C. Smith
Chairman, Departmental Committee on Graduate Theses

MASSACHUSETTS INSTITUTE
OF TECHNOLOGY

MAR 21 1997

LIBRARIES

Synthetic Aperture Radar Discrimination of Diffuse and Specular Target Returns

by

Gilbert Leung

Submitted to the Department of Electrical Engineering and Computer Science
on March 7, 1997, in Partial Fulfillment of the
Requirements for the Degrees of
Master of Engineering in Electrical Engineering and Computer Science
and
Bachelor of Science in Electrical [Computer] Science and Engineering

Abstract

Synthetic aperture radars (SARs) provide the coverage rate and all-weather operability needed for wide-area surveillance. SAR-based automatic target recognition (ATR) systems need fast and effective discriminators to suppress vast amounts of natural clutter from, while admitting the much more limited set of man-made object data to, their classification processors. Recent research, using mm-wave SAR data, has demonstrated that multi-resolution processing offers a useful discriminant in this regard. Other work, with ultra-wide-band foliage-penetrating SAR data, has shown that adaptive-resolution imaging can exploit the aspect-dependent reflectivity of man-made objects. Neither these studies, nor other related works, have taken a principled approach—one based on the physical characteristics of the reflecting surfaces and SAR operation—to multi-resolution SAR image formation and optimal target detection. The present thesis is a first step toward such a fundamental assessment.

Using physical optics formalism, we consider multi-resolution SAR image formation for a 1-D, continuous-wave, down-looking sensor. We find that the carrier-to-noise ratios (CNRs) for diffuse (natural clutter) and specular (man-made objects) reflectors have different multi-resolution signatures. In particular, a diffuse reflector and a specular reflector of the same size have identical normalized CNRs when their SAR returns are processed over the full dwell time. However, these reflectors show substantially different behavior when processed over shorter time intervals. In addition, the “broad-side flash” phenomenon is clearly present in our specular CNR analysis.

Two relevant target detection problems are examined and discussed in detail. We see that the fundamental differences in the reflection behaviors of specular and diffuse targets directly impact the structure and performance of their Neyman-Pearson optimal detectors.

Thesis Supervisor: Jeffrey H. Shapiro
Title: Professor of Electrical Engineering

Acknowledgments

After a year and a half of working on this research problem, it is a great delight to be able to archive my work in this document and to express my gratitude for the people who made this possible.

First, I am most indebted to my thesis supervisor Prof. Jeff Shapiro for his continual motivation and patience with me whenever I was stymied. His guidance since the very beginning of our relationship has been extremely helpful. My gradual learning of the proper methodology for good scientific research owes much to his strong analytical power and clarity of thought.

Second, I am very grateful to the Air Force Office of Scientific Research that has sponsored my research under Grant F49620-93-1-0604.

I would like to thank my advisor, Dr. Marija Ilíc, who has given me tremendous support on a personal level over my past 5 years in school.

Next is my officemate, Jeff Bounds, whose words of wisdom often enlighten me, and whose witty yet not-so-benign humor never leaves me bored in our windowless office.

In addition, I would never have “made it” this far without my friends: Garlen Leung, Seung Jae Lee, Sarah Winslade, Chee-Kian Ooi, Carol Foltz, Katerina Nguyen, Marek Zebrowski, Petra Chong, Derrick Chen, Sandy Tsao, and Henry Wong. They were a significant influence in my personal development and self-improvement at various points of my life. More importantly, they have been my source of happiness.

Last but not the least, I would like to thank my sisters Winnie and Wendy, and my parents who have taken good care of me. I am especially grateful to my parents, to whom this thesis is dedicated, for sacrificing much to have come to this country to give their children better educational opportunities.

To my parents ...

Contents

- 1 Introduction** **11**
- 1.1 Motivation 11
- 1.2 Basic 1-D SAR Principles 13
- 1.3 Thesis Outline 15

- 2 Radar System Model** **17**
- 2.1 Radar Model 17
- 2.1.1 Radar Motion 17
- 2.1.2 Radar Transmitter 18
- 2.1.3 Propagation to Target Region 19
- 2.1.4 Target Model 20
- 2.1.5 Receiver Model 21
- 2.2 Target Model 23
- 2.2.1 Multiplicative Model 23
- 2.2.2 General Linear Model 27

- 3 Target Signatures and Returns** **28**
- 3.1 Uniform Clutter 28
- 3.2 Finite-size Diffuse Target 29
- 3.3 Specular Mirror 31
- 3.3.1 Target Return (Special Case: No Curvature, Large Mirror) 33
- 3.3.2 Target Return (General Case) 35
- 3.3.3 Target Return Frequency and Energy 36
- 3.4 Multiple-bounce Reflectors 37
- 3.4.1 Right-angled Trihedral 37
- 3.4.2 Right-angled Dihedral 39

4	Synthetic Aperture Radar and Multi-resolution Processing	42
4.1	Conventional SAR Processing	42
4.2	Multi-resolution Processing	45
4.3	Target Multi-resolution Signatures	47
4.3.1	A General Resolution Calculation	48
4.3.2	MR Signature Comparison: Variations across Targets	48
4.3.3	MR Signature Comparison: Variations due to Target Geometry	52
4.3.4	Summary	58
5	Target Detection Problems	59
5.1	Detection of a Specular Mirror in Uniform Clutter	59
5.1.1	Idealized Binary Hypothesis Test	59
5.1.2	Optimal Processor	61
5.1.3	Conventional Processor: Full-dwell-time Imager	70
5.1.4	Adaptive (Optimized) Multi-resolution Processor	75
5.2	Detection of a Diffuse Target	79
5.2.1	Idealized Binary Hypothesis Test	79
5.2.2	Optimal Processor	79
5.2.3	Adaptive (Optimized) Multi-resolution Imager	89
5.2.4	Conventional Processor: Full-dwell-time Imager	93
5.3	Summary	96
6	Conclusion	98
6.1	Directions for Future Work	98
A	Gaussian-Schell Model	100
B	Statistics for a Finite Sum of Exponential Random Variables	103

List of Figures

- 1-1 Geometry of radar operation 13
- 1-2 Linear approximation to motion-induced Doppler frequency chirp 15

- 2-1 IF Signal model 21
- 2-2 Radar system block diagram 23
- 2-3 Input-output relation for a multiplicative target model 24
- 2-4 Rough surface gives diffuse reflections 25
- 2-5 Smooth surface gives specular reflections 26

- 3-1 Geometry of the specular mirror 31
- 3-2 A tilted mirror offsets the broadside flash and the chirp center 34
- 3-3 The radar return from a tilted target includes a shifted portion of the Doppler frequency chirp 36
- 3-4 Triple-bounce effect of a trihedral 37
- 3-5 Scattering gain pattern 38
- 3-6 Double-bounce and single-bounce effects of a dihedral 39

- 4-1 Optimal receiver for estimating the target’s location 43
- 4-2 Conventional-Imager Receiver Structure 44
- 4-3 Resolution and peak CNR of a point scatterer as a function of integration duration 46
- 4-4 High noise level corrupts location estimate 47
- 4-5 MR signatures for four target models: diffuse target, specular mirror ($R_x \rightarrow \pm\infty$), trihedral, and dihedral ($\theta = \pi/4$) 51
- 4-6 MR signatures of diffuse targets with different dimensions 52
- 4-7 MR signatures: resolution of specular mirrors with different dimensions and curvatures 53
- 4-8 MR signatures: shift of specular mirrors with different dimensions and curvatures 56
- 4-9 MR signature: resolution of trihedrals with different dimensions 57
- 4-10 MR signature: resolution of dihedrals with different angles of orientation 57

5-1	Optimal processor as a whiten-correlator system	61
5-2	Optimal processor as a filter-sample system	62
5-3	Receiver Operating Characteristic: Marcum's Q -function	63
5-4	Detection probability versus effective signal-to-noise ratio	64
5-5	Comparison of specular mirror and uniform clutter return in the frequency domain	65
5-6	Normalized d_{opt} as a function of tilt $ \phi_x $	67
5-7	Normalized d_{opt} as a function of target azimuth dimension ρ_x	69
5-8	Conventional imager-receiver	70
5-9	Effective signal-to-noise ratio comparison (against target size ρ_x) of optimal processor vs. conventional processor	72
5-10	Effective signal-to-noise ratio comparison (against target tilt $ \phi_x $) of optimal processor vs. conventional processor	73
5-11	Effective signal-to-noise ratio comparison (against target curvature $\frac{k\rho_x^2}{ R_x }$) of optimal processor vs. conventional processor	74
5-12	Adaptive multi-resolution receiver structure	75
5-13	Effective signal-to-noise ratio comparison (against effective target size $\tilde{\rho}_x$) of optimal processor vs. adaptive MR processor	77
5-14	Effective signal-to-noise ratio comparison (against target tilt $ \phi_x $) of optimal processor vs. adaptive MR processor	78
5-15	Estimator-correlator realization for optimal detection of diffuse target in white receiver noise	82
5-16	Filter-squarer-integrator realization for optimal detection of diffuse target in white receiver noise	83
5-17	Receiver Operating Characteristic for detection of diffuse target return from white receiver noise.	85
5-18	Optimal detection probability versus size of diffuse target ρ_x	87
5-19	Optimal detection probability versus SNR of diffuse target	88
5-20	Multi-resolution imager with integration period κT_{dw}	89
5-21	Comparison of optimal and MR detection probabilities of a diffuse target (as a function of ρ_x)	91
5-22	Comparison of optimal and MR detection probabilities of a diffuse target (as a function of SNR)	92
5-23	Conventional imager with full dwell time integration period T_{dw}	93
5-24	Comparison of optimal and conventional detection probabilities of a diffuse target (as a function of ρ_x)	94

5-25 Comparison of optimal and conventional detection probabilities of a diffuse target (as a function of SNR) 95

List of Tables

3.1	Summary of target returns	41
4.1	Target MR signature: resolution for $\kappa = 1$ (full dwell time), compared with original target return duration	50
4.2	Specular mirror MR signature: offset for $\kappa = 1$ (full dwell time), compared with original target return offset	54
5.1	Conditions for optimality of the adaptive MR processors	97

Chapter 1

Introduction

Radars have long been used, for both military and non-military purposes, in a wide variety of applications such as imaging, guidance, remote sensing, and global positioning [3, 26]. The basic principle of radar is to transmit an electromagnetic waveform which, after propagation through a medium (e.g., the atmosphere), scatters, or reflects off an object and then propagates back to the radar's receiver. Partial information about the object's location, velocity, geometry, and material composition may then be inferred from the received signal. For the case of locating a target in azimuth and elevation, the resolution of a real-aperture radar is limited by its transmitter's diffraction width, because, from the received waveform, it is generally not possible to distinguish two targets that are both located within this "footprint". For an antenna of aperture a operating at wavelength λ and range L , the footprint is approximately $\lambda L/a$ in width. Laser radars, or ladars [16], are used to seek improved resolution by operating at the infrared (IR) frequency band which has a smaller wavelength than that of conventional, microwave radars.

Another way of achieving better resolution from radars is signal processing. A synthetic aperture radar (SAR) [8, 5] takes advantage of a known relative motion between the radar and the target to coherently integrate a returned signal, such that the processed signal approximates one received through an aperture whose size equals the distance covered by the motion of the radar over the same time period. This reduces the size of the effective footprint at range L , which in turn improves the resolution. Indeed, the resolution achieved by SAR can be made independent of the radar-to-target range L , a property which is desirable in many cases.

1.1 Motivation

A major use of SAR's high resolution capability is to image terrain as the sensor front-end for an automatic target detection and recognition (ATD/R) system [20]. ATD/R systems typically employ a multi-stage architecture comprising imaging, detection, classification, and recognition sub-

systems [30]. However, achieving the best overall performance requires that each stage fully exploits the capabilities of its predecessors.

In particular, because classification and recognition algorithms tend to be computationally intensive, it is crucial that the detection stage provides an efficient means for screening out vast amounts of natural background, such as grass and bushes, in which the far more limited number of man-made objects, such as tanks and planes, are embedded. One fundamental difference between the natural and man-made objects is their surface roughness relative to the wavelength of a microwave or millimeter wave radar. Man-made objects, due to the metallic material used, usually have smooth surfaces whose fluctuations in height are on a microscopic scale compared to the wavelength. This kind of targets are termed “specular” and the spatial coherence of the impinging radar beam is preserved in the reflected beam. Natural objects have rough surfaces whose fluctuations in height may greatly exceed a wavelength. These are termed “diffuse” and they turn a spatially coherent impinging radar beam into a spatially incoherent reflected radar beam.

Motivated by the same goal of separating man-made targets from natural clutter, Chaney et al. [4] introduced an adaptive signal processing algorithm to exploit the aspect-dependence of man-made targets, those that exhibit a “broad-side flash.”¹ Improved resolution and dynamic range in the resulting SAR images were claimed. Irving et al. [15] employed a multi-resolution (MR), recursive imaging algorithm and devised a discriminator for distinguishing man-made targets from natural clutter based on the MR image models of these two types of targets. This discriminator out-performed the conventional one used in the Lincoln Laboratory ATR system. However, neither these studies, nor other related works, have taken a principled approach – one based on the physical characteristics of the reflecting surfaces and their interaction with SAR operation – to MR-SAR image formation and optimal target detection. The present thesis is a first step toward such a fundamental assessment.

Using the physical optics formalism established in [21], this thesis investigates in depth a small repertoire of geometrically simple specular and diffuse targets that are motionless on the target terrain, and explores some of their differences by analyzing their target models, their contributions to the radar return, and their MR 1-D continuous-wave SAR images. The aspect-dependence of man-made targets shown in [4] is clearly present in the analysis for our specular mirror. Due to the differences in the targets’ MR signatures, this class of multi-resolution processor may serve as a discriminator for different target returns.

In addition to deriving MR SAR-image statistics for specular and diffuse objects, we also pose and solve several simple but relevant Neyman-Pearson detection problems involving this collection of targets. The receiver operating characteristics (detection versus false-alarm probability) of these

¹The radar receives maximum return when it is at a location, along its flight of path, closest to the scattering main lobe of the target. For a plane mirror, that would be along its principle axis, or the surface normal at the center of the mirror.

processors are evaluated. They serve as the ultimate performance limits for more realistic detection problems in which the exact target categories and geometries are unknown.

We shall now demonstrate the basic principles of a continuous wave (CW) 1-D SAR on which this thesis is built. Then, we will close this chapter with an outline of the thesis.

1.2 Basic 1-D SAR Principles

As shown in Figure 1-1, we are interested in a down-looking radar (the radar's line-of-sight is perpendicular to the target reference plane, $z = 0$) flying at a constant transverse velocity over the target terrain. The transmitted field is a transverse-polarized wave that propagates in the direction of the line-of-sight, $-\hat{z}$.

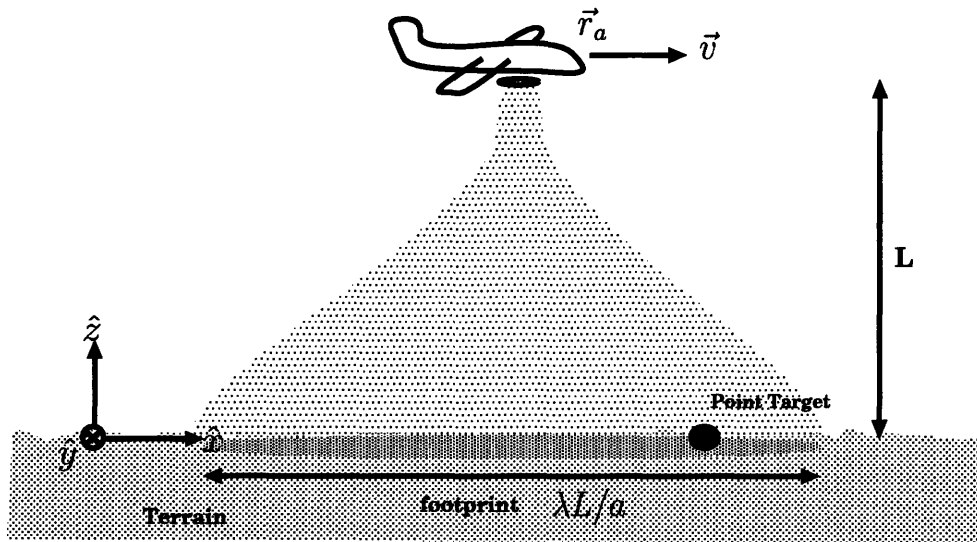


Figure 1-1: Geometry of radar operation

We first examine the position-dependent Doppler frequency chirp imparted to the radar return by the known relative motion between the radar and a point target. This same frequency chirp is present on the radar returns for all stationary targets, such as the ones presented in Chapter 3, and is exploited by SAR post-reception processing for high-resolution image formation or target detection (Chapter 4 and 5.)

Without loss of generality, we pick our coordinate system such that our point target is situated at $(0, y)$ on the target terrain ($z = 0$ plane.) The radar is moving at a constant transverse velocity along the trajectory,

$$\vec{r}_a(t) = \vec{v}t + L\hat{z} = vt\hat{x} + 0\hat{y} + L\hat{z}. \quad (1.1)$$

We can then write the range equation to describe the time-dependent distance between the radar

and the point target.

$$\vec{r}_i(t) = (vt)\hat{x} + y\hat{y} + L\hat{z} \quad (1.2)$$

$$|\vec{r}_i(t)| = \sqrt{(vt)^2 + y^2 + L^2} \quad (1.3)$$

$$\approx L + \frac{(vt)^2 + y^2}{2L} \quad (1.4)$$

where the paraxial approximation $(vt)^2 + y^2 \ll L^2$ has been used.

For now, we neglect the details of the radar system such as the antenna beam patterns, etc. We can directly argue for there being a chirp on the return from this point target in the following physical way. We are using a CW transmitter whose output is a sinusoid $\cos(2\pi\nu t - \psi)$ for some appropriate phase shift ψ . The return from the point target will be another sinusoid delayed by $\frac{2|\vec{r}_i(t)|}{c}$, where c is the speed of light, and hence proportional to $\cos\left(2\pi\nu\left(t - \frac{2|\vec{r}_i(t)|}{c}\right) - \psi'\right)$, where ψ' is another phase shift. The instantaneous Doppler frequency shift of this signal is thus,

$$\nu_D(t) \equiv -\frac{1}{2\pi} \frac{\partial}{\partial t} \frac{\nu 2|\vec{r}_i(t)|}{c} \quad (1.5)$$

$$\approx -\frac{\partial}{\partial t} \frac{2}{\lambda} \left(L + \frac{(vt)^2 + y^2}{2L} \right) \quad (1.6)$$

$$= -\frac{2v^2}{\lambda L} t \quad (1.7)$$

which is a linear chirp centered at the time when the plane flies right above the target. In complex envelope form, this chirp corresponds to a quadratic-in-time phase shift, $\exp\left[j\frac{kv^2}{L}t^2\right]$ (where $k = \frac{2\pi\nu}{c}$ is the wave number), a term which will be seen often in all the radar returns analyzed in Chapter 3. Due to the range equation used (1.4), this linear chirp is only an approximation of the actual Doppler chirp, as seen in Figure 1-2. The approximation is reasonably good for $|t| < \frac{L}{2v}$. Since we only care about a target's presence when it is within the illumination of the radar's footprint, i.e., within the dwell period of $\frac{\lambda L}{av}$ corresponding to the time the plane takes to fly a distance the size of the footprint, we see that this linear chirp approximation is good for $a \gg 4\lambda$, an assumption easily satisfied by a microwave radar.

The resulting dwell-limited bandwidth of the return will then have a chirp bandwidth of

$$\text{BW} \equiv \left| \nu_D\left(t + \frac{\lambda L}{2av}\right) - \nu_D\left(t - \frac{\lambda L}{2av}\right) \right| \quad (1.8)$$

$$\approx \left| \frac{\partial}{\partial t} \nu_D(t) \right| \frac{\lambda L}{av} \quad (1.9)$$

$$= \frac{2v}{a} \quad (1.10)$$

How well we can resolve the signal in time (or how well we can resolve the target in space) is

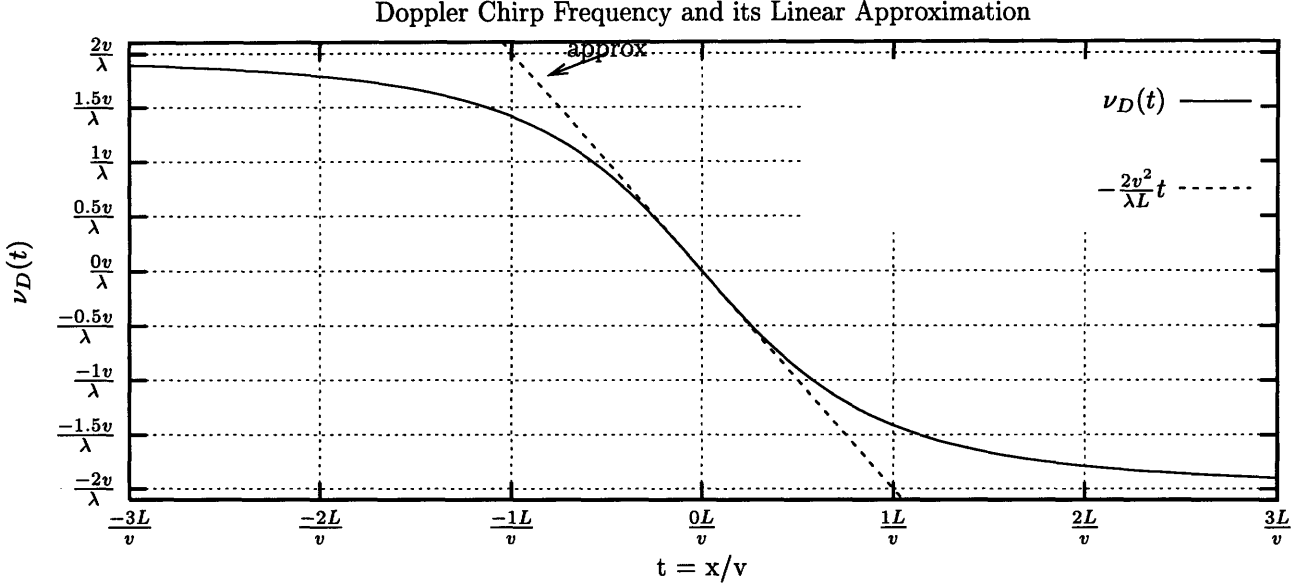


Figure 1-2: Linear approximation to motion-induced Doppler frequency chirp

approximately inversely proportional to the bandwidth of the output signal,

$$t_{res} \approx \frac{1}{BW} = \frac{a}{2v} \ll \frac{\lambda L}{av} \quad (1.11)$$

The last inequality is true because of the Fraunhofer far field assumption of the radar. This is the SAR processing that we have used to improve the along-track resolution of our target:

$$x_{res} \equiv vt_{res} = \frac{a}{2} \ll \frac{\lambda L}{a} \quad (1.12)$$

This has an interpretation of that we have synthesized an aperture the size of the footprint, which is much larger than the physical aperture itself. The synthesized aperture helps focus the antenna to give a high resolution.

So far our presentation of the 1-D SAR principles is heavily based on the assumption of a target of negligible size, hence point target. The other target models explored in this thesis will more realistically be finite-size. We shall come to an understanding of how the size, together with possibly other target geometric parameters, will affect the effectiveness of SAR processing.

1.3 Thesis Outline

In Chapter 2, the geometry of the radar operation and the structure of our radar system model will be stated. Our notation for its system parameters will be laid out. The general diffuse and specular target models will be proposed, and their underlying physical interpretations will be explained and

compared.

In Chapter 3, we will present a collection of diffuse and specular targets, in a handbook-like manner, by specializing the general models introduced in Chapter 2. Their individual radar-return signals will be used to develop an understanding of the influence of target geometry and surface characteristics on the signals.

Chapter 4 presents a derivation of the conventional SAR image formation filter. This derivation is generalized to a coherent post-reception integration to obtain an integration-time-dependent Carrier-to-Noise Ratio (CNR). This is what we call the MR signature for a target. The fact that different targets show different signatures tells us that the target returns can be discriminated by their MR behaviors. This serves as the motivation for our detection problems in the following chapter.

Chapter 5 poses two target-discrimination problems involving a subset of the targets presented in Chapter 3. The first one involves the absence or presence of a specular mirror in extended diffuse clutter. The second one involves the absence or presence of a diffuse target. In both detection problems, the radar return is corrupted by receiver noise. The Neyman-Pearson optimal processors (maximum detection probability subject to chosen false alarm probability) required are found and their receiver operating characteristics are evaluated. The problems are simplistic because we assume prior knowledge of the target's location, the type of target, and the target's geometry. Nevertheless, by comparing the performances of the optimal receivers and that of the conventional receivers in various situations, we can learn when and why the conventional receivers yield sub-optimal performance so as to give directions for improvements in future SAR system design.

In Chapter 6, we will summarize the thesis and conclude with several comments about multi-resolution SAR image formation and target discrimination. Several possible extensions to this work will be discussed.

Chapter 2

Radar System Model

In this chapter, we will first go through a detailed description of the radar system – from the transmitted field through propagation to the target region, target interaction, propagation back to the radar, return reception, and post-reception processing. A detailed explanation and discussion of the general diffuse and specular target models will follow.

2.1 Radar Model

Our radar will be assumed to be monostatic—the transmitter and receiver share the same antenna. Although the transmitter, the atmospheric effects, the target, and the receiver front end might all be sensitive to the vector/polarization characteristics of the radar’s radiation, we will choose scalar wave modeling for its mathematical tractability in this first analysis of specular and diffuse targets.

For portability in an airborne setting, the radar’s dimensions are usually small such that the target terrain is in the Fraunhofer far field of the radar antenna, and, except for applications such as the foliage-penetrating SAR, the radar is usually in the Fraunhofer far field of the target’s reflective surface. Therefore, only the far field in the vicinity of the radar’s principle axis is of interest. This paraxial limit assumption is necessary for the validity of scalar wave modeling (especially scalar wave diffraction [18].)

2.1.1 Radar Motion

Our airborne radar will be mounted on a plane flying at a constant transverse velocity $\vec{v} = v\hat{x} + 0\hat{y}$ at some fixed height (Figure 1-1), such that our radar motion can be described by

$$\vec{r}_a(t) = \vec{v}t + L\hat{z} = vt\hat{x} + 0\hat{y} + L\hat{z}. \quad (2.1)$$

We call \hat{x} the azimuth or along-track direction, \hat{y} the across-track direction, and $\pm\hat{z}$ the radar's line-of-sight.

2.1.2 Radar Transmitter

The transmitter model is characterized by the real-valued field at the exit pupil ($z = L$ plane), $E_{tr}(\bar{\rho}, t)$, in $\sqrt{\text{Watts/m}^2}$, as a function of the transverse coordinates $\bar{\rho}' = [x' \ y']^T$ and time t ,

$$E_{tr}(\bar{\rho}', t) = \Re \{ \mathbf{E}_{tr}(\bar{\rho}', t) \exp[-j2\pi\nu t] \} \quad (2.2)$$

$$\mathbf{E}_{tr}(\bar{\rho}', t) = \sqrt{P_{tr}} \mathbf{U}_{ant}(\bar{\rho}', t) \quad (2.3)$$

where

P_{tr} = transmitted power

$\mathbf{U}_{ant}(\bar{\rho}', t)$ = normalized (square-integral unity)

transmitted spatial antenna beam pattern

The time dependence of $\mathbf{U}_{ant}(\bar{\rho}', t)$ is merely due to the motion of the radar transmitter traveling at a velocity \bar{v} :

$$\mathbf{U}_{ant}(\bar{\rho}', t) = \mathbf{U}_{ant}^o(\bar{\rho}' - \bar{v}t) \quad (2.4)$$

where $\mathbf{U}_{ant}^o(\bar{\rho}')$ is the fixed spatial antenna beam pattern in the radar's rest-frame. We use a normalized, continuous wave (CW) collimated elliptical-Gaussian beam to model the finite aperture dimensions a_x and a_y of the transmitter antenna.

$$\mathbf{U}_{ant}^o(\bar{\rho}') = \sqrt{\frac{2}{\pi a_x a_y}} \exp \left[- \left(\frac{x'}{a_x} \right)^2 - \left(\frac{y'}{a_y} \right)^2 \right] \quad (2.5)$$

We will assume that the actual antenna aperture, A , does not appreciably truncate the Gaussian beam pattern, i.e.,

$$\int_A |\mathbf{U}_{ant}^o(\bar{\rho}')|^2 d\bar{\rho}' \approx \int_{-\infty}^{+\infty} |\mathbf{U}_{ant}^o(\bar{\rho}')|^2 d\bar{\rho}' = 1 \quad (2.6)$$

In the subsequent development, the limits in the integration over the radar antenna as above will be dropped and the approximation sign will be taken as an equal sign for notational convenience.

This confirms that our CW transmitter has a constant power of

$$\int_A |\mathbf{E}_{tr}(\bar{\rho}', t)|^2 d\bar{\rho}' = \int_{z=L} |\sqrt{P_{tr}} \mathbf{U}_{ant}^o(\bar{\rho}')|^2 d\bar{\rho}' = P_{tr}. \quad (2.7)$$

We have used an elliptical beam because we would like to examine the separate effects of the along-track and across-track dimensions of the antenna's beam pattern, which are usually different in SAR practice because, for the same desired resolution, a 1-D SAR has different antenna width requirements in the azimuth and across-track directions. [21]

2.1.3 Propagation to Target Region

During the propagation of the transmitted waveform from the radar to the target terrain, the coherent beam will generally suffer from the effects of atmospheric extinction and turbulence [21]. Since atmospheric effects are not the emphasis of this thesis, we will use a free-space propagation model [18], which is sufficient for operation in good weather, to describe the illuminating field at the target plane $z = 0$,

$$\mathbf{E}_{il}(\bar{\rho}, t) = \int_{z=L} \mathbf{E}_{tr}(\bar{\rho}', t - \frac{L}{c}) \mathbf{h}_L(\bar{\rho}' - \bar{\rho}) d\bar{\rho}' \quad (2.8)$$

$$\mathbf{h}_L(\bar{\rho}') \equiv \frac{1}{j\lambda L} \exp\left(jkL + j\frac{k|\bar{\rho}'|^2}{2L}\right) \quad (2.9)$$

where c is the speed of light, λ is the transmitted beam's wavelength, $k = 2\pi/\lambda = 2\pi\nu/c$ is the wave number, and $\mathbf{h}_L(\bar{\rho}')$ is the space-invariant impulse response (or Green's function) for propagating the transmitted waveform through a distance L of free-space in the paraxial limit.¹ We have used $\bar{\rho} = [x \ y]^T$ for the transverse coordinates at the $z = 0$ plane to distinguish them from $\bar{\rho}' = [x' \ y']^T$ at the $z = L$ plane.

With the far field approximation

$$\frac{ka_x^2}{2L} \ll 1, \quad \frac{ka_y^2}{2L} \ll 1 \quad (2.10)$$

we get

$$\mathbf{E}_{il}(\bar{\rho}, t) \approx \mathbf{h}_L(\bar{\rho}) \tilde{\mathbf{E}}_{tr}\left(\frac{\bar{\rho}}{\lambda L}, t - \frac{L}{c}\right) \quad (2.11)$$

$$\approx \mathbf{h}_L(\bar{\rho}) \tilde{\mathbf{E}}_{tr}\left(\frac{\bar{\rho}}{\lambda L}, t\right) \quad (2.12)$$

where $\tilde{\mathbf{E}}_{tr}\left(\frac{\bar{\rho}}{\lambda L}, t\right)$ is the transverse (2-D) spatial Fourier transform of $\mathbf{E}_{tr}(\bar{\rho}', t)$ evaluated at $\frac{\bar{\rho}}{\lambda L}$, and

¹The paraxial approximation is $|\bar{\rho}' - \bar{\rho}| \ll L$, and therefore, $\sqrt{|\bar{\rho}' - \bar{\rho}|^2 + L^2} \approx L + \frac{|\bar{\rho}' - \bar{\rho}|^2}{2L}$. We are only interested in the field within the radar footprint on the target plane where it is sufficiently illuminated by the radar. So there is little loss of generality imposed by assuming paraxial propagation from the radar to the ground.

we have neglected the radar lag time (the $\frac{L}{c}$ time delay, during which the radar moves a distance $\frac{vL}{c}$, because it is generally too small to affect the transmitter beam pattern.) The spatial-invariance of our system in conjunction with the radar's motion (2.4) now allows us to write

$$\mathbf{E}_{il}(\bar{\rho}, t) = \mathbf{E}_{il}(\bar{\rho} - \bar{v}t, t = 0) \quad (2.13)$$

$$= \mathbf{h}_L(\bar{\rho} - \bar{v}t) \bar{\mathbf{E}}_{tr}\left(\frac{\bar{\rho} - \bar{v}t}{\lambda L}, t = 0\right) \quad (2.14)$$

Finally, because of the reciprocity of free-space, the same model can be used to calculate the received field at the radar, $\mathbf{E}_{rec}(\bar{\rho}', t)$, from the reflected field at the target plane, $\mathbf{E}_{rfl}(\bar{\rho}, t)$, once the latter has been found:

$$\mathbf{E}_{rec}(\bar{\rho}', t) = \int_{z=0} \mathbf{E}_{rfl}(\bar{\rho}, t - \frac{L}{c}) \mathbf{h}_L(\bar{\rho}' - \bar{\rho}) d\bar{\rho} \quad (2.15)$$

2.1.4 Target Model

Unless the field strength is extremely high, which is not true in general radar practice, the reflected field will be a linear functional of the illuminating field (or incident field)

$$\mathbf{E}_{rfl}(\bar{\rho}, t) = \int_{z=0} \mathbf{T}(\bar{\rho}, \bar{\rho}_1) \mathbf{E}_{il}(\bar{\rho}_1, t) d\bar{\rho}_1 \quad (2.16)$$

where $\mathbf{T}(\bar{\rho}, \bar{\rho}_1)$ is the (possibly space-varying) complex reflection impulse response of the target, relating the contribution of the incident field at $\bar{\rho}_1$ to the reflected field at $\bar{\rho}$ in a linear fashion. We have assumed that the target is independent of time and the radar's carrier frequency.

This $\mathbf{T}(\bar{\rho}, \bar{\rho}_1)$ can be random, deterministic, or a combination of both. It is a special case of the $\bar{\mathbf{R}}$ matrix presented in [24] for general linear target interactions. One common specialization of this complex reflection impulse response is to assume that the reflected field at $\bar{\rho}$ depends only on the illuminating field at $\bar{\rho}$, i.e. the spatial counterpart of a "memoryless" time-domain system:

$$\mathbf{T}(\bar{\rho}, \bar{\rho}_1) = \mathbf{T}(\bar{\rho}) \delta(\bar{\rho} - \bar{\rho}_1) \quad (2.17)$$

$$\mathbf{E}_{rfl}(\bar{\rho}, t) = \mathbf{T}(\bar{\rho}) \mathbf{E}_{il}(\bar{\rho}, t) \quad (2.18)$$

This is also known as the multiplicative model.² We will discuss the target model in greater depth in the next section.

²Note that $\mathbf{T}(\bar{\rho})$ is dimensionless, but $\mathbf{T}(\bar{\rho}, \bar{\rho}_1)$ has the unit $1/m^2$

2.1.5 Receiver Model

The receiver antenna converts the received field to an electrical signal:

$$\mathbf{y}'(t) = \int_{z=L} d\bar{\rho}' \mathbf{E}_{rec}(\bar{\rho}', t) \mathbf{U}_{ant}(\bar{\rho}', t). \quad (2.19)$$

Notice that the same antenna pattern is used in the receiver as that of the transmitter because our

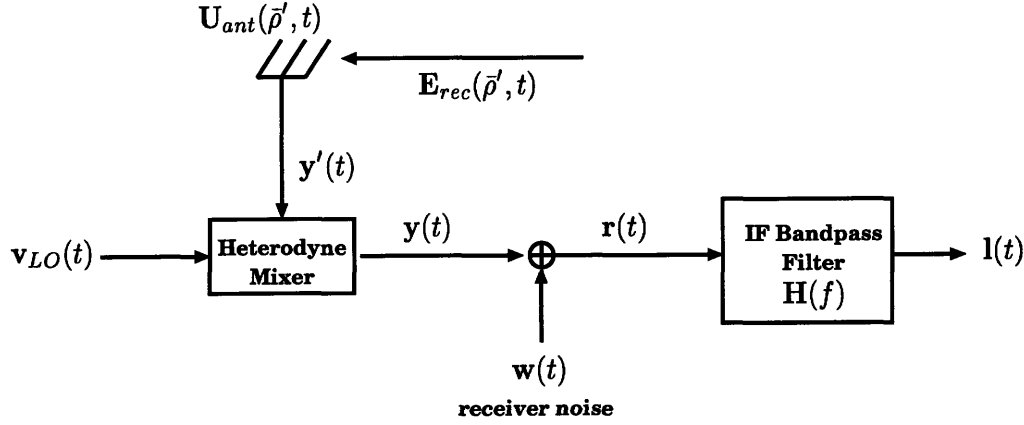


Figure 2-1: IF Signal model

radar is monostatic. This return signal is then beat in a heterodyne mixer with a local oscillator (LO) waveform, $v_{LO}(t)$, of frequency $\nu_{LO} = \nu - \nu_{IF}$. $v_{LO}(t)$ has the complex envelope

$$v_{LO}(t) = V_{LO} \exp[j2\pi\nu_{IF}t] \quad (2.20)$$

corresponding to the real valued waveform

$$v_{LO}(t) = \Re\{V_{LO} \exp[-j2\pi(\nu - \nu_{IF})t]\} \quad (2.21)$$

That leads us to the IF beat signal

$$y(t) = \Re\{\mathbf{y}(t) \exp[-j2\pi\nu_{IF}t]\} \quad (2.22)$$

The heterodyne mixer shifts the signal from the transmission (or radio) frequency (RF), ν , to the processing frequency (or intermediate) frequency (IF), ν_{IF} . For analytical convenience, we have normalized out the heterodyne mixing gain, such that $\mathbf{y}(t)$ does not depend on the LO voltage. This output signal $\mathbf{y}(t)$ is then passed through a bandpass filter $\mathbf{H}(f)$ whose main function is to select out the signal component of the electrical signal at the beat (IF) frequency. We have used f to represent the processing frequency in Hz centered at the IF frequency ν_{IF} such that $f = \nu - \nu_{IF}$.

The functional form of $\mathbf{H}(f)$ dictates what application-dependent post-reception processing is done with the target return signal. This $\mathbf{H}(f)$ will be specified for different situations in the later chapters.

The following model for the normalized radar return and receiver noise is used in all that follows [25],

$$r(t) = \Re\{\mathbf{r}(t) \exp[-j2\pi\nu_{IF}t]\} \quad (2.23)$$

where

$$\mathbf{r}(t) = \mathbf{y}(t) + \mathbf{w}(t) \quad (2.24)$$

$$\mathbf{y}(t) = \int_{z=L} d\bar{\rho}' \mathbf{E}_{rec}(\bar{\rho}', t) \mathbf{U}_{ant}(\bar{\rho}', t) \quad (2.25)$$

$$\mathbf{l}_y(t) \equiv \mathbf{y}(t) * \mathbf{h}(t) \quad (2.26)$$

$$\mathbf{l}_w(t) \equiv \mathbf{w}(t) * \mathbf{h}(t) \quad (2.27)$$

$$\mathbf{l}(t) = \mathbf{r}(t) * \mathbf{h}(t) = \mathbf{l}_y(t) + \mathbf{l}_w(t). \quad (2.28)$$

Here, $\mathbf{r}(t)$ is the normalized complex envelope of the IF target return plus receiver noise; and $\mathbf{w}(t)$ is the receiver noise, which is usually dominated by thermal noise, and is modeled by a zero-mean, circulo-complex white Gaussian noise with spectral density N_o [27].

After substituting (2.3, 2.15, 2.16, 2.12) into (2.25), we find that the radar return is given by

$$\mathbf{y}(t) = \int_{z=0} d\bar{\rho}_1 \int_{z=0} d\bar{\rho} \mathbf{T}(\bar{\rho}, \bar{\rho}_1) \sqrt{P_{tr}} \mathbf{h}_L(\bar{\rho}_1) \tilde{\mathbf{U}}_{ant} \left(\frac{\bar{\rho}_1}{\lambda L}, t - \frac{2L}{c} \right) \mathbf{h}_L(\bar{\rho}) \tilde{\mathbf{U}}_{ant} \left(\frac{\bar{\rho}}{\lambda L}, t \right) \quad (2.29)$$

where $\tilde{\mathbf{U}}_{ant}(\cdot, t)$ is the 2-D spatial Fourier transform of the normalized antenna spatial beam pattern at time t . Further, neglecting the lag time $\frac{2L}{c}$, and using the space-invariance of our system (2.4, 2.14),

$$\mathbf{h}_L(\bar{\rho}) \tilde{\mathbf{U}}_{ant} \left(\frac{\bar{\rho}}{\lambda L}, t \right) = \mathbf{h}_L(\bar{\rho} - \bar{v}t) \tilde{\mathbf{U}}_{ant}^o \left(\frac{\bar{\rho} - \bar{v}t}{\lambda L} \right). \quad (2.30)$$

we arrive at

$$\mathbf{y}(t) \approx \sqrt{P_{tr}} \int_{z=0} d\bar{\rho}_1 \int_{z=0} d\bar{\rho} \mathbf{T}(\bar{\rho}, \bar{\rho}_1) \mathbf{h}_L(\bar{\rho}_1 - \bar{v}t) \tilde{\mathbf{U}}_{ant}^o \left(\frac{\bar{\rho}_1 - \bar{v}t}{\lambda L} \right) \mathbf{h}_L(\bar{\rho} - \bar{v}t) \tilde{\mathbf{U}}_{ant}^o \left(\frac{\bar{\rho} - \bar{v}t}{\lambda L} \right) \quad (2.31)$$

or, for the multiplicative target model (2.18),

$$\mathbf{y}(t) = \sqrt{P_{tr}} \int_{z=0} d\bar{\rho} \mathbf{T}(\bar{\rho}) \mathbf{h}_L^2(\bar{\rho} - \bar{v}t) \tilde{\mathbf{U}}_{ant}^o{}^2 \left(\frac{\bar{\rho} - \bar{v}t}{\lambda L} \right). \quad (2.32)$$

The radar model established in this section is summarized by the system block diagram shown in Figure 2-2.

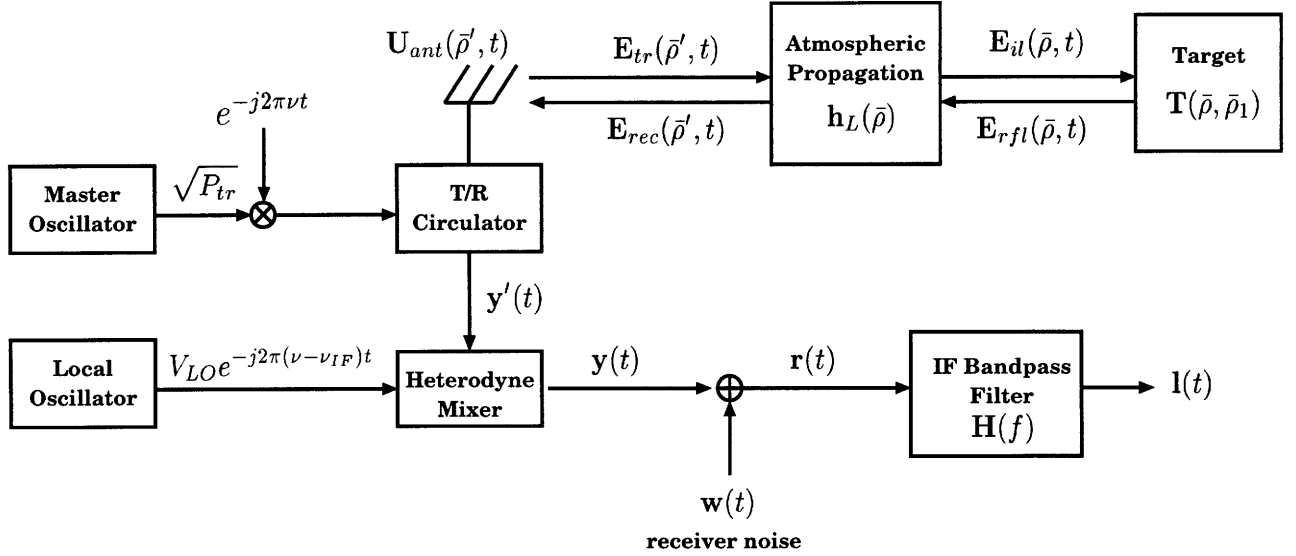


Figure 2-2: Radar system block diagram

2.2 Target Model

The most general linear target interaction model was given by (2.16), but in practice, the multiplicative model (2.18) is often sufficient and used. We will first discuss the multiplicative model because its physics can be more easily interpreted. The general linear model will be needed because the multiplicative model cannot explain the reflection behavior of multiple-bounce specular reflectors, introduced in the next chapter.

2.2.1 Multiplicative Model

The multiplicative target model $\mathbf{T}(\bar{\rho})$ is a complex-valued, spatially-varying reflection coefficient that, via

$$\mathbf{E}_{rfl}(\bar{\rho}, t) = \mathbf{T}(\bar{\rho})\mathbf{E}_{il}(\bar{\rho}, t), \quad (2.33)$$

relates the $+\hat{z}$ -going reflected field, \mathbf{E}_{rfl} , at the ground reference plane ($z = 0$) to the $-\hat{z}$ -going illumination field, \mathbf{E}_{il} , at the same plane. The multiplicative model assumes that the reflected field, $\mathbf{E}_{rfl}(\bar{\rho}, t)$ depends only on the incident field, $\mathbf{E}_{il}(\bar{\rho}, t)$ at the same transverse coordinate $\bar{\rho}$ (spatially memoryless.) Although simplistic, the model agrees with Snell's law of reflection and can be adapted to represent specular, diffuse, or a combination of both reflections.

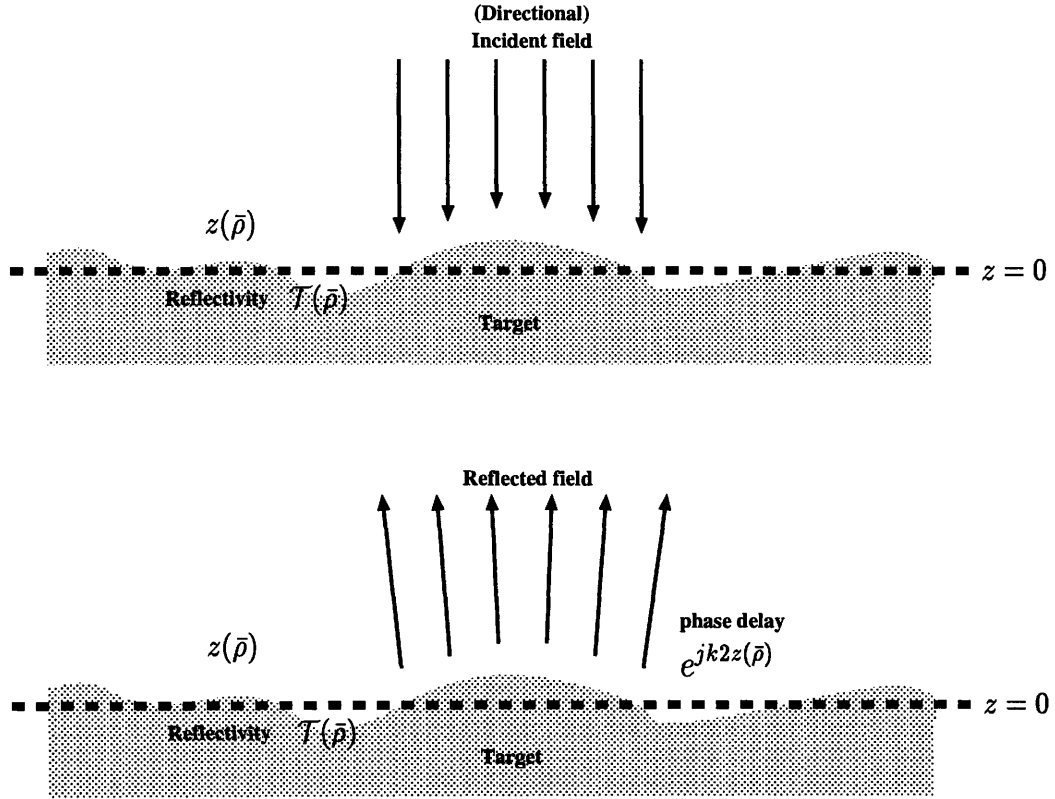


Figure 2-3: Input-output relation for a multiplicative target model

There is a simple physical interpretation to this multiplicative model: the relative height of the target surface (relative to the target plane $z = 0$), $z(\bar{\rho})$, produces a phase delay due to the wave traveling from the nominal range $z = 0$ to the surface and back, i.e., $\exp[j2kz(\bar{\rho})]$. This phase term modulates the square root of a non-negative, nominal reflective intensity $\mathcal{T}(\bar{\rho})$ to give

$$\mathbf{T}(\bar{\rho}) = \sqrt{\mathcal{T}(\bar{\rho})} \exp[j2kz(\bar{\rho})]. \quad (2.34)$$

This interpretation is valid for targets that are in the paraxial limit and do not have steep edges with respect to the target reference plane.

The specularity or diffuseness of a target depends on the surface smoothness of the target in comparison to the radar wavelength. What would be diffuse for a laser radar with a wavelength of one to ten microns might closely resemble a purely specular target for a millimeter wave radar.

Diffuse Model

A diffuse, or speckle, target will have large surface height fluctuations (or roughness) which contributes to the stochastic nature of the reflection coefficient $\mathbf{T}(\bar{\rho})$. We shall model such a surface

using the moments [24, 25, 6]

$$\langle \mathbf{T}(\bar{\rho}) \rangle = 0 \quad (2.35)$$

$$\langle \mathbf{T}(\bar{\rho})\mathbf{T}(\bar{\rho}_1) \rangle = 0 \quad (2.36)$$

$$\langle \mathbf{T}(\bar{\rho})\mathbf{T}^*(\bar{\rho}_1) \rangle = \lambda^2 \mathcal{T}_d(\bar{\rho})\delta(\bar{\rho} - \bar{\rho}_1) \quad (2.37)$$

where $\langle \cdot \rangle$ represents ensemble average, and $\mathcal{T}_d(\bar{\rho})$ is the mean diffuse reflectivity (intensity of reflection) at transverse position $\bar{\rho}$. With the target height interpretation (2.34), both $\sqrt{\mathcal{T}(\bar{\rho})}$ and $z(\bar{\rho})$ are now random quantities – in such a way that the averages in (2.35) and (2.36) vanish. Equation (2.37) says that the random reflectivity is uncorrelated in space and has no directional information in it (the δ function gives uniform response to all spatial frequencies, i.e. it is isotropic.) Together, this set of equations state that a diffuse target turns a spatially coherent illuminating beam into a spatially incoherent reflected beam.³

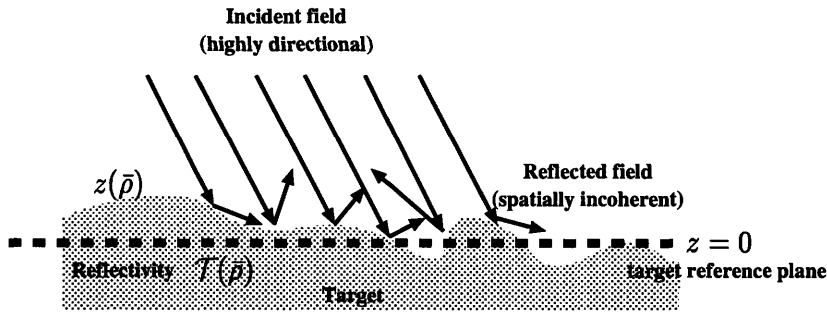


Figure 2-4: Rough surface gives diffuse reflections

From the radar's perspective, the received field will be a summation of scattered field contributions from a large number of small facets on the rough surface. Thus, via the central-limit theorem, we can assume that $\mathbf{T}(\bar{\rho})$ is a circulo-complex Gaussian process [27] insofar as the received field is concerned. The phase of the reflectivity $\angle \mathcal{T}(\bar{\rho}) = \exp[j2kz(\bar{\rho})]$ is uniformly distributed between

³This statement can be more rigorously shown by taking the spatial Fourier transforms of (2.37).

$$\int d\bar{\rho} \int d\bar{\rho}_1 \langle \mathbf{T}(\bar{\rho})\mathbf{T}^*(\bar{\rho}_1) \rangle e^{-j2\pi\bar{s}\cdot\bar{\rho}} e^{+j2\pi\bar{s}_1\cdot\bar{\rho}_1} = \int \lambda^2 \mathcal{T}_d(\bar{\rho}) e^{-j2\pi(\bar{s}-\bar{s}_1)\cdot\bar{\rho}} d\bar{\rho} \quad (2.38)$$

where $\bar{s}_1, \bar{s} = [s_{x1} \ s_{y1}]^T, [s_x \ s_y]^T$ are transverse spatial frequency vectors, and therefore

$$\langle \tilde{\mathbf{T}}(\bar{s})\tilde{\mathbf{T}}^*(\bar{s}_1) \rangle = \lambda^2 \tilde{\mathcal{T}}_d(\bar{s} - \bar{s}_1) \quad (2.39)$$

where $\tilde{\mathbf{T}}(\cdot)$ and $\tilde{\mathcal{T}}_d(\cdot)$ are the spatial Fourier transform of $\mathbf{T}(\cdot)$ and $\mathcal{T}_d(\bar{\rho})$ respectively. This implies $\tilde{\mathbf{T}}(\bar{s})$ is a wide-sense stationary (WSS) stochastic process with spectrum of $\mathcal{T}_d(\bar{\rho})$. Therefore, the Fourier transform of (2.33)

$$\tilde{\mathbf{E}}_{rfi}(\bar{s}, t) = \int \tilde{\mathbf{T}}(\bar{s} - \bar{s}_1) \tilde{\mathbf{E}}_{il}(\bar{s}_1, t) d\bar{s}_1 \quad (2.40)$$

implies passing the input field $\tilde{\mathbf{E}}_{il}(\bar{s}_1, t)$ through a WSS random linear spatial-frequency-invariant system $\tilde{\mathbf{T}}(\bar{s})$ such that the output $\tilde{\mathbf{E}}_{rfi}(\bar{s}, t)$ is also a WSS random process in the spatial frequency \bar{s} .

0 and 2π and is uncorrelated with the magnitude $|\mathbf{T}(\bar{\rho})| = \sqrt{\mathcal{T}(\bar{\rho})}$, which is Rayleigh distributed. This process is white but *not* homogeneous (2.37) unless $\mathcal{T}_a(\bar{\rho})$ is a constant.

In addition, the diffuse model can be interpreted as one limit of the Gaussian-Schell model to be discussed in Appendix A, in which the λ^2 factor in (2.37) can also be accounted for.

Specular Model

A specular, or glint, target is defined to be one that preserves the spatial coherence of the incident beam in the reflected beam after reflection. The complex reflection coefficient of such a target is

$$\mathbf{T}(\bar{\rho}) = \sqrt{\mathcal{T}_s(\bar{\rho})} \exp(jk2z(\bar{\rho}) + j\psi). \quad (2.41)$$

Now, the height profile $z(\bar{\rho})$ is deterministic and smoothly varying relative to the radar's wavelength. The extent of the target is the region over which the reflective intensity $\mathcal{T}_s(\bar{\rho})$ is not negligible. These two terms completely characterize the geometry of the target. Note that the target height interpretation is precise under the paraxial limit.

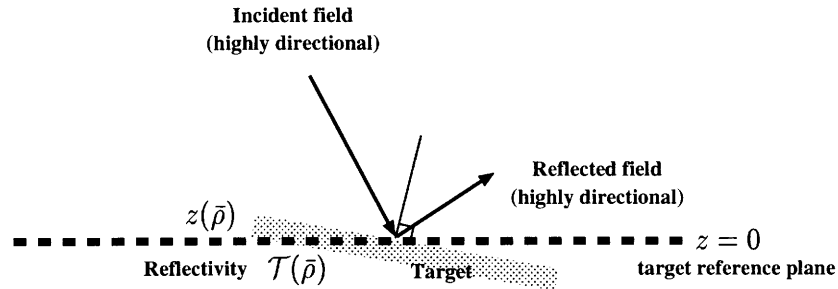


Figure 2-5: Smooth surface gives specular reflections

In general, the nominal altitude of the radar from the target reference plane cannot be known down to sub-wavelength resolution. There will therefore be a random but constant phase error ψ , which has a uniform probability density over $[0, 2\pi)$, for the unknown absolute altitude of the airplane. This is reasonable as long as this phase, generally a function of time, either does not change much or can be accurately tracked using an Inertial Navigation System (INS) or the Global Positioning System (GPS), etc. [14] throughout the dwell time, i.e., the time interval in which a target is illuminated by the radar footprint.

We shall summarize this section with several comments about the specular and diffuse models.

- How a specular target transforms the coherence and directionality of the impinging beam is captured in the phase function of the specular model, whereas the statistical characterization of the diffuse target (2.35-2.37) guarantees loss of coherence or directionality of the reflected beam.

- Strong height fluctuations in the diffuse target can overwhelm the geometric interpretation of the phase (2.34), which assumes no steep edges in the target. But the diffuse model is still sufficient to characterize the collection of random phase delays at the target, which can be used to argue that the diffuse model has already incorporated some multiple-scattering effects in the target through the randomness of its phase delay. This simple specular model, however, explicitly ignores multiple scattering. Both models fail to treat any shadowing behavior.
- In our system, the radar is always down-looking, and our targets are modeled for that mode of operation. But in the general case, a more sophisticated model has to be used if the radar operates at a different look-angle or if the objects have steep edges.
- It is possible for a target to exhibit both specular and diffuse reflections. In that case, the complex reflection coefficient will have both deterministic and random components:

$$\mathbf{T}(\bar{\rho}) = \mathbf{T}_s(\bar{\rho}) + \mathbf{T}_d(\bar{\rho}) \quad (2.42)$$

- Specification of a purely diffuse target implies substituting a particular diffuse reflectivity function for $\mathcal{T}_d(\bar{\rho})$ in (2.37) whereas specification of a purely specular target involves modeling both the specular reflectivity $\mathcal{T}_s(\bar{\rho})$ and the target geometry $z(\bar{\rho})$ in (2.41).

We have to emphasize that *neither* the target height interpretation (2.18) *nor* the limiting case of the Gaussian-Schell model (Appendix A) is a rigorous derivation of our diffuse and specular models. But these interpretations give reasonable physical insight into what the models, while mathematically tractable, do and do not represent.

2.2.2 General Linear Model

The general impulse response model will be needed to model a dihedral and a trihedral, where the multiplicative model becomes insufficient. There is no general interpretation of the possibly space-varying linear impulse response model and we will defer discussion of it until the next chapter when we have specific target behaviors that we wish to model.

Chapter 3

Target Signatures and Returns

In this chapter, we shall study the signatures of a repertoire of targets – both diffuse and specular – by specializing the functional forms of the general models we developed in the previous chapter (2.16, 2.18). We then examine their radar returns to gain an understanding of the influence of target geometry and surface characteristics on the returns. These target models and returns will be used heavily in the later development of various methods of radar return processings.

We will start with two types of diffuse targets – uniform clutter and finite-size diffuse target, because they are simple and because the general diffuse model was studied in [21]. Then we will move on to a finite-size specular mirror, which has a number of geometric parameters. Finally, we will study some multiple-bounce specular reflectors: a dihedral and a trihedral.

Without losing any generality for our analysis of the target signatures and their returns, we have conveniently picked our coordinate system such that all the targets are situated at the origin on the target reference plane ($z = 0$.) This, however, will affect our assessment of target detection performance in the later chapters because it implies that we have prior knowledge of the location of the target.

3.1 Uniform Clutter

We would like to model natural clutter (such as grass background) whose extent is much larger than the man-made targets of interest. Instead of assuming any arbitrary (thus possibly unreasonable) geometric shape to this natural clutter, we will assume that it is statistically uniform throughout the entire target region. It is within this natural clutter that our man-made, specular targets may be embedded.

The uniform diffuse clutter is characterized by

$$\langle \mathbf{T}(\bar{\rho})\mathbf{T}^*(\bar{\rho}_1) \rangle = \lambda^2 \mathcal{T}_{uc} \delta(\bar{\rho} - \bar{\rho}_1). \quad (3.1)$$

Using (2.32, 2.8, and 2.5), the average power of the return signal from such a clutter is

$$\langle |\mathbf{y}_{uc}(t)|^2 \rangle = P_{tr} \frac{a_x a_y}{L^2} \pi \mathcal{T}_{uc} \equiv C_{tr} C_{uc} \quad (3.2)$$

where the constants

$$C_{tr} \equiv P_{tr} \left(\frac{k^2 a_x a_y}{2\pi L^2} \right)^2 \quad (3.3)$$

$$C_{uc} \equiv \lambda^2 \mathcal{T}_{uc} \pi \frac{L^2}{k^2 a_x a_y} \quad (3.4)$$

have been chosen for our later convenience. This diffuse clutter return is a wide-sense stationary random process because its correlation function is easily shown to be

$$\langle \mathbf{y}_{uc}(t) \mathbf{y}_{uc}^*(u) \rangle = C_{tr} C_{uc} \exp \left(-\frac{v^2}{a_x^2} (t-u)^2 \right) \quad (3.5)$$

$$= \langle |\mathbf{y}_{uc}(t)|^2 \rangle \exp \left(-\frac{v^2}{a_x^2} (t-u)^2 \right) \quad (3.6)$$

which is a function of only the time difference $t - u$. The power density spectrum of the uniform clutter return is

$$S_{\mathbf{y}_{uc}}(f) = C_{tr} C_{uc} \sqrt{\frac{\pi a_x^2}{v^2}} \exp \left[-\frac{a_x^2}{v^2} (\pi f)^2 \right] \quad (3.7)$$

The bandwidth of the spectrum is proportional to v , because the chirp slope is proportional to v . Also, the bandwidth is a decreasing function of the antenna's aperture size, because a large antenna has a narrow beam pattern in the down-looking direction and hence receives little high chirp-frequency power.

3.2 Finite-size Diffuse Target

For man-made clutter, such as houses, and natural diffuse objects, such as trees and shrubs, the targets have finite extents. For mathematical tractability, we shall use an elliptical Gaussian to model the finite dimensions of these targets.

$$\langle \mathbf{T}(\bar{\rho}) \mathbf{T}^*(\bar{\rho}_1) \rangle = \lambda^2 \mathcal{T}_{dt} \exp \left(-\frac{2x^2}{\rho_x^2} - \frac{2y^2}{\rho_y^2} \right) \delta(\bar{\rho} - \bar{\rho}_1). \quad (3.8)$$

We have assumed elliptical symmetry and perfect alignment of the principal axes with the airplane's along- and across-track directions not because this is generally true, but because this allows us to examine the the along-track and across-track effects separately.

The average power of the radar return from this finite diffuse target is

$$\langle |\mathbf{y}_{dt}(t)|^2 \rangle = C_{tr} C_{dt} \exp \left[-\frac{t^2}{\Delta t_{dt}^2} \right] \quad (3.9)$$

$$C_{dt} = \lambda^2 \mathcal{T}_{dt} \pi \frac{\rho_x \rho_y}{2} \quad (3.10)$$

$$\Delta t_{dt}^2 = \frac{L^2}{k^2 v^2 a_x^2} \quad (3.11)$$

The duration of the intensity Gaussian, Δt_{dt} , can be considered as the time resolution for locating the target. We see that the diffuse target, being an isotropic scatterer, gives a return of a duration equal to the period over which it is illuminated,

$$\Delta t_{dt} = \frac{L}{k a_x v} = T_{dw} \quad (3.12)$$

i.e., the full dwell time of an unresolved target $\left(\rho_x^2 \ll \left(\frac{L}{k a_x} \right)^2 \right)$, as was seen in Chapter 1 for the point scatterer case. Furthermore, the correlation function of the diffuse target return is

$$\begin{aligned} \langle \mathbf{y}_{dt}(t) \mathbf{y}_{dt}^*(u) \rangle = C_{tr} C_{dt} \exp \left[-\frac{k^2 \rho_x^2 v^2}{2L} (t-u)^2 \right] \\ \exp \left[-\left(\frac{k^2 a_x^2 v^2}{2L^2} - j \frac{k v^2}{L} \right) t^2 - \left(\frac{k^2 a_x^2 v^2}{2L^2} + j \frac{k v^2}{L} \right) u^2 \right] \end{aligned} \quad (3.13)$$

which can be thought of as a combination of a stationary component ($(t-u)^2$ term), and a non-stationary component (t^2, u^2 terms) due to the finite illumination period. The stationary component can be decorrelated by increasing the target size, because more facets of random heights on the target surface are contributing to the target return such that a small change in the receive antenna's beam pattern, due to the radar motion in a short period of time, gives an uncorrelated "snapshot" of the widely fluctuating target surface.

The average energy received from the diffuse target return is

$$\langle E_{y_{dt}} \rangle = \int \langle |\mathbf{y}_{dt}(t)|^2 \rangle dt = C_{tr} C_{dt} \sqrt{\pi} \Delta t_{dt} \quad (3.14)$$

$$= P_{tr} \frac{k a_x a_y^2}{L^3 v} \pi^{3/2} \mathcal{T}_{dt} \frac{\rho_x \rho_y}{2} \quad (3.15)$$

It is a product of the transmitted power P_{tr} , radar return duration Δt_{dt} , and a dimensionless constant comprising the parameters of both the radar and the target.

3.3 Specular Mirror

For our man-made targets, we will use a multiplicative specular reflector model.

$$\mathbf{T}_{sm}(\bar{\rho}) = \underbrace{\sqrt{\mathcal{T}_{sm}}}_1 \exp \left[\underbrace{-\frac{x^2}{\rho_x^2} - \frac{y^2}{\rho_y^2}}_2 \underbrace{+ j2k\bar{\phi} \cdot \bar{\rho}}_3 \underbrace{+ j\frac{kx^2}{R_x} + j\frac{ky^2}{R_y}}_4 \underbrace{+ j\psi}_5 \right] \quad (3.16)$$

This specular mirror has

1. a positive specular reflectivity \mathcal{T}_{sm}
2. finite dimensions ρ_x, ρ_y , satisfying the far field assumption $\frac{k\rho_x^2}{L} \ll 1$, $\frac{k\rho_y^2}{L} \ll 1$
3. a tilt vector $\bar{\phi} = [\phi_x \ \phi_y]^T$, with $|\phi_x| \ll 1$, $|\phi_y| \ll 1$ as the tilt slopes with respect to the \hat{x} and \hat{y} axes They can also be interpreted as the tilt angles between the mirror and the target reference plane (since $\tan \phi \approx \phi$ for $|\phi| \ll 1$ as in Figure 3-1.)
4. radii of curvature, R_x, R_y , along the \hat{x} and \hat{y} axes. Because of the finite target dimensions, the curvature terms only exists for approximately $|x| \leq \rho_x$ and $|y| \leq \rho_y$. As shown in Figure 3-1, if $R_x > 0, R_y > 0$, the mirror is a convex \cap paraboloid. If $R_x < 0, R_y < 0$, the mirror is convex \cup . If R_x, R_y have opposite signs, the mirror is a saddle. To avoid the degeneracy of having the mirror larger than the spheres that circumscribe the curvatures, we also have the place the restriction of $2\rho_x < R_x, 2\rho_y < R_y$.
5. a random phase, with a uniform density over $[0, 2\pi)$, for the uncertainty in the absolute altitude of the radar

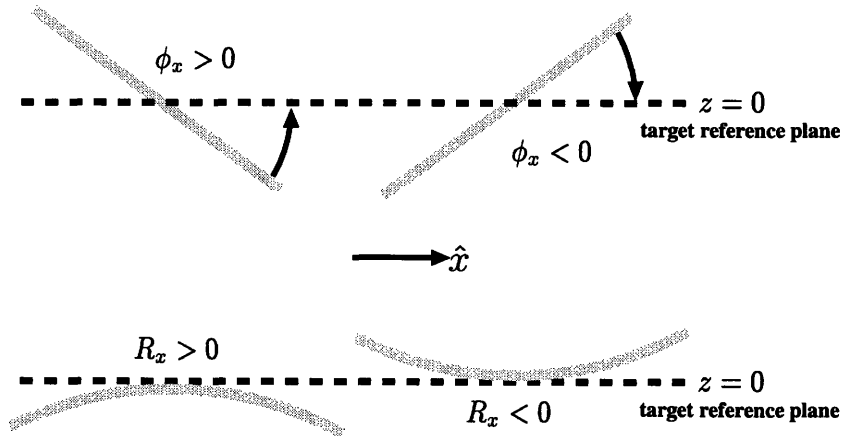


Figure 3-1: Geometry of the specular mirror

Similar to the diffuse target, this mirror has elliptical symmetry and perfect alignment with the radar's axes, again assumed to permit separation of the effects of the along-track and across-track target parameters. The above model is closely related to the thin lens model of Fourier optics [9].

Because specular models are spatially coherent, we can also analyze the target by taking the Fourier transform of our input/output relation (2.18)

$$\tilde{\mathbf{E}}_{rfl}(\bar{s}, t) = \int \tilde{\mathbf{T}}_{sm}(\bar{s} - \bar{s}_1) \tilde{\mathbf{E}}_{il}(\bar{s}_1, t) d\bar{s}_1 \quad (3.17)$$

which becomes a convolution in the spatial frequency domain of the illuminating field with the specular mirror's signature $\tilde{\mathbf{T}}_{sm}(\bar{s})$,

$$\tilde{\mathbf{T}}_{sm}(\bar{s}) = \int \mathbf{T}_{sm}(\bar{\rho}) e^{-j2\pi\bar{s}\cdot\bar{\rho}} d\bar{\rho} \quad (3.18)$$

$$\begin{aligned} &= \pi \tilde{\rho}_x \tilde{\rho}_y \sqrt{1 + j \frac{k\rho_x^2}{R_x}} \sqrt{1 + j \frac{k\rho_y^2}{R_y}} \exp \left[- \left(\pi \left(s_x - \frac{2\phi_x}{\lambda} \right) \tilde{\rho}_x \right)^2 \left(1 + j \frac{k\rho_x^2}{R_x} \right) \right] \\ &\quad \exp \left[- \left(\pi \left(s_y - \frac{2\phi_y}{\lambda} \right) \tilde{\rho}_y \right)^2 \left(1 + j \frac{k\rho_y^2}{L} \right) \right] \end{aligned} \quad (3.19)$$

where

$$\tilde{\rho}_x = \frac{\rho_x}{\sqrt{1 + \left(\frac{k\rho_x^2}{R_x} \right)^2}}, \quad \tilde{\rho}_y = \frac{\rho_y}{\sqrt{1 + \left(\frac{k\rho_y^2}{R_y} \right)^2}} \quad (3.20)$$

are the effective target dimensions because the curvatures of the target effectively reduce the target's surface area facing the down-looking radar. These effective dimensions do not depend on the directions (signs) of the curvatures, and converge to the actual target dimensions for planar mirrors, i.e.,

$$\lim_{R_x \rightarrow \pm\infty} \tilde{\rho}_x = \rho_x, \quad \lim_{R_y \rightarrow \pm\infty} \tilde{\rho}_y = \rho_y \quad (3.21)$$

The specular mirror's spatial frequency signature is a complex Gaussian of widths $\tilde{\rho}_x, \tilde{\rho}_y$ centered at the frequencies $\frac{2\phi_x}{\lambda}$ and $\frac{2\phi_y}{\lambda}$ respectively. We see that the larger the effective size of the mirror, $\tilde{\rho}_x, \tilde{\rho}_y$, the sharper this Gaussian is, corresponding to the fact that a directional incident plane wave would stay directional after reflection (convolving with a sharp function results in little blurring or spreading.) The direction of this wave, however, will be shifted by the center frequencies of this Gaussian, corresponding to Snell's law of reflection (the factors of 2 in the center frequencies are a result of the sums of the angles of incidence and the angles of reflection, which are equal to ϕ_x and ϕ_y for the two transverse coordinates.)

We shall examine the radar returns of this specular mirror by using (2.32, 2.8, and 2.5). Before we present the most general results, we will first investigate the return of a special case to gain insight into the physics.

3.3.1 Target Return (Special Case: No Curvature, Large Mirror)

In the case of a flat specular mirror

$$R_x \rightarrow \pm\infty, R_y \rightarrow \pm\infty \quad (3.22)$$

that is large compared to the radar aperture

$$2\rho_x^2 \gg a_x^2, \quad (3.23)$$

the specular mirror return is

$$\mathbf{y}'_{sm}(t) = \sqrt{C_{tr}C'_{sm}} \exp \left[j \frac{kv^2}{L} (t - t'_c)^2 - \frac{(t - t'_i)^2}{2\Delta t'_{sm}} + j\psi' \right] \quad (3.24)$$

$$\Delta t'_{sm}{}^2 = \frac{L^2}{k^2 v^2 2\rho_x^2} \quad (3.25)$$

$$t'_i = \frac{\phi_x L}{v} \quad (3.26)$$

$$t'_c = -\frac{\phi_x L}{v} \left(\frac{k\rho_x^2}{L} \right)^2 \quad (3.27)$$

$$\sqrt{C'_{sm}} = \sqrt{\mathcal{T}_{sm} \pi \rho_x \rho_y} \exp \left[-\frac{1}{2} (k\phi_x a_x)^2 - (k\phi_y \rho_y)^2 \right] \quad (3.28)$$

We have lumped all the constant phase terms into our unknown phase ψ' , since we do not care about the absolute phase. The density of ψ' will stay uniform over $[0, 2\pi)$. We see that the radar return is proportional to some radar transmission parameters (3.3), the square root of the target's specular reflectivity, \mathcal{T}_{sm} , and the target's area, $\pi\rho_x\rho_y$. The time dependent part of the signal comprises a chirp of instantaneous frequency $-\frac{2v^2}{\lambda L}(t - t'_c)$, (hence centered at the chirp time center t'_c), and an intensity Gaussian of width $\Delta t'_{sm}$ centered at t'_i . It is common knowledge that the larger a plane mirror, the better it preserves the directionality of an incident plane wave. This mirror is large enough (3.23) such that the peak of the reflected beam obeys Snell's law of reflection exactly, and occurs at the time t'_i when the radar illuminates the mirror at normal incidence. However, the mirror is far from being an infinite plane mirror which does not spread the incident beam after reflection – the mirror's finite size gives this peak a width $\Delta t'_{sm}$ inversely proportional to the mirror's azimuth dimension ρ_x . This width is much narrower than that of a diffuse target return (3.11, 3.23), hence the “broadside flash” phenomenon when the radar is at a position such that its line-of-sight is aligned with the mirror's surface normal. (Figure 3-2)

The chirp time center is negligible compared to the intensity time center, $|t'_c| \ll |t'_i|$, but is only

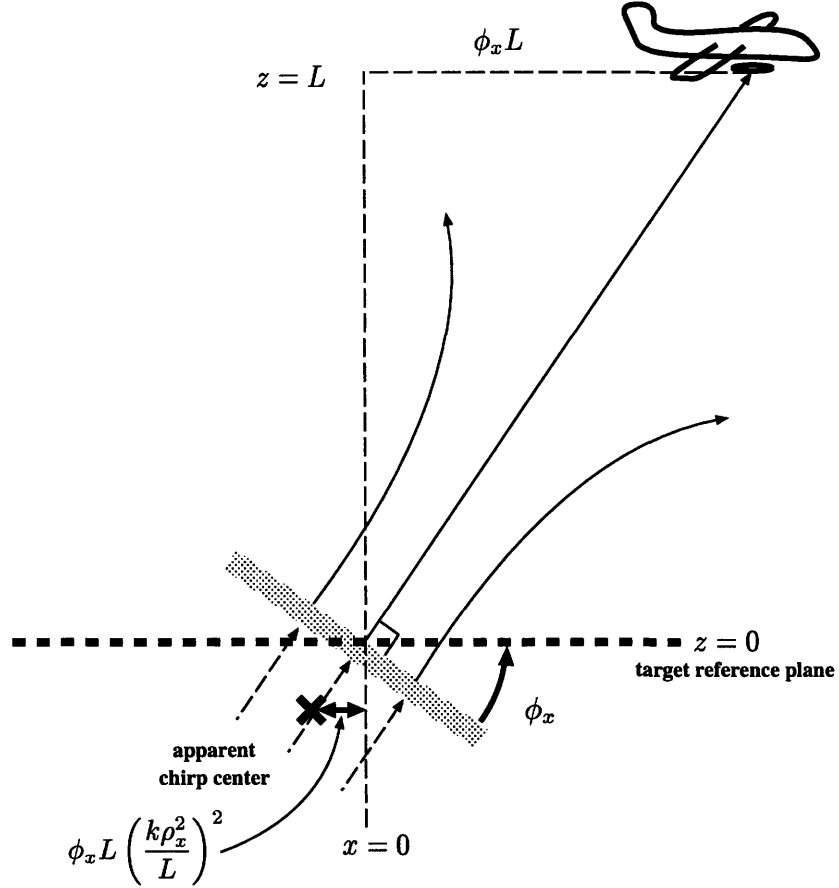


Figure 3-2: A tilted mirror offsets the broadside flash and the chirp center

negligible itself if $t'_c \ll \Delta t'_{sm}$, or equivalently,

$$k|\phi_x|a_x \left(\frac{k\rho_x^2}{L} \right)^2 \ll 1 \quad (3.29)$$

Because of the separation of the chirp center and the intensity center in the radar return, it is possible in principle to estimate the target's tilt angle based on the difference between the intensity and the chirp centers. If these two centers do not separate, it would be impossible to tell apart a weakly reflecting target right along the radar's line-of-sight, or a strongly reflecting tilted target whose normal tilts toward the radar when it is far from the radar's line-of-sight.

The fact that the reflected beam is incorrectly directed by the mirror's tilt for the always-down-looking radar causes the exponential attenuation (in $\sqrt{C_{sm}}$.) The attenuation due to the azimuth tilt $|\phi_x|$ is limited by the receive antenna gain in the azimuth direction of normal incidence to the mirror when the radar is along the mirror's normal. Because the radar is confined to the same across-track coordinate as the mirror, the attenuation due to $|\phi_y|$ is limited by the mirror's back-scattering gain in the across-track direction back along the direction of incidence. These attenuations are increasing functions (more severe attenuations) of a_x and ρ_y , because the larger these parameters, the sharper

the receiver and back-scattering beam patterns are, respectively, and the more weakly the radar receives an incorrectly directed beam.

3.3.2 Target Return (General Case)

$$\mathbf{y}_{sm}(t) = \sqrt{C_{tr}C_{sm}} \exp \left[j \frac{kv^2}{L} (t - t_c)^2 - \frac{(t - t_i)^2}{2\Delta t_i^2} + j\psi' \right] \quad (3.30)$$

$$\Delta t_{sm}^2 = \frac{L^2}{k^2 v^2 (2\tilde{\rho}_x^2 + a_x^2)} \quad (3.31)$$

$$t_i = \frac{\phi_x L}{v} \frac{2\tilde{\rho}_x^2}{2\tilde{\rho}_x^2 + a_x^2} \left(1 - \frac{ka_x^2}{2L} \frac{k\rho_x^2}{R_x} \right) \quad (3.32)$$

$$t_c = -\frac{\phi_x L}{v} \frac{k\tilde{\rho}_x^2}{L} \left(\frac{ka_x^2}{2L} + \frac{k\rho_x^2}{L} + \frac{k\rho_x^2}{R_x} \right) \quad (3.33)$$

$$\sqrt{C_{sm}} = \sqrt{T_{sm}} \pi \sqrt{\rho_x \tilde{\rho}_x \rho_y \tilde{\rho}_y} \exp \left[-\frac{(k\phi_x \tilde{\rho}_x a_x)^2}{2\tilde{\rho}_x^2 + a_x^2} - (k\phi_y \tilde{\rho}_y)^2 \right] \quad (3.34)$$

Aside from the expressions for t_i and t_c , the curvatures enter the radar return only through $\tilde{\rho}_x, \tilde{\rho}_y$ (3.20.) The effective target area is now $\pi \sqrt{\rho_x \tilde{\rho}_x \rho_y \tilde{\rho}_y}$.

Because the mirror is not necessarily large, the way the mirror reflects the incident beam does not obey Snell's law completely and the intensity time center becomes an increasing function of the target's effective azimuth dimension $\tilde{\rho}_x$, approaching asymptotically to the geometric limit of $\frac{\phi_x L}{v}$ as $\tilde{\rho}_x$ increases (if we assume the $\frac{k\rho_x^2}{R_x}$ term is negligible for the moment.) One can interpret this as saying that the effective normal of the mirror points somewhere between the up-looking direction and the actual normal, which is perpendicular to the tilt slopes. Now this effective normal causes the tilt attenuation to be an effect of the combined gain patterns of both the mirror and the receive antenna (the ϕ_x exponential in $\sqrt{C_{sm}}$).

Neither of the $\frac{k\rho_x^2}{R_x}$ curvature terms in t_i and t_c is negligible in general,¹ but the difference between the intensity and the chirp centers,

$$t_i - t_c = \frac{\phi_x L}{v} \frac{2\tilde{\rho}_x^2}{2\tilde{\rho}_x^2 + a_x^2} \quad (3.35)$$

is not an explicit function of R_x .

¹The conditions for them to be negligible are

$$\begin{aligned} \frac{|\phi_x|L}{v} \frac{2\tilde{\rho}_x^2}{2\tilde{\rho}_x^2 + a_x^2} \left(\frac{ka_x^2}{2L} \right) \frac{k\rho_x^2}{R_x} &\ll \Delta t_{sm} \implies k|\phi_x|a_x \frac{k\rho_x^2}{L} \ll 1 \\ \frac{|\phi_x|L}{v} \frac{k\tilde{\rho}_x^2}{L} \frac{k\rho_x^2}{R_x} &\ll \Delta t_{sm} \implies k|\phi_x|a_x \frac{k\rho_x^2}{L} \ll 1 \end{aligned}$$

3.3.3 Target Return Frequency and Energy

We can infer from the squared magnitude of the Fourier transform of the radar return

$$|\mathbf{Y}_{sm}(f)|^2 = C_{tr}C_{sm} \frac{\pi L}{kv^2} \exp \left[-\frac{2\tilde{\rho}_x^2 + a_x^2}{v^2} \left(\pi f + \frac{kv^2}{L}(t_i - t_c) \right)^2 \right] \quad (3.36)$$

that the energy of the radar return has a bandwidth of $\sqrt{\frac{v^2}{2\tilde{\rho}_x^2 + a_x^2}}$ and is centered at the frequency $-\frac{2v^2}{\lambda L}(t_i - t_c)$. This is because the azimuth tilt of the target separates the chirp center and the intensity center of the return, causing it to include a different portion of the Doppler frequency chirp (Figure 3-3).

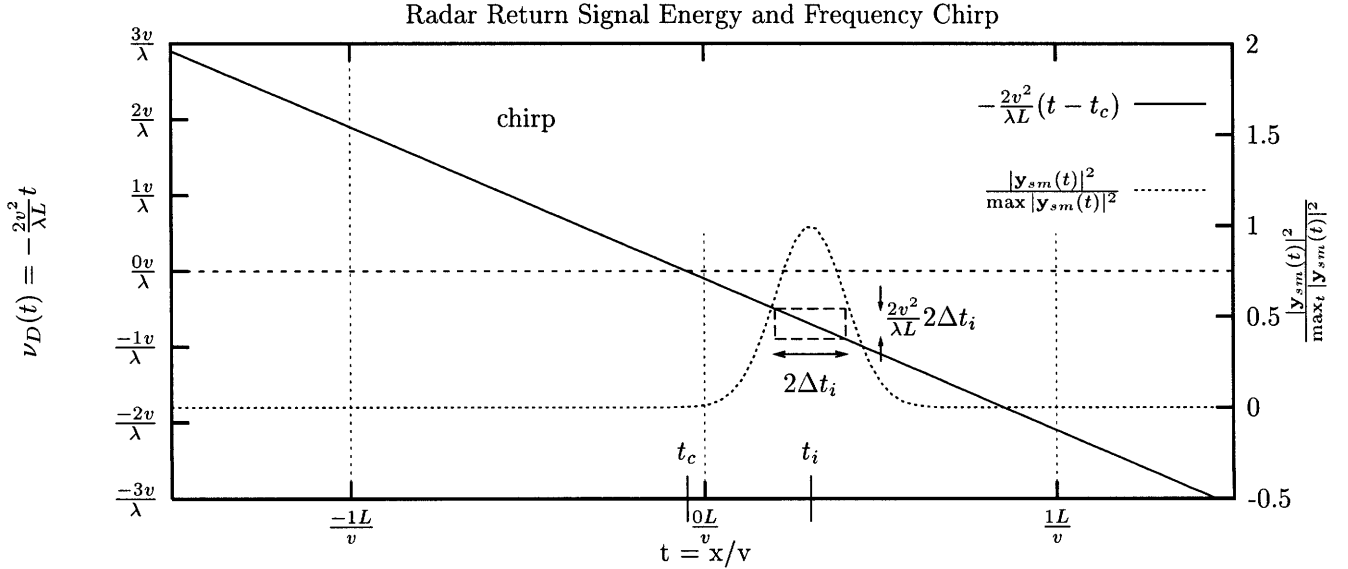


Figure 3-3: The radar return from a tilted target includes a shifted portion of the Doppler frequency chirp

Note also that both the time duration Δt_{sm} and the bandwidth are decreasing functions of the target's effective azimuth dimension $\tilde{\rho}_x$. This occurs because a larger effective target size leads to a narrower far-field diffraction pattern, which is traversed more quickly by the moving radar. Furthermore, this shorter radar-return time duration means that less frequency-chirp is incurred because the chirp bandwidth is proportional to the duration of the return. What prevents the time duration and the chirp bandwidth from both shrinking completely to zero (thus, violating the uncertainty principle) is our far-field assumption: the target cannot be infinitely large.

The total energy of the radar return is

$$E_{y_{sm}} = \int |Y_{sm}(f)|^2 df = \int |y_{sm}(t)|^2 dt \quad (3.37)$$

$$= C_{tr} C_{sm} \sqrt{\pi} \Delta t_{sm} \quad (3.38)$$

$$= P_{tr} \frac{k^3 a_x^2 a_y^2}{4L^3 v \sqrt{2\tilde{\rho}_x^2 + a_x^2}} \sqrt{\pi} T_{sm} \rho_x \tilde{\rho}_x \rho_y \tilde{\rho}_y \exp \left[-\frac{2(k\phi_x \tilde{\rho}_x a_x)^2}{2\tilde{\rho}_x^2 + a_x^2} - 2(k\phi_y \tilde{\rho}_y)^2 \right]. \quad (3.39)$$

3.4 Multiple-bounce Reflectors

Another important type of man-made specular target is the multiple-bounce reflector [31]. Specifically, we will study a right-angled dihedral and a right-angled trihedral because their special scattering properties discussed below make them integral reference devices for calibrating radar systems. We will first present the trihedral model.

3.4.1 Right-angled Trihedral

A right-angled trihedral (3 plane mirrors meeting at 90°) is also called a corner reflector. It is a 3-fold coherent reflector which, due to a triple-bounce effect shown in Figure 3-4, has the special property that no matter what angle of incidence a beam comes into interaction with the trihedral, the three-bounce reflection within the trihedral turns the illuminating beam directly backwards along the direction of incidence. If we define a “backscattering gain pattern” as the ratio of received

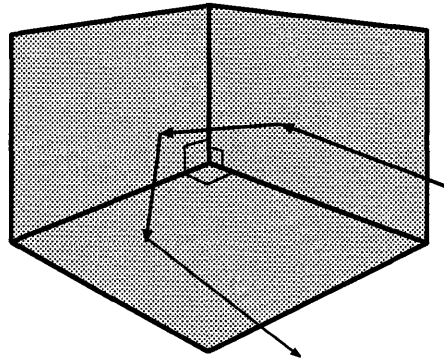


Figure 3-4: Triple-bounce effect of a trihedral

energy to transmitted energy as a function of the incident angle and the transmitter-to-receiver angle (one subtended by the lines-of-sight of the transmitter and receiver as shown in Figure 3-5), then a trihedral has a high backscattering gain pattern independent of the incident angle α but highly dependent on the transmitter-to-receiver angle β . The gain is the highest at $\beta = 0$ and close to zero otherwise. That is, the strength of the scattered beam from a trihedral has a broad incident beam angle, α , but a narrow transmitter-to-receiver beam angle β .

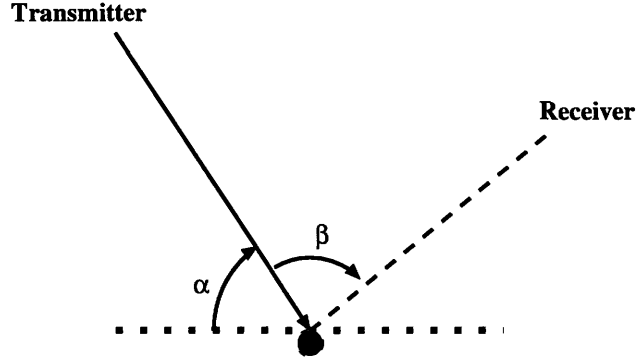


Figure 3-5: Scattering gain pattern

In other words, a right-angled trihedral's scattering behavior is such that it reverses incident plane wave's direction. Because spatial Fourier transforms of the illumination and reflected fields basically represent the plane-wave components of these fields, an ideal trihedral can be characterized by an impulse response model,

$$\mathbf{E}_{rfl}(\bar{\rho}, t) = \int \mathbf{T}(\bar{\rho}, \bar{\rho}_1) \mathbf{E}_{il}(\bar{\rho}_1, t) d\bar{\rho}_1 \quad (3.40)$$

which produces

$$\tilde{\mathbf{E}}_{rfl}(\bar{s}, t) \propto \tilde{\mathbf{E}}_{il}(-\bar{s}, t), \quad (3.41)$$

where $\tilde{\mathbf{E}}_{rfl}(\bar{s}, t)$, $\tilde{\mathbf{E}}_{il}(\bar{s}, t)$ are the transverse spatial Fourier transforms of $\mathbf{E}_{rfl}(\bar{\rho}, t)$ and $\mathbf{E}_{il}(\bar{\rho}_1, t)$ respectively, with \bar{s} representing a plane wave's transverse direction. However, a plane wave has infinite spatial extent, and to satisfy such a condition of reflection implies that the reflecting surface is also of infinite extent. To address this problem, we propose the following model:

$$\mathbf{T}_{3h}(\bar{\rho}, \bar{\rho}_1) = \sqrt{\mathcal{T}_{3h}} \exp \left[-\frac{|\bar{\rho}|^2}{\rho_T^2} + j\psi \right] \delta(\bar{\rho} + \bar{\rho}_1) \quad (3.42)$$

where ρ_T represents the finite size of the reflector (we no longer use separate ρ_x and ρ_y because the separate along-track and across-track effects on the targets are already quite apparent by now), and ψ is an appropriate phase shift as in the specular mirror.

The resulting approximation to (3.41) can be seen in

$$\mathbf{E}_{il}(\bar{\rho}_1, t) = \int \tilde{\mathbf{E}}_{il}(\bar{s}, t) e^{j2\pi\bar{s}\cdot\bar{\rho}_1} d\bar{s} \quad (3.43)$$

$$\mathbf{E}_{rf1}(\bar{\rho}, t) = \int d\bar{\rho}_1 \mathbf{T}(\bar{\rho}, \bar{\rho}_1) \int \tilde{\mathbf{E}}_{il}(\bar{s}, t) e^{j2\pi\bar{s}\cdot\bar{\rho}_1} d\bar{s} \quad (3.44)$$

$$= \int d\bar{\rho}_1 \sqrt{\mathcal{T}_{3h}} \exp\left[-\frac{|\bar{\rho}|^2}{\rho_T^2} + j\psi\right] \delta(\bar{\rho} + \bar{\rho}_1) \int \tilde{\mathbf{E}}_{il}(\bar{s}, t) e^{j2\pi\bar{s}\cdot\bar{\rho}_1} d\bar{s} \quad (3.45)$$

$$= \sqrt{\mathcal{T}_{3h}} \exp\left[-\frac{|\bar{\rho}|^2}{\rho_T^2} + j\psi\right] \int \tilde{\mathbf{E}}_{il}(-\bar{s}, t) e^{j2\pi\bar{s}\cdot\bar{\rho}} d\bar{s}. \quad (3.46)$$

Therefore, if the point of incidence of the illuminating wave is within the extent ρ_T of this trihedral, the incident wave will be completely reversed after reflection, otherwise, attenuated.

The radar return from this trihedral is

$$\mathbf{y}_{3h}(t) = \sqrt{C_{tr}C_{3h}} \exp\left[\left(j\frac{kv^2}{L} - \frac{1}{2\Delta t_{3h}^2}\right)t^2 + j\psi'\right] \quad (3.47)$$

$$\sqrt{C_{3h}} = \sqrt{\mathcal{T}_{3h}}\pi\rho_T^2 \quad (3.48)$$

$$\Delta t_i^2 = \frac{L^2}{k^2 a_x^2 v^2} \quad (3.49)$$

We see that the trihedral return has the same full-dwell duration as that of a point scatterer or a diffuse target because all these reflectors' backscattering patterns are independent of the illumination direction.

3.4.2 Right-angled Dihedral

A right-angled dihedral is a 2-fold reflector (2 plane mirrors meeting at 90°) that turns an incident beam directly backwards in the same manner as a trihedral only in the direction perpendicular to its crease, but acts like a plane mirror in the direction along its crease.

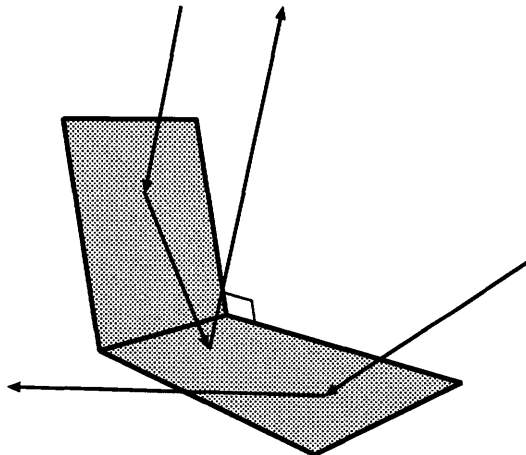


Figure 3-6: Double-bounce and single-bounce effects of a dihedral

Provided that a dihedral is located in an orientation such that θ is the angle the across-crease direction of the dihedral makes with \hat{x} -axis, we expect

$$\mathbf{E}_{rfl}(\bar{\rho}, t) = \sqrt{\mathcal{T}_{2h}} \exp \left[-\frac{|\bar{\rho}|^2}{\rho_T^2} + j\psi \right] \int \tilde{\mathbf{E}}_{il}(\bar{\mathbf{Q}}\bar{s}, t) e^{j2\pi\bar{s}\cdot\bar{\rho}_1} d\bar{s} \quad (3.50)$$

where

$$\bar{\mathbf{Q}} \equiv \bar{\mathbf{R}}(\theta)\bar{\mathbf{F}}\bar{\mathbf{R}}(-\theta) = \bar{\mathbf{Q}}^T = \bar{\mathbf{Q}}^{-1} \quad (3.51)$$

$$\bar{\mathbf{R}}(\theta) = \begin{bmatrix} \cos \theta & -\sin \theta \\ \sin \theta & \cos \theta \end{bmatrix}, \quad \bar{\mathbf{F}} = \begin{bmatrix} -1 & 0 \\ 0 & 1 \end{bmatrix} \quad (3.52)$$

$$\bar{\mathbf{Q}} = \begin{bmatrix} -\cos 2\theta & -\sin 2\theta \\ -\sin 2\theta & \cos 2\theta \end{bmatrix} \quad (3.53)$$

We have used $\bar{\mathbf{R}}(\pm\theta)$ to transform the radar's transverse coordinates to and from the coordinate system of the dihedral, and used $\bar{\mathbf{F}}$ to flip the spatial frequencies of the illuminating beam in the across-crease direction of the dihedral. This can be achieved with the model:

$$\mathbf{T}_{2h}(\bar{\rho}, \bar{\rho}_1) = \sqrt{\mathcal{T}_{2h}} \exp \left[-\frac{|\bar{\rho}|^2}{\rho_T^2} + j\psi \right] \delta(\bar{\rho}_1 - \bar{\mathbf{Q}}\bar{\rho}). \quad (3.54)$$

Then

$$\mathbf{E}_{rfl}(\bar{\rho}, t) = \int d\bar{\rho}_1 \sqrt{\mathcal{T}_{2h}} \exp \left[-\frac{|\bar{\rho}|^2}{\rho_T^2} + j\psi \right] \delta(\bar{\rho}_1 - \bar{\mathbf{Q}}\bar{\rho}) \int \tilde{\mathbf{E}}_{il}(\bar{s}, t) e^{j2\pi\bar{s}\cdot\bar{\rho}_1} d\bar{s} \quad (3.55)$$

$$= \sqrt{\mathcal{T}_{2h}} \exp \left[-\frac{|\bar{\rho}|^2}{\rho_T^2} + j\psi \right] \int \tilde{\mathbf{E}}_{il}(\bar{s}, t) e^{j2\pi\bar{s}\cdot\bar{\mathbf{Q}}\bar{\rho}} d\bar{s} \quad (3.56)$$

$$= \sqrt{\mathcal{T}_{2h}} \exp \left[-\frac{|\bar{\rho}|^2}{\rho_T^2} + j\psi \right] \int \tilde{\mathbf{E}}_{il}(\bar{\mathbf{Q}}\bar{s}, t) e^{j2\pi\bar{s}\cdot\bar{\rho}} d\bar{s} \quad (3.57)$$

and we have arrived at the desired scattering behavior (3.50): if the point of incidence of the illuminating wave is within the extent ρ_T of this dihedral, the incident wave will be completely reversed in the across-crease direction after reflection, otherwise, attenuated.

The radar return of a dihedral is

$$\mathbf{y}_{2h}(t) = \sqrt{C_{tr}C_{2h}} \exp \left[\left(j\frac{kv^2}{L} - \frac{1}{2\Delta t_{2h}^2} \right) t^2 + j\psi' \right] \quad (3.58)$$

$$\sqrt{C_{2h}} = \sqrt{\mathcal{T}_{2h}\pi\rho_T^2} \quad (3.59)$$

$$\Delta t_{2h}^2 = \frac{L^2}{k^2v^2(a_x^2 + \rho_T^2(1 - \cos 2\theta))} \quad (3.60)$$

Two special cases of this dihedral are noteworthy. When $\theta = 0$, the crease lies perpendicular to

the azimuth \hat{x} . The return duration is the full dwell for an unresolved target $\frac{L}{ka_x v}$, just like the trihedral. When $\theta = \pi/2$, however, the dihedral acts only like a plane mirror: the return duration is then short, $\Delta t_i = \frac{L}{k\sqrt{a_x^2 + 2\rho_T^2}v}$.

We can also think of the dihedral as an untilted plane mirror with effective dimension

$$\tilde{\rho}_T = \rho_T \sqrt{\frac{1 - \cos 2\theta}{2}} = \rho_T \sin \theta. \quad (3.61)$$

But this shortening of the effective dimension due to misalignment of the dihedral's across-crease direction with the azimuth does not show up in $\sqrt{C_{2h}}$.

In this chapter, we have studied a number of simple target models: a uniform clutter, a diffuse target, a specular mirror, a trihedral, and a dihedral. The target returns of these models are summarized in the following table.

Target	Return Duration	Target Parameters	Note
Point Scatterer	$\Delta t_{pt} = \frac{L}{ka_x v}$	–	
Uniform clutter	∞	$C_{uc} = \lambda^2 \mathcal{T}_{uc} \pi \frac{L^2}{k^2 a_x a_y}$	
Diffuse Target	$\Delta t_{dt} = \frac{L}{ka_x v}$	$C_{dt} = \lambda^2 \mathcal{T}_{dt} \pi \frac{\rho_x \rho_y}{2}$	
Specular Mirror	$\Delta t_{sm} = \frac{L}{k\sqrt{2\tilde{\rho}_x^2 + a_x^2}v}$	$C_{sm} = \mathcal{T}_{sm} \pi^2 \rho_x \tilde{\rho}_x \rho_y \tilde{\rho}_y$	$t_i - t_c = \frac{\phi_x L}{v} \frac{2\tilde{\rho}_x^2}{2\tilde{\rho}_x^2 + a_x^2}$
Dihedral	$\Delta t_{2h} = \frac{L}{k\sqrt{2\rho_T^2 \sin^2 \theta + a_x^2}v}$	$C_{2h} = \mathcal{T}_{2h} \pi^2 \rho_T^4$	
Trihedral	$\Delta t_{3h} = \frac{L}{k\sqrt{2\rho_T^2 + a_x^2}v}$	$C_{3h} = \mathcal{T}_{3h} \pi^2 \rho_T^4$	

Table 3.1: Summary of target returns

Chapter 4

Synthetic Aperture Radar and Multi-resolution Processing

We have examined the return signals of the individual targets in the previous chapters by assuming that they are all located at the origin of the target terrain. In practice when we do not have this prior information about their locations, we may use the peak power in the return signal, i.e. $|\mathbf{y}(t)|^2$, to locate these targets. How well we can locate a target depends on how narrow, or high-resolution, the peak in the return is. We note that the diffraction-limited resolution in time of some of these target return signals are at the maximum dwell time $T_{dw} = \frac{L}{ka_x v}$, corresponding to a resolution in space $vT_{dw} = \frac{L}{ka_x}$, which is a rather large uncertainty for many applications. The specular mirror does have a narrower time resolution due to its spatial coherence. But in either case, the resolution can be improved by coherently integrating a return over the dwell time – by compensating for the motion-induced frequency chirp, we can obtain a much sharper peak, or a higher resolution.

We shall now revisit SAR processing that we first introduced in Chapter 1 using the target models, radar system, and target returns that we developed in the last 2 chapters.

4.1 Conventional SAR Processing

First, we would like to use our radar system formulation to rigorously re-derive results from Chapter 1 to demonstrate SAR's resolution enhancement capabilities for a point target. In particular, we will examine the target return of a point target derived from our planar, uncurved specular mirror model by shrinking the mirror to a negligible size,

$$\mathbf{T}_{pt}(\bar{\rho}) \equiv \mathbf{T}_{sm}(\bar{\rho} - \bar{\rho}_0), \quad 2\rho_x^2 \ll a_x^2 \quad (4.1)$$

That is, the point target is located at $\bar{\rho}_o = [x_o \ 0]^T$, where x_o is an unknown parameter that we want to estimate. Using (3.30), we get

$$\mathbf{y}_{pt} = \sqrt{C_{tr}C_{pt}} \exp \left[\left(j \frac{kv^2}{L} - \frac{1}{2\Delta t_{pt}^2} \right) \left(t - \frac{x_o}{v} \right)^2 + j\psi \right] \quad (4.2)$$

where

$$\Delta t_{pt} = T_{dw} = \frac{L}{ka_x v} \quad (4.3)$$

and C_{pt} is a constant that does not concern us. The target return peaks at x_o/v corresponding to where the target is. In the presence of additive white Gaussian receiver noise $\mathbf{w}(t)$ in the radar return, as is usually the case, optimal estimation (minimum variance unbiased estimation) of the location of the target from this signal would involve a matched filter [28] (Figure 4-1), because such a structure optimizes the output signal-to-noise ratio for a signal-in-Gaussian-noise problem. In the

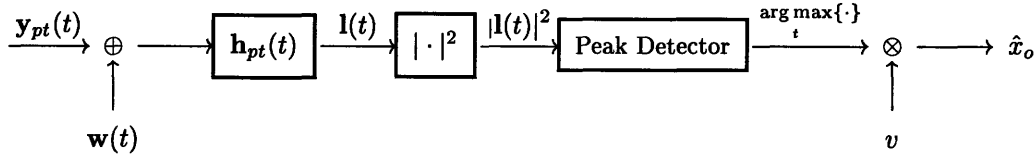


Figure 4-1: Optimal receiver for estimating the target's location

diagram,

$$\mathbf{h}_{pt}(t) = \exp \left(-j \frac{kv^2}{L} - \frac{k^2 a_x^2 v^2}{2L^2} \right) t^2 \quad (4.4)$$

$$\propto \mathbf{y}_{pt}^*(-t) \Big|_{x_o=0} \quad (4.5)$$

is our matched filter, which is proportional to the unshifted, time-reversed, and complex-conjugated version of the target return. \hat{x}_o is the location estimate.

Reference [21] took a different approach to arrive at the same filter, which we shall call the “conventional imager” from now on, because it is conventionally used to process the target return to obtain a high-resolution SAR image (Figure 4-2.)

$$\mathbf{h}_{ci}(t) \equiv \mathbf{h}_{pt}(t) = \exp \left(-j \frac{kv^2}{L} - \frac{1}{2T_{dw}^2} \right) t^2 \quad (4.6)$$

Physically, this filter matches the frequency composition of the point target return exactly and

therefore maximizes the peak magnitude of its expected output,

$$\langle \mathbf{I}(t) \rangle = \mathbf{l}_{y_{pt}}(t) = \mathbf{y}_{pt}(t) * \mathbf{h}_{ci}(t) \quad (4.7)$$

$$|\mathbf{l}_{y_{pt}}(t)|^2 = C_{tr}C_{pt}\sqrt{\pi}T_{dw} \exp \left[-\frac{2v^2}{a_x^2} \left(t - \frac{x_o}{v} \right)^2 \right]. \quad (4.8)$$

The peak of $|\mathbf{l}_{y_{pt}}(t)|^2$ occurs at $t = x_o/v$, which is shown in [28] to give x_o as the expected location estimate (i.e. the estimator is unbiased.)

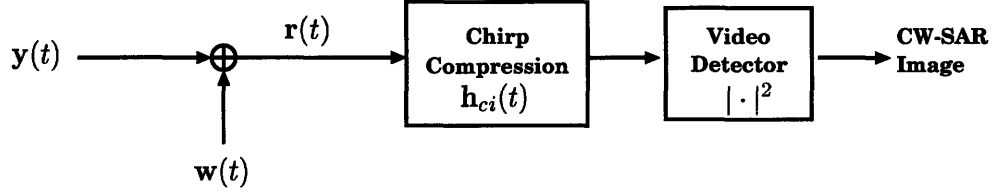


Figure 4-2: Conventional-Imager Receiver Structure

If we define resolution as the width of the Gaussian, $|\mathbf{l}_{y_{pt}}(t)|^2$, because it roughly represents how well we can locate this peak, then

$$t_{res} = \frac{a_x}{v\sqrt{2}} \ll T_{dw} \quad (4.9)$$

The last inequality is true because of the Fraunhofer far field assumption on the radar. The filter $\mathbf{h}_{ci}(t)$ can also be interpreted as a bandpass filter centered at the IF frequency ($f = 0$) such that it allows the time-dependent Doppler chirp frequency within the dwell time of the target return to pass through, resulting in a high-bandwidth target return signal. Because of the ability of this filter to utilize the chirp or Doppler history imparted by the known motion of the radar to the target to obtain a narrow peak in its output, it is also known as the “chirp compression” filter. The along-track resolution of our target is now

$$x_{res} \approx vt_{res} = \frac{a_x}{\sqrt{2}} \ll \frac{L}{ka_x}, \quad (4.10)$$

which is a great improvement over the diffraction-limited resolution of the size of the radar footprint.

Another interpretation of this SAR is that we have synthesized an aperture approximately equal to the distance that the plane covers during the dwell, vT_{dw} , which is much larger than the physical aperture itself. The effective footprint cast by our synthetic aperture, a limitation to our resolution, is reduced to approximately $\frac{L}{k(vT_{dw})} = a_x$.

4.2 Multi-resolution Processing

If we use a different period than T_{dw} in the filter, should the resulting output have a different bandwidth and therefore, a different and possibly finer resolution? To answer this question, we will need to examine the consequences of varying the integration duration, and hence the synthetic aperture size in (4.6).

$$\mathbf{h}_{mr}(t; \kappa) = \exp \left[\left(-j \frac{kv^2}{L} - \frac{1}{2(\kappa T_{dw})^2} \right) t^2 \right]; \quad \kappa \geq 0 \quad (4.11)$$

$$= \exp \left[\left(-j \frac{kv^2}{L} - \frac{1}{2T_{int}^2} \right) t^2 \right]; \quad T_{int} \equiv \kappa T_{dw} \quad (4.12)$$

where κ is the ratio of how much of the full dwell time we use for the coherent integration. We call this general chirp-compression filter the “multi-resolution” filter because, as we have conjectured, a different output resolution can be obtained by varying κ , or the synthetic aperture. To formally show this, we need to define a carrier-to-noise ratio performance measure as in [21].

$$\text{CNR}(t; \kappa) \equiv \frac{\langle |\mathbf{l}_y(t)|^2 \rangle}{\langle |\mathbf{l}_w(t)|^2 \rangle} \quad (4.13)$$

$$\mathbf{l}_y(t) \equiv \mathbf{y}(t) * \mathbf{h}_{mr}(t; \kappa) \quad (4.14)$$

$$\mathbf{l}_w(t) \equiv \mathbf{w}(t) * \mathbf{h}_{mr}(t; \kappa) \quad (4.15)$$

$$\text{CNR}(t; \kappa) = \frac{\langle |\mathbf{l}_y(t)|^2 \rangle}{N_o \kappa T_{dw} \sqrt{\pi}} \quad (4.16)$$

This CNR is applicable to all target returns by substituting the corresponding $\mathbf{y}(t)$. It is the ratio of the instantaneous mean power of the target return to the instantaneous mean power of the white Gaussian noise of spectral height N_o . The CNR can be interpreted as the normalized signal strength, an indication of how well we can detect and estimate the signal from the instantaneous output $\mathbf{l}_y(t)$ of the filter [28].

For the Gaussian-shaped target models we have assumed, the CNR is also a Gaussian shape.

$$\text{CNR}(t; \kappa) \propto \frac{C_{tr} C_{\text{target}} T_{int}}{N_o} \exp \left[-\frac{(vt - x^\dagger(\kappa))^2}{x_{\text{res}}^2(\kappa)} \right] \quad (4.17)$$

where C_{target} is one of the target-dependent constants listed in Table 3.1. We will define the synthetic-aperture-dependent resolution of the chirp-compressed signal output to be the spatial width of $\text{CNR}(t; \kappa)$, i.e., $x_{\text{res}}(\kappa)$.

For now, let us finish the resolution analysis of our point target with the CNR – it will be centered

at $x^\dagger = x_o$, where the target is located.

$$\text{CNR}_{pt}(t; \kappa) = \frac{C_{tr}C_{pt}}{N_o} \frac{2\sqrt{\pi}\kappa T_{dw}}{\kappa^2 + 1} \exp \left[-\frac{(vt - x_o)^2}{\Delta x_{pt}^2} \right] \quad (4.18)$$

$$\Delta x_{pt}^2 = \frac{a_x^2}{4} \frac{\kappa^2 + 1}{\kappa^2 + \left(\frac{\kappa a_x^2}{2L}\right)^2} \quad (4.19)$$

Now we are ready to examine the effects of varying the integration duration on the CNR resolution. In Figure 4-3, we see that the resolution is a function of the integration time and the

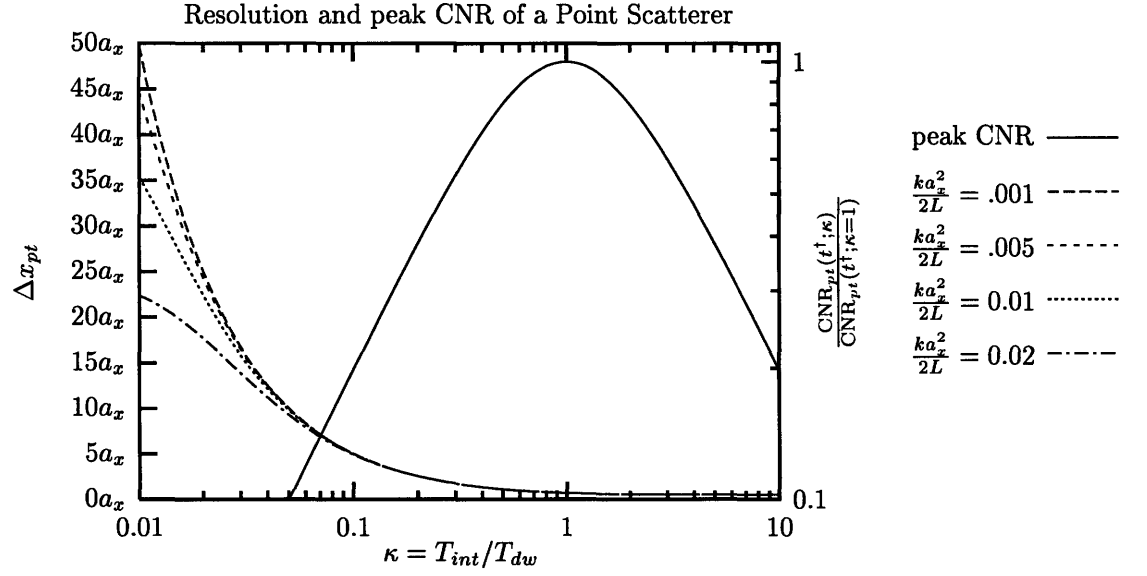


Figure 4-3: Resolution and peak CNR of a point scatterer as a function of integration duration

transmitter's along-track Fresnel number $\left(\frac{\kappa a_x^2}{2L}\right)$. The latter indicates how far the target is from the radar; $\left(\frac{\kappa a_x^2}{2L}\right) \ll 1$ is required for our far-field assumption. The asymptotic (unprocessed) resolution with a small synthetic aperture approaches the footprint size on the terrain. Even then, we achieve marked improvement with only 0.1 of the full-dwell synthetic aperture.

If we use an integration duration longer than the dwell time, we obtain a slightly finer resolution, but at the cost of degradation in CNR. For optimal estimation of the location of the point target, we would like to use the full target return duration ($\Delta t_{pt} = T_{dw}$) as the integration duration such that the highest CNR is achieved. This makes good sense. If the integration time is shorter than Δt_{pt} , then we are not using all the available target return energy for the chirp-compression. On the other hand, if the integration time is longer than Δt_{pt} , then we are letting unnecessary noise enter our processed signal through the extra chirp bandwidth in the filter. This brings up the radar issue of resolution versus accuracy [1]. We can obtain a higher resolution for our estimate with a longer integration time, because resolution is a system performance limit calculated in the absence of noise (i.e., width of $\langle |I_y(t)|^2 \rangle$.) However, a long-integration estimate might not be close to the true

value of the estimated parameter (i.e. accurate) because, at a low CNR, $|I_y(t)|^2$ can be overwhelmed by the high level of noise and the peak of the former may be misplaced (Figure 4-4.)

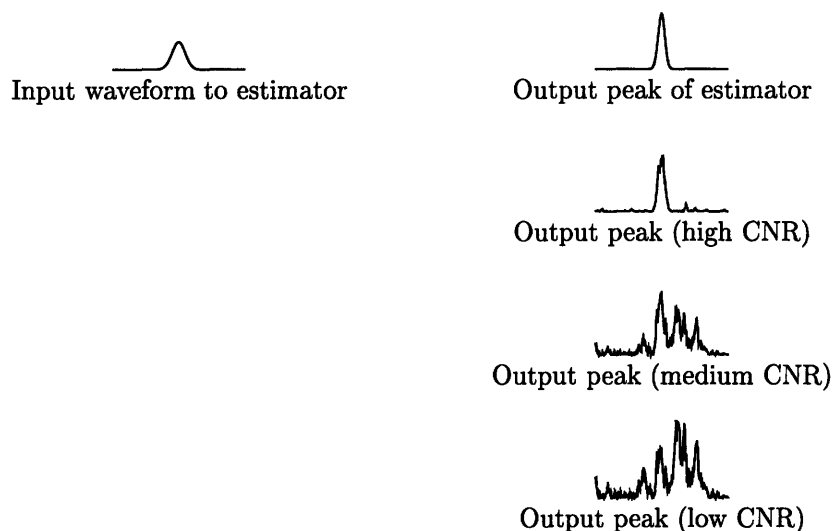


Figure 4-4: Receiver output for estimating target's location: high noise level (low CNR) shifts peak of receiver output from where the true value lies

In all situations with a specular target return and additive white Gaussian noise, the best CNR is achieved if we match the integration time with the duration of the target return, because this is a result of the matched filter that classical detection and estimation theory establishes.

To summarize this section, we note that multi-resolution processing of the radar return offers a way to vary the CNR behavior (4.17) of our processed signal according to the length of the integration time used. Although there is probably only one best CNR achieved by the matched integration time (e.g. with the target return duration), we shall show in the next section that how this CNR changes, i.e. how $x^\dagger(\kappa)$, $x_{res}(\kappa)$ change, with respect to the integration time, is target dependent. This is a strong parallel to the work of Irving et al. [15], which shows that a similar multi-resolution imaging scheme, essentially one that uses a discrete collection of κ to image the return, leads to a useful discriminant of clutter and man-made targets.

4.3 Target Multi-resolution Signatures

In this section, we shall assume returns from some of the targets presented in Chapter 3, and show that their multi-resolution CNR behaviors are different. This is evidence that various targets, having different multi-resolution signatures, can be discriminated from each other. We will first present a general result about the SAR resolution which we will use later on to carry out the calculations for different targets.

4.3.1 A General Resolution Calculation

We need to look at the width of the Gaussian in $|\mathbf{l}_y(t)|^2$ or the CNR to figure out the resolution of a target. Ultimately, we must convolve $\mathbf{y}(t)$ with $\mathbf{h}_{mr}(t; \kappa)$. However, because convolution is associative (for smooth waveforms), we can use (2.32, 2.8, 2.5, and 2.26) to carry out the time integration first, and defer the spatial integral over the target reference plane. For a multiplicative target model, we find that

$$\mathbf{l}_y(t) = \sqrt{C_{tr}\kappa T_{dw}} \sqrt{\frac{2\pi}{\kappa^2 + 1}} \int d\bar{\rho} \mathbf{T}(\bar{\rho}) \exp \left[j \frac{ky^2}{L} - \frac{k^2 a_y^2}{2L^2} y^2 - \mathbf{P}(vt - x)^2 \right] \quad (4.20)$$

$$\mathbf{P} = \frac{2}{a_x^2} \left[\left(\frac{\kappa^2 + \left(\frac{ka_x^2}{2L}\right)^2}{\kappa^2 + 1} \right) + j \frac{ka_x^2}{2L} \left(\frac{\kappa^2 - 1}{\kappa^2 + 1} \right) \right] \quad (4.21)$$

This has the additional interpretation of passing a spatial function or random process $\mathbf{T}(\bar{\rho})$ (depending on whether the diffuse or the specular target model is used) through a linear system that transforms the spatial information of the target to a time signal.

We can arrive at a similar result for a general linear impulse response target model by using (2.31) instead of (2.32). With the aid of a transform from x, x_1 to the sum-and-difference coordinates, $\frac{1}{2}(x + x_1), x - x_1$, we are able to re-use the same time-integration for obtaining (4.20) and write

$$\begin{aligned} \mathbf{l}_y(t) = & \sqrt{C_{tr}\kappa T_{dw}} \sqrt{\frac{2\pi}{\kappa^2 + 1}} \int d\bar{\rho} \int d\bar{\rho}_1 \mathbf{T}(\bar{\rho}, \bar{\rho}_1) \\ & \exp \left[\left(j \frac{k}{2L} - \frac{k^2 a_y^2}{4L^2} \right) (y^2 + y_1^2) + \left(j \frac{k}{2L} - \frac{k^2 a_x^2}{4L^2} \right) \frac{(x - x_1)^2}{2} - \mathbf{P} \left(vt - \frac{x + x_1}{2} \right)^2 \right] \end{aligned} \quad (4.22)$$

which is in an extremely convenient form for our trihedral.

For our diffuse model, we can use (2.37) to further write

$$\langle |\mathbf{l}_y(t)|^2 \rangle = C_{tr}\kappa^2 T_{dw}^2 \frac{2\pi}{\kappa^2 + 1} \int d\bar{\rho} \lambda^2 \mathcal{T}_d(\bar{\rho}) \exp \left[- \left(\frac{ka_y}{L} \right)^2 y^2 - 2\Re\{\mathbf{P}\}(vt - x)^2 \right] \quad (4.23)$$

4.3.2 MR Signature Comparison: Variations across Targets

We shall now use the above equations to calculate the multi-resolution (MR) CNR behavior of our targets. In this subsection, we will only present the general formulae for the shift and resolution for each target. We will defer the more detailed comments about the individual targets to the next subsection.

Diffuse Target

$$x_{dt}^\dagger = 0 \quad (4.24)$$

$$\frac{2\Delta x_{dt}^2(\kappa)}{\rho_x^2} = 1 + \frac{1}{\Re\{\mathbf{P}\}\rho_x^2} \quad (4.25)$$

$$(4.26)$$

Specular Mirror

$$\frac{x_{sm}^\dagger(\kappa)}{\rho_x} = -\frac{k\phi_x\rho_x \left(\Im\{\mathbf{P}\}\rho_x^2 + \Re\{\mathbf{P}\}\rho_x^2 \frac{k\rho_x^2}{R_x} \right)}{|\mathbf{P}|^2\rho_x^4 + \Re\{\mathbf{P}\}\rho_x^2 \left(1 + \left(\frac{k\rho_x^2}{R_x} \right)^2 \right)} \quad (4.27)$$

$$\frac{2\Delta x_{sm}^2(\kappa)}{\rho_x^2} = \frac{|\mathbf{P}|^2\rho_x^4 + 1 + \left(\frac{k\rho_x^2}{R_x} \right)^2 + 2\Re\{\mathbf{P}\}\rho_x^2}{|\mathbf{P}|^2\rho_x^4 + \Re\{\mathbf{P}\}\rho_x^2 \left(1 + \left(\frac{k\rho_x^2}{R_x} \right)^2 \right)} \quad (4.28)$$

Right-angled Trihedral

$$x_{3h}^\dagger = 0 \quad (4.29)$$

$$\frac{2\Delta x_{3h}^2(\kappa)}{\rho_x^2} = \frac{1}{\Re\{\mathbf{P}\}\rho_x^2} \quad (4.30)$$

Right-angled Dihedral

$$x_{2h}^\dagger = 0 \quad (4.31)$$

$$\frac{2\Delta x_{2h}^2(\kappa)}{\rho_x^2} = \left(\sin^2 \theta + \frac{1 + \Re\{\mathbf{P}\}\rho_x^2 \sin^2 \theta}{|\mathbf{P}|^2\rho_x^4 \sin^2 \theta + \Re\{\mathbf{P}\}\rho_x^2} \right) \quad (4.32)$$

In Figure 4-5, we have plotted the MR signatures of our four finite-size targets: diffuse, specular mirror, trihedral, and dihedral, for some nominal combinations of Fresnel numbers $\frac{ka_x^2}{2L}$ and target sizes ρ_x . We see that, even when the targets have the same dimension ρ_x , processing the radar return signals with different integration times leads to different resolutions for different targets. As a result, target discrimination based on the SAR images of different resolutions is possible.

Note that in all cases, as the integration time, or κ , approaches zero, our filter $\mathbf{h}_{mr}(t; \kappa)$ approaches an impulse and $\mathbf{l}_y(t)$, essentially unprocessed, approaches $\mathbf{y}(t)$. i.e., the resolution would be the diffraction-limited target return duration. As we can infer from our analysis in Chapter 2, in a low κ regime, the diffuse target and the trihedral have the same duration or resolution, in fact, the broadest among all targets. For the diffuse target, this is because it is an isotropic scatterer; for

the trihedral, while it does not scatter isotropically, has a broad backscattering pattern – one that is independent of the direction of illumination. In the same low- κ regime, the specular mirror, being the one that preserves the most directionality of the impinging beam among all targets, will yield the narrowest target return width. The dihedral’s behavior, depending on its orientation (which is $\theta = \pi/4$ for this example) lies between that of the specular mirror and the trihedral.

As κ increases and before it approaches 1 (full dwell), the resolutions of these targets undergo significant changes. The specular mirror’s resolution merges with that of the diffuse target: they both exhibit the same target-limited resolution, whereas the trihedral’s resolution is only limited by the size of the radar’s aperture, and is exactly that of a point target. i.e. The dwell time limits the chirp bandwidth in the trihedral return and thus the resolution, which is on the order of the radar’s aperture size (Table 4.3.2). The dihedral, again, lies in between the specular mirror and the trihedral.

The following table is a summary of the target’s MR signatures.

	$(v\Delta t)^2$	$\Delta x^2(\kappa = 1)$
Diffuse Target	$\left(\frac{L}{ka_x}\right)^2$	$\frac{1}{2}(\rho_x^2 + a_x^2)$
Specular Mirror	$\frac{L^2}{k^2(2\tilde{\rho}_x^2 + a_x^2)}$	$\frac{1}{2}\left[\tilde{\rho}_x^2\left(\frac{\rho_x^2 + a_x^2}{\tilde{\rho}_x^2 + a_x^2}\right) + a_x^2\right]$
Point Target	$\left(\frac{L}{ka_x}\right)^2$	$\frac{a_x^2}{2}$
Trihedral	$\left(\frac{L}{ka_x}\right)^2$	$\frac{a_x^2}{2}$
Dihedral	$\frac{L^2}{k^2(\rho_x^2 \sin^2 \theta + a_x^2)}$	$\frac{1}{2}(\rho_x^2 \sin^2 \theta + a_x^2)$

Table 4.1: Target MR signature: resolution for $\kappa = 1$ (full dwell time), compared with original target return duration

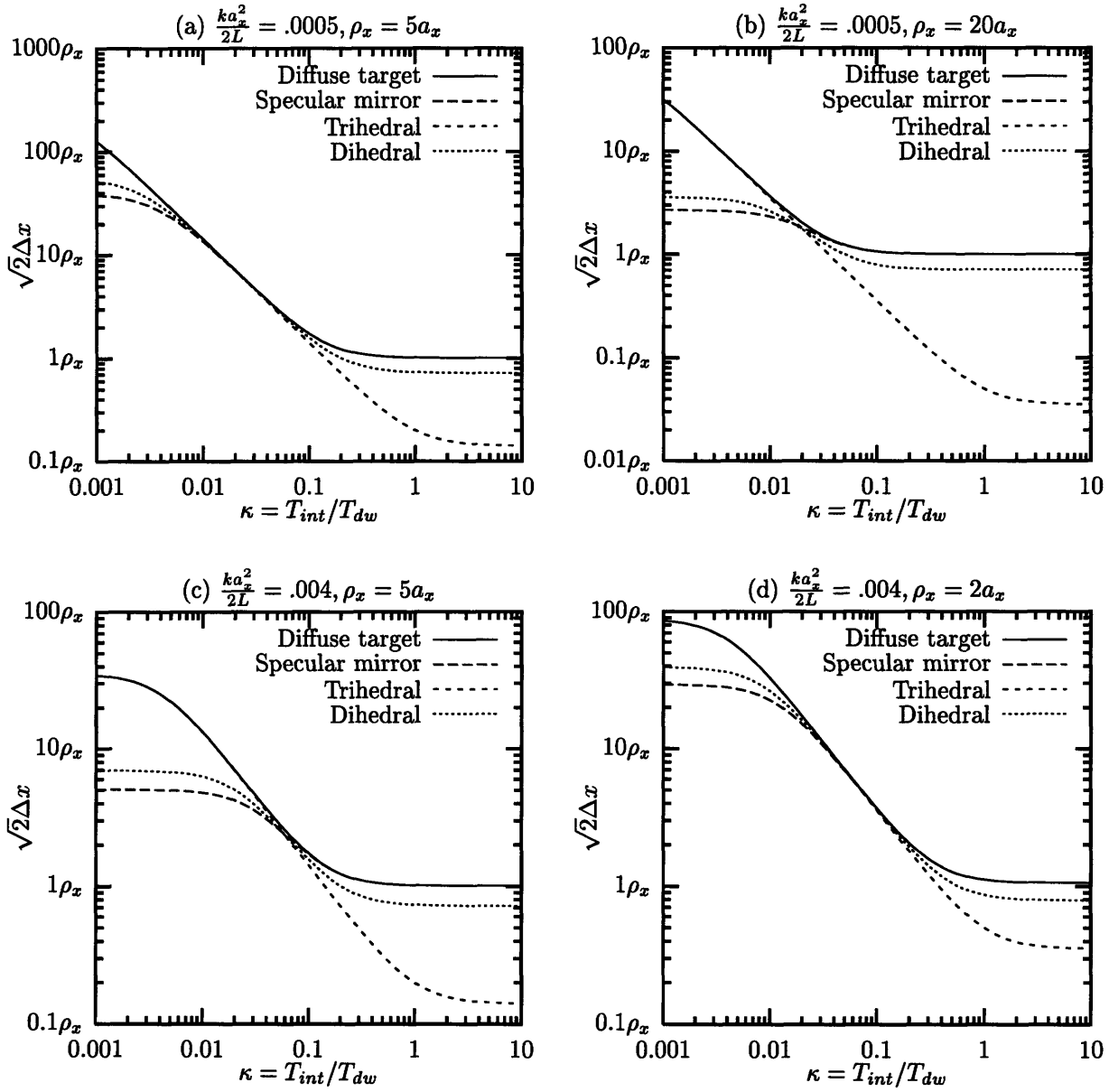


Figure 4-5: MR signatures for four target models: diffuse target, specular mirror ($R_x \rightarrow \pm\infty$), trihedral, and dihedral ($\theta = \pi/4$)

4.3.3 MR Signature Comparison: Variations due to Target Geometry

In this subsection, we will examine the MR signatures of each type of target individually. We would like to show that, within each type of target, the MR signatures are affected by different geometries of the target. This may be used as another MR target characteristic to help discrimination, as well as to possibly estimate the target's geometric parameters.

Diffuse Target

The MR resolution of a diffuse target is a monotonically decreasing function of the integration time. In the low- κ region, the diffuse target resolution is dwell-limited, as shown in Figure 4-6, and is independent of the target size. Only the trihedral or the point target (which is only an idealization) would have such a full dwell back-scattering duration. When processed with the full dwell, the diffuse target resolution is target-limited, which is different from how a trihedral or a point scatterer would give aperture-limited (or chirp-limited) resolution in that regime. In fact, the larger the diffuse target, the bigger this difference in resolution is at the full-resolution image.

In practice, one would not use $\mathbf{h}_{mr}(t, \kappa = 0)$ because of broadband noise. However, because of this distinction at these two limits, it is possible to tell this diffuse target apart from an untilted, uncurved specular mirror by using the MR processor at $\kappa \ll 1$ and $\kappa = 1$. Provided that we have techniques to contend with speckle fading [6] that degrades the SAR image, it is possible to estimate the diffuse target size based on the full-dwell SAR image.

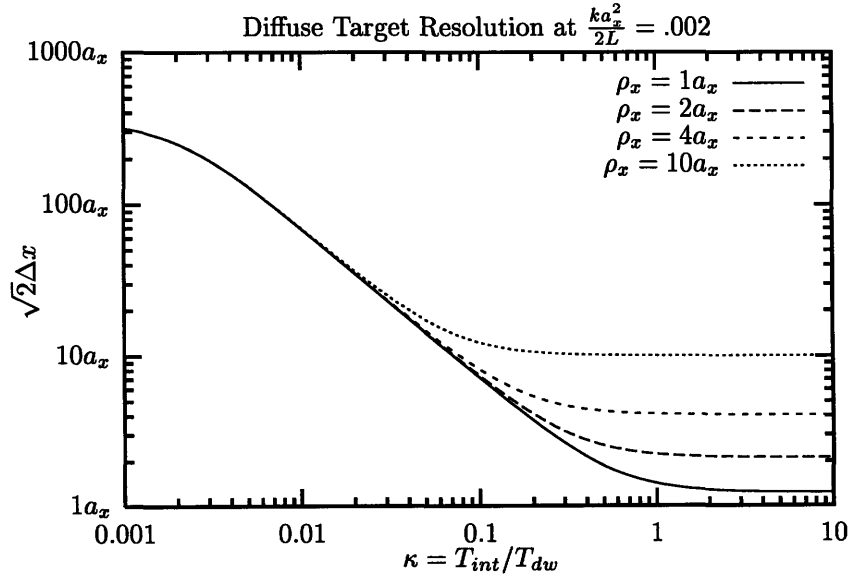


Figure 4-6: MR signatures of diffuse targets with different dimensions

Specular Mirror

The diffraction-limited resolution of the specular mirror's unprocessed return ($\kappa = 0$) is finer than that of the diffuse target because of the coherent behavior of the specular mirror. However, at $\kappa = 1$, it has the same target-limited resolution (Figure 4-7 (c)). Again, we could possibly estimate the size of the specular mirror based on the full-resolution image.

Note that the resolution of our specular mirror does not depend on the tilt. This is apparent from the fact that the target return duration of our specular mirror Δt_i (3.31) is independent of the tilt.

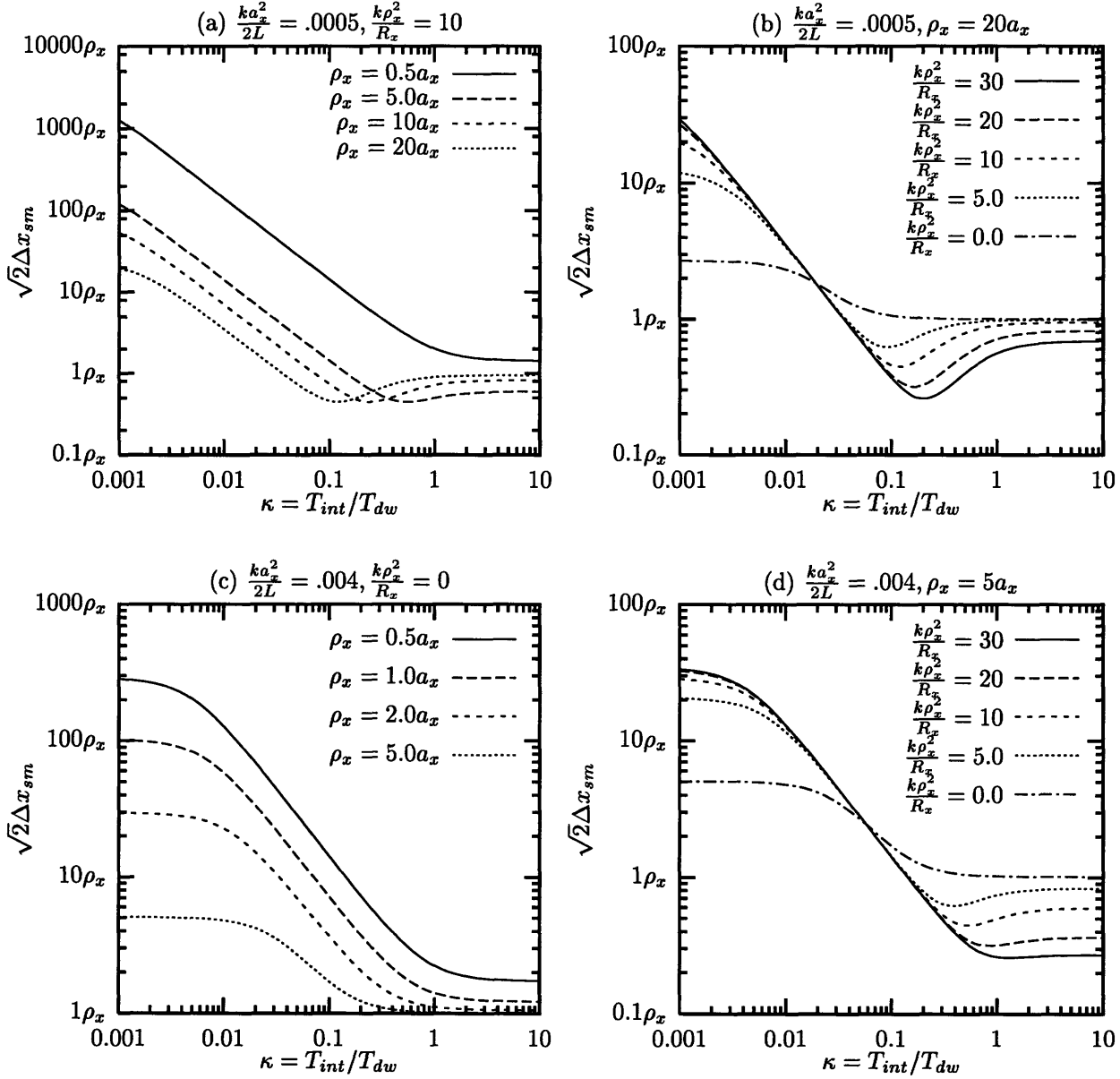


Figure 4-7: MR signatures: resolution of specular mirrors with different dimensions and curvatures

Now let us examine the effect of curvature on the MR signatures of the specular mirror. Under

all circumstances (Figure 4-7 (b) and (d)), the curvature of a mirror seems to affect the effective target size only (3.20). At a low κ , the higher the curvature, the smaller the effective target size, the less directional the reflected beam is after interaction with the specular mirror. This results in a broad target return width is (wider than the diffraction-limited resolution for a large mirror.) At a high κ , the fact that the curvature reduces the effective target size actually helps the resolution. (This effect does not depend on the sign of the curvature (4.28).)

In addition, the best resolution of a curved mirror clearly is achieved at some $\kappa < 1$. This minimum resolution appears to be an increasing function of the curvature, (Figure 4-7 (b)), but a decreasing function of the target size (Figure 4-7 (a)) (which is probably due to the fact that with $\frac{k\rho_x^2}{R_x}$ held constant, increasing ρ_x actually *decreases* the radius of curvature R_x .) Why the MR signatures show this curvature dependent effect is not quite understood at the writing of this thesis, but we may be able to exploit this effect to detect curved specular mirrors.

Note that the best CNR is probably not achieved at $\kappa = 1$ due to the mismatch of the target duration Δt and the dwell time.

The shift in the peak CNR also shows MR dependence. In particular, the aspect-dependence, or the broad-side flash phenomenon [4] is present at low κ but vanishes at high κ (Figure 4-8, Table 4.2). This can be explained from the fact that at high κ , our SAR becomes very focused due to the large synthetic aperture, and the effective antenna beam pattern becomes sharply pointed right below the down-looking radar. The broad-side flash received at the normal incidence of the tilted plane mirror assumes an off-down-looking direction from the radar's perspective and therefore will not show up.

	vt_i	$x^\dagger(\kappa = 1)$
Specular Mirror	$\phi_x L \frac{2\tilde{\rho}_x^2}{2\tilde{\rho}_x^2 + a_x^2} \left(1 - \frac{ka_x^2 k\rho_x^2}{2L R_x} \right)$	$-\phi_x L \frac{\tilde{\rho}_x^2}{\tilde{\rho}_x^2 + a_x^2} \frac{ka_x^2 k\rho_x^2}{L R_x}$

Table 4.2: Specular mirror MR signature: offset for $\kappa = 1$ (full dwell time), compared with original target return offset

Both the tilt and the curvature dependent MR behavior of the specular mirror may very favorably help us detect its presence.

Trihedral

The resolution of a trihedral is completely independent of the target size in all regions of κ . But our trihedral model is very idealized and does not include cut-off effects at the boundaries, or tilt, or the possible translation of the incident beam.

Dihedral

A dihedral is really not any different from a specular mirror with no tilt and no curvature because its behavior can be summarized by obtaining the effective target size $\bar{\rho}_T = \rho_T \sin \theta$ according to the target's orientation (3.61), and substituting this value for the dimension of a specular mirror. The interesting behavior of the dihedral probably lies in a 2-D SAR radar system when the across-track effects become crucial as well. In addition, a dihedral has different polarization properties due to its double-bounce scattering nature that will not appear in our scalar wave analysis.

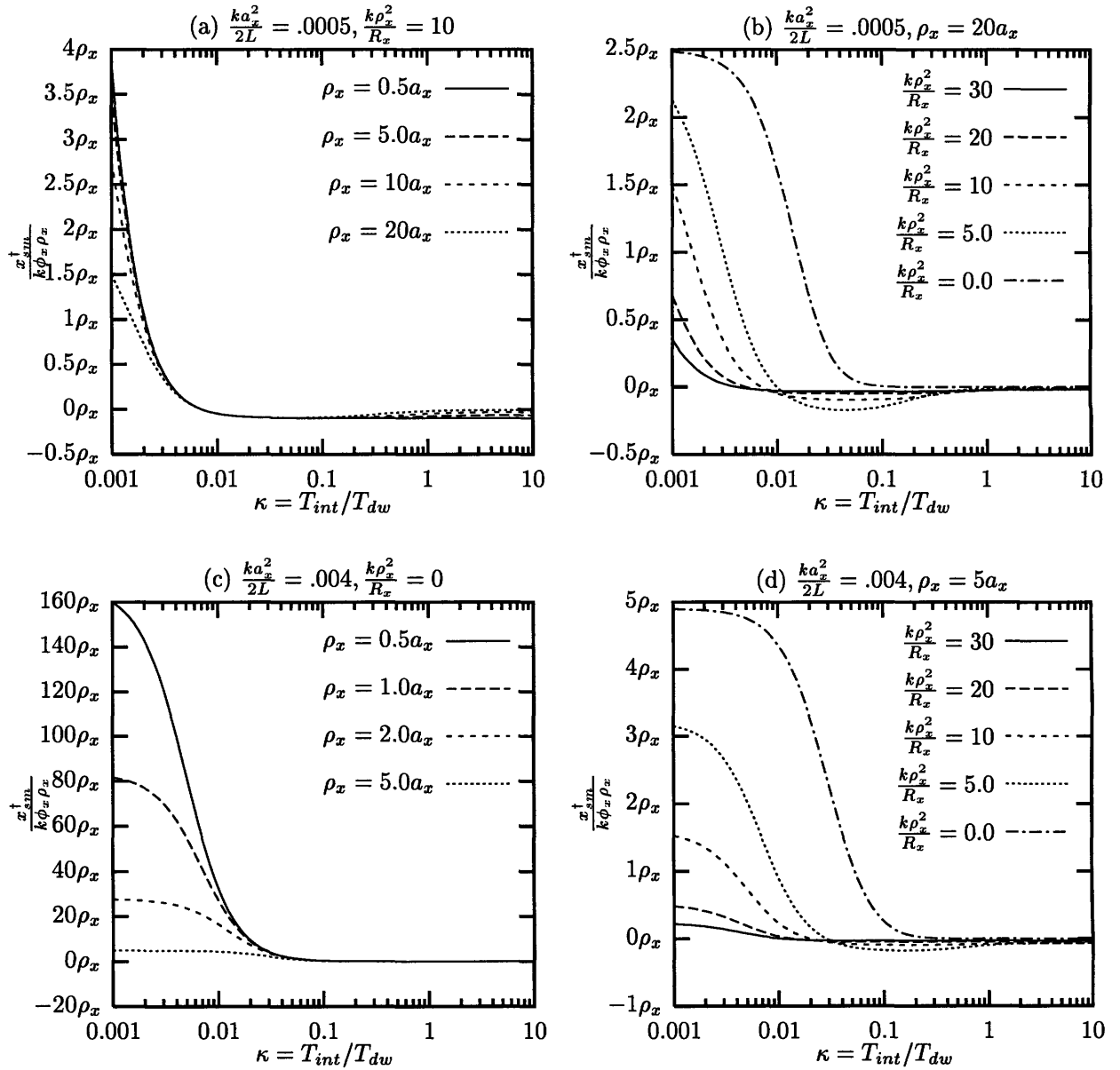


Figure 4-8: MR signatures: shift of specular mirrors with different dimensions and curvatures

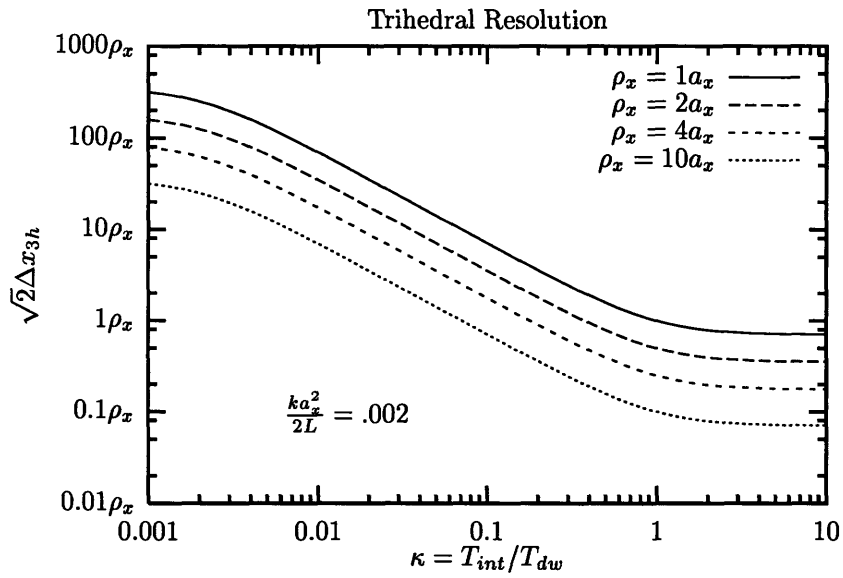


Figure 4-9: MR signature: resolution of trihedrals with different dimensions

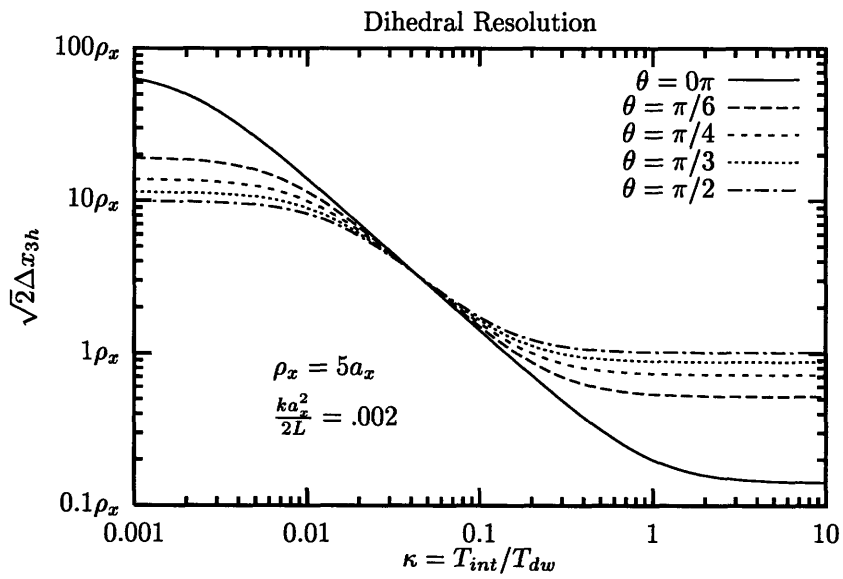


Figure 4-10: MR signature: resolution of dihedrals with different angles of orientation

4.3.4 Summary

In this chapter, we have explored in detail the MR signatures of different targets, which help us realize that various targets can be discriminated merely by processing the return signal with a varying integration time. Most importantly, some of these differences in MR target signatures are lost in conventional SAR images processed with the full dwell time. Certain adaptations to the conventional imaging method are therefore necessary for target discrimination. Several questions remain to be answered.

1. What are the target discrimination problems that we want to pose to address common situations in radar system practice?
2. What are the proper ways to utilize the MR filter in order to achieve the best performance in target discrimination?
3. Would the MR filter be optimal for the above problems? If not, what are the structures of the optimal filters and how well do they perform compared to the MR filter?

An optimal target detection scheme based on the MR resolution signature difference would involve processing the radar return at several resolutions, $\kappa_i, i = 1, 2, \dots, n$ in order to obtain the widths of the resulting output signal for use in later decision rules. In order to utilize this information optimally, we need to have some statistical information about the widths. This presents a difficulty because these widths are only theoretical characterizations based heavily on the assumption of the Gaussian shape of our signals, and not straightforward experimental quantities whose probability densities or statistical moments can be easily obtained independent of the measurement procedure.

If we are to study this MR filter further, we could take the approach of further assuming some experimental definition of the CNR resolution defined theoretically in this chapter, and apply a statistical model for the measurements of these widths in additive white Gaussian noise to obtain the optimal decision rules therefrom. Alternatively, we could train some assumed adaptive or learning signal processing structure to exploit these target-dependent MR signature differences as done in [15], and achieve a certain performance improvement in target discrimination without understanding the system's underlying limitations.

Parameterized by only κ , the MR filter does have the benefit of generality which may help simplify its implementation, but at the same time it may be sub-optimal. Therefore, neither approach seems as satisfactory as posing some practical yet tractable detection problems, and solving for their optimal detectors without constraining ourselves to using the MR filter. We shall proceed in this direction in the next chapter.

Chapter 5

Target Detection Problems

In the following sections, we shall pose different hypothesis testing problems that address some common situations in practice. In all of the cases, we assume that the geometric parameters and the location of our targets are known. Although not entirely realistic, this will allow us to assess how much improvement an optimal method of target-return processing, probably one different from both the conventional and the MR filters, can be obtained under idealized circumstances. That is, we will present the optimal receiver structures for these detection problems and compare their performance against those of the conventional and the MR filter and hence gain intuition into what needs to be improved in the latter. The performance of the optimal processors should serve as the theoretical limits (under the assumption of the validity of our target models) of how well any other receivers can perform in either an idealized or generalized setting.

5.1 Detection of a Specular Mirror in Uniform Clutter

The first problem we will address is the one that motivates this thesis. We have a vast extent of natural clutter (probably grass) in which a specular man-made target could possibly be embedded.

5.1.1 Idealized Binary Hypothesis Test

We will model the grass with our uniform diffuse clutter model, and we will pick our coordinate system such that the possible man-made target, modeled by our specular mirror, is located at the origin of the target terrain. The uniform diffuse background clutter is present under both hypothesis H_0 and hypothesis H_1 . In our null hypothesis H_0 , the specular mirror is absent, and in hypothesis H_1 , the specular mirror is present.

$$\begin{aligned}
H_0 : \quad \mathbf{T}(\bar{\rho}) &= \mathbf{T}_{uc}(\bar{\rho}) \\
H_1 : \quad \mathbf{T}(\bar{\rho}) &= \mathbf{T}_{sm}(\bar{\rho}) + \mathbf{T}_{uc}(\bar{\rho})
\end{aligned} \tag{5.1}$$

where both $\mathbf{T}_{uc}(\bar{\rho})$ and $\mathbf{T}_{sm}(\bar{\rho})$ are defined in Chapter 3. In reality, there probably should be a hole in the uniform clutter where our man-made target is located. But since a large area, at the size of the radar footprint, of the uniform clutter is being imaged, this hole of the size of a man-made target in the far field probably would not make much difference to the uniform clutter's contribution to the radar return at any point in time, and therefore the optimal decision system is rather unaffected by this simplification in modeling.

Without going through the same calculations from the previous chapters, we will work directly with the radar return $\mathbf{r}(t)$ contributed from the possible target and clutter under each of the hypotheses. In addition, we will have receiver noise with the same statistics under both hypotheses.

$$\begin{aligned}
H_0 : \quad \mathbf{r}(t) &= \mathbf{y}_{uc}(t) + \mathbf{w}(t) \\
H_1 : \quad \mathbf{r}(t) &= \mathbf{y}_{sm}(t) + \mathbf{y}_{uc}(t) + \mathbf{w}(t)
\end{aligned} \tag{5.2}$$

where

$\mathbf{y}_{uc}(t)$ = return from uniform diffuse clutter

$\mathbf{y}_{sm}(t)$ = return from specular mirror located at origin

$\mathbf{w}(t)$ = receiver noise

$\mathbf{y}_{sm}(t)$ is precisely (3.30) and is a deterministic signal except for its random absolute phase. $\mathbf{w}(t)$ and $\mathbf{y}_{uc}(t)$ are statistically independent, zero-mean circulo-complex Gaussian noise sources and have the following power density spectra:

$$S_{\mathbf{w}}(f) = N_o \tag{5.3}$$

$$S_{\mathbf{y}_{uc}}(f) = C_{tr}C_{uc} \sqrt{\frac{\pi a_x^2}{v^2}} \exp \left[-\frac{a_x^2}{v^2} (\pi f)^2 \right] \tag{5.4}$$

where $f = \nu - \nu_{IF}$ is frequency in Hz centered at the IF frequency ν_{IF} . The uniform clutter acts as a colored noise, and has a bandwidth proportional to $\frac{v}{a_x}$. This is a simple binary detection problem: there is a random-phased known signal under one hypothesis and identical colored noise under both hypotheses.

5.1.2 Optimal Processor

We would like to process our return $\mathbf{r}(t)$ in such a way that the probability of detection $P_D = Pr\{\text{say } H_1 \text{ given } H_1 \text{ true}\}$ is maximized subject to the constraint that the probability of false alarm $P_F = Pr\{\text{say } H_1 \text{ given } H_0 \text{ true}\}$ does not exceed a specified level. This is the Neyman-Pearson criterion for a binary hypothesis testing problem, whose optimal decision rule is known to be a likelihood ratio test (LRT) [28]. To implement the LRT for detecting our specular mirror return (deterministic) from the combined colored noise, we need a whitening filter $\mathbf{H}_w(f)$ whose output will be matched-filtered with the pre-whitened expected return $\mathbf{y}_{sm}(t) * \mathbf{h}_w(t)$ [28], where $\mathbf{h}_w(t)$ is the impulse response of $\mathbf{H}_w(f)$ (Figure 5-1.) The whitening filter has to satisfy¹

$$|\mathbf{H}_w(f)|^2 = \frac{1}{S_w(f) + S_{y_{uc}}(f)} \quad (5.6)$$

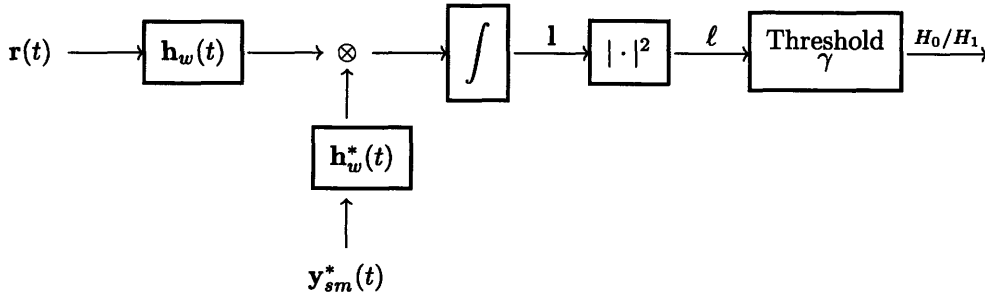


Figure 5-1: Optimal processor as a whitened-correlator system

The resulting LRT is

$$|l|^2 = \ell \sum_{\text{say } H_0}^{\text{say } H_1} \gamma \quad (5.7)$$

where the threshold is chosen to achieve the desired false-alarm probability. We can also cast this optimal processor into a form that is used in the IF filtering model [28]: where the first two blocks constitute our IF filter $\mathbf{H}(f)$ (centered at the frequency ν_{IF}) in our IF model.

¹A possible filter is

$$\mathbf{H}_w(f) = \frac{1}{\sqrt{N_o + j\sqrt{C_{tr}C_{sm}}} \sqrt{\frac{\pi a_x^2}{v^2} \exp\left[-\frac{a_x^2}{2v^2}(\pi f)^2\right]}} \quad (5.5)$$

but this is not unique or causal. The idea of causality should not concern us now because off-line processing is assumed.

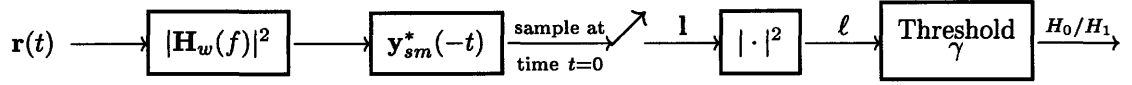


Figure 5-2: Optimal processor as a filter-sample system

The probability of false alarm of such a receiver is

$$P_F = \exp \left[-\frac{\gamma}{\text{var}(1 | H_0 \text{ or } H_1)} \right]. \quad (5.8)$$

The probability of detection is completely characterized by the effective signal-to-noise ratio d_{opt}^2 ,

$$P_D = Q \left(\sqrt{2}d_{opt}, \sqrt{\frac{2\gamma}{\text{var}(1 | H_0 \text{ or } H_1)}} \right) \quad (5.9)$$

$$= Q(\sqrt{2}d_{opt}, \sqrt{-2 \ln P_F}) \quad (5.10)$$

where $Q(a, b)$ is Marcum's Q -function [13]

$$Q(a, b) = \int_b^\infty z \exp \left(-\frac{z^2 + a^2}{2} \right) I_0(az) dz \quad (5.11)$$

and $I_0(x)$ is the modified Bessel function of the first kind.

$$I_0(x) = \int_{-\pi}^{\pi} \exp[x \cos \theta] \frac{d\theta}{2\pi}. \quad (5.12)$$

The effective signal-to-noise ratio for this optimal processor is

$$d_{opt}^2 \equiv \frac{|\langle 1 | H_1 \rangle - \langle 1 | H_0 \rangle|^2}{\text{var}(1 | H_0 \text{ or } H_1)} \quad (5.13)$$

$$= \frac{\left[\int |\mathbf{Y}_{sm}(f)|^2 |\mathbf{H}_w(f)|^2 df \right]^2}{\int [S_w(f) + S_{y_{uc}}(f)] |\mathbf{H}_w(f)|^4 |\mathbf{Y}_{sm}(f)|^2 df} \quad (5.14)$$

$$= \int \frac{|\mathbf{Y}_{sm}(f)|^2}{N_o + S_{y_{uc}}(f)} df \quad (5.15)$$

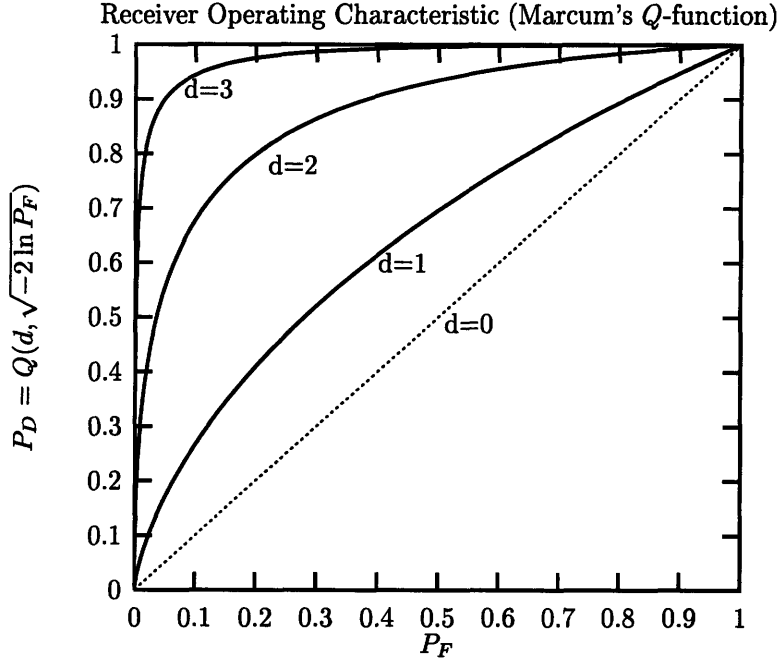


Figure 5-3: The Receiver Operating Characteristics (ROC) of a filter-sample system for detecting a deterministic signal with random phase from Gaussian signal noise. The detection probability is always Marcum's Q -function parameterized by the effective signal-to-noise ratio d^2 (which depends on the filter used), and the probability of false alarm P_F .

Normalizing the frequency f in Hz to a dimensionless quantity f' , we get

$$d_{opt}^2 = \text{SNR}_{sm} \frac{1}{\sqrt{\pi}} \int \frac{\exp \left[- \left(f' + k\phi_x \frac{2\tilde{\rho}_x^2}{\sqrt{2\tilde{\rho}_x^2 + a_x^2}} \right)^2 \right]}{1 + \text{DNR} \exp \left[- \frac{a_x^2}{2\tilde{\rho}_x^2 + a_x^2} f'^2 \right]} df' \quad (5.16)$$

where

SNR_{sm} = Specular mirror signal-to-receiver-noise ratio

$$\equiv \frac{1}{N_o} \int |\mathbf{Y}_{sm}(f)|^2 df = \frac{1}{N_o} \int |\mathbf{y}_{sm}(t)|^2 dt = \frac{C_{tr}}{N_o} C_{sm} \sqrt{\pi} \Delta t_{sm} \quad (5.17)$$

$$= \frac{P_{tr}}{N_o} \frac{k^3 a_x^2 a_y^2}{4L^3} \frac{1}{v \sqrt{2\tilde{\rho}_x^2 + a_x^2}} \sqrt{\pi} \mathcal{T}_{sm} \rho_x \tilde{\rho}_x \rho_y \tilde{\rho}_y \exp \left[- \frac{2(k\phi_x \tilde{\rho}_x a_x)^2}{2\tilde{\rho}_x^2 + a_x^2} - 2(k\phi_y \tilde{\rho}_y)^2 \right]. \quad (5.18)$$

DNR = Diffuse background (uniform clutter) to receiver noise ratio

$$\equiv \frac{S_{y_{uc}}(f=0)}{N_o} = \frac{C_{tr} C_{uc}}{N_o} \sqrt{\frac{\pi a_x^2}{v^2}} \quad (5.19)$$

$$= \frac{P_{tr}}{N_o} \frac{a_x^2 a_y}{L^2 v} \pi^{3/2} \mathcal{T}_{uc} \quad (5.20)$$

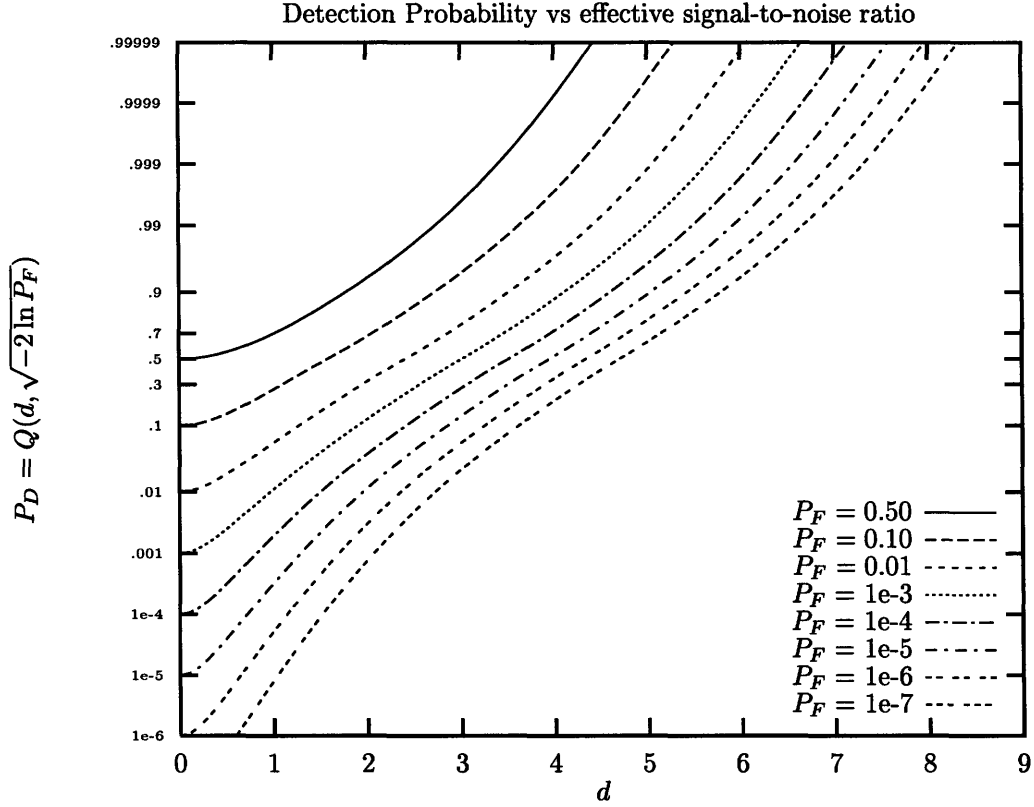


Figure 5-4: Detection probability versus effective signal-to-noise ratio

We see that d_{opt}^2 is proportional to the signal-to-receiver-noise ratio SNR_{sm} (which can be increased by increasing the transmitted power, establishing proper orientation of the target, etc.) and an integral which represents how much the combined receiver and diffuse background noise corrupts the specular signal energy (Figure 5-5). If the hypothesis testing problem is one of detecting the specular mirror return in white receiver noise only *without* the diffuse clutter return ($DNR = 0$), SNR_{sm} would be the performance index d^2 to be used in combination with Marcum's Q -function (5.10) to evaluate P_D given P_F .

Because the integral in (5.16) cannot be evaluated in closed form for an arbitrary value of DNR, we will first present the results of some limiting cases for which we can simplify the d_{opt}^2 expression.

Large Tilt

When the target is very tilted, it acquires a large chirp frequency shift. i.e. the numerator of the integrand in (5.16) is insignificant at all frequencies for which the clutter spectrum differs significantly from zero. At frequencies where the mirror's power spectrum is significant, there is only receiver noise to contend with.

$$d_{opt}^2 \rightarrow SNR_{sm}, \quad \text{when } k|\phi_x|a_x \gg 1 + \frac{a_x^2}{2\tilde{\rho}_x^2} \quad (5.21)$$

Typical Power Spectra of Specular Mirror Return and Uniform Diffuse Clutter Return

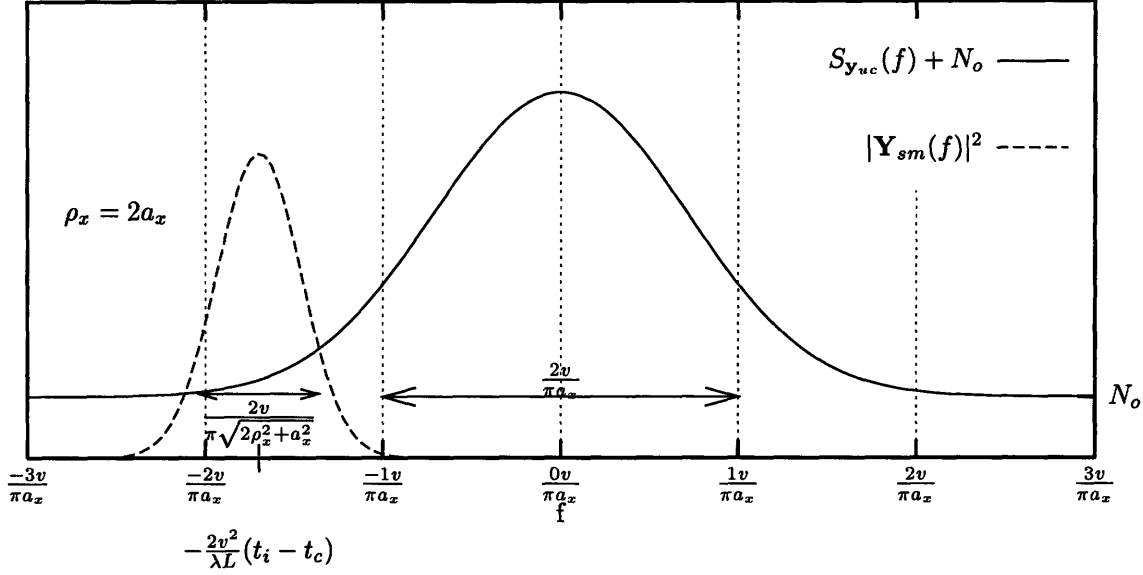


Figure 5-5: Comparison of specular mirror and uniform clutter return in the frequency domain

Note that SNR_{sm} is a decreasing function of the tilt $|\phi_x|$ (5.18).

High Clutter Energy, Small Tilt

The DNR is frequently quite high, perhaps on the order of 100 [14] because the large diffraction footprint of the radar gives a strong return that results from the reflection off the large area of uniform clutter. This means that we can neglect the receiver noise and obtain

$$d_{opt}^2 \rightarrow \frac{\text{SNR}_{sm}}{\text{DNR}} \sqrt{\frac{2\tilde{\rho}_x^2 + a_x^2}{2\tilde{\rho}_x^2}} \exp \left[(k\phi_x a_x)^2 \frac{2\tilde{\rho}_x^2}{2\tilde{\rho}_x^2 + a_x^2} \right], \quad (5.22)$$

when $\text{DNR} \gg 1$ and $k|\phi_x|a_x < 1 + \frac{a_x^2}{2\tilde{\rho}_x^2}$

Interestingly, the advantage we gain from having a tilt in our mirror by deflecting the signal energy from the clutter energy, i.e., the positive exponent above, is exactly the same as the attenuation suffered by the mirror from the tilt $\exp \left[-(k\phi_x a_x)^2 \frac{2\tilde{\rho}_x^2}{2\tilde{\rho}_x^2 + a_x^2} \right]$ (5.16). However, this high clutter energy regime is only valid for a low tilt because the clutter is band-limited and the receiver noise will limit the performance of our optimal processor at a high tilt.

Large Target

When the target is large, the mirror's return will have a much smaller bandwidth than that of the clutter. The mirror's signal essentially only sees the noise at the shifted frequency of the mirror's

return.

$$d_{opt}^2 \rightarrow \frac{\text{SNR}_{sm}}{1 + \text{DNR} \exp[-(k\phi_x a_x)^2]} \quad 2\bar{\rho}_x^2 \gg a_x^2 \quad (5.23)$$

General Case

We would like to see how our target geometric parameters affect our detection performance, i.e. the effective signal-to-noise ratio d_{opt}^2 . From (3.39) and (5.16), the across-track parameters ρ_y, ϕ_y, R_y enter the effective signal-to-noise ratio only through the energy $E_{y,sm}$ (and not the integral in (5.16), which is due to the radar-system dynamics in the along-track direction.) How they influence d_{opt}^2 is obvious. We will investigate how d_{opt}^2 fares against the along-track parameters ρ_x, ϕ_x, R_x . First we write explicitly

$$d_{opt}^2 = d_{opt}^2(\rho_x, \phi_x, R_x) \quad (5.24)$$

$$\text{SNR}_{sm} = \text{SNR}_{sm}(\rho_x, \phi_x, R_x) \quad (5.25)$$

and we compare d_{opt}^2 to a particular signal-to-noise ratio,

$$\text{SNR}_{sm}^{\circ} = \text{SNR}_{sm}(\rho_x = a_x, \phi_x = 0, R_x \rightarrow \pm\infty) \quad (5.26)$$

because SNR_{sm}° is a quantity independent of the target's along-track parameters. From (3.39) and (5.16),

$$\frac{d_{opt}^2(\rho_x, \phi_x, R_x)}{\text{SNR}_{sm}^{\circ}} = \frac{\rho_x}{a_x} \sqrt{\frac{3\bar{\rho}_x^2}{2\bar{\rho}_x^2 + a_x^2}} \frac{1}{\sqrt{\pi}} \exp \left[-(k\phi_x a_x)^2 \frac{2\bar{\rho}_x^2}{2\bar{\rho}_x^2 + a_x^2} \right] \int \frac{\exp \left[- \left(f + k\phi_x \frac{2\bar{\rho}_x^2}{\sqrt{2\bar{\rho}_x^2 + a_x^2}} \right)^2 \right]}{1 + \text{DNR} \exp \left[- \frac{a_x^2}{2\bar{\rho}_x^2 + a_x^2} f^2 \right]} df \quad (5.27)$$

$$= \frac{d_{opt}^2(\bar{\rho}_x, \phi_x, R_x \rightarrow \pm\infty)}{\text{SNR}_{sm}^{\circ}} \sqrt{1 + \left(\frac{k\rho_x^2}{R_x} \right)^2}. \quad (5.28)$$

We will show only the special case results of an uncurved target, $\frac{d_{opt}^2(\bar{\rho}_x, \phi_x, R_x \rightarrow \pm\infty)}{\text{SNR}_{sm}^{\circ}}$, because the general case with a curved target is only a simple extension thereof.

From (5.27), we see that the tilt affects d_{opt}^2 in two competing ways: the exponential coefficient due to the fact that the tilted mirror does not point to the radar's line-of-sight (vertical direction); the integral which describes the benefit of the shift of chirp frequency in the specular mirror return (away from the spectrum of the uniform clutter) due to the displacement of our broadside flash. The former is a decreasing function of the tilt $|\phi_x|$; the latter is an increasing function of the tilt

(Figure 5-5).

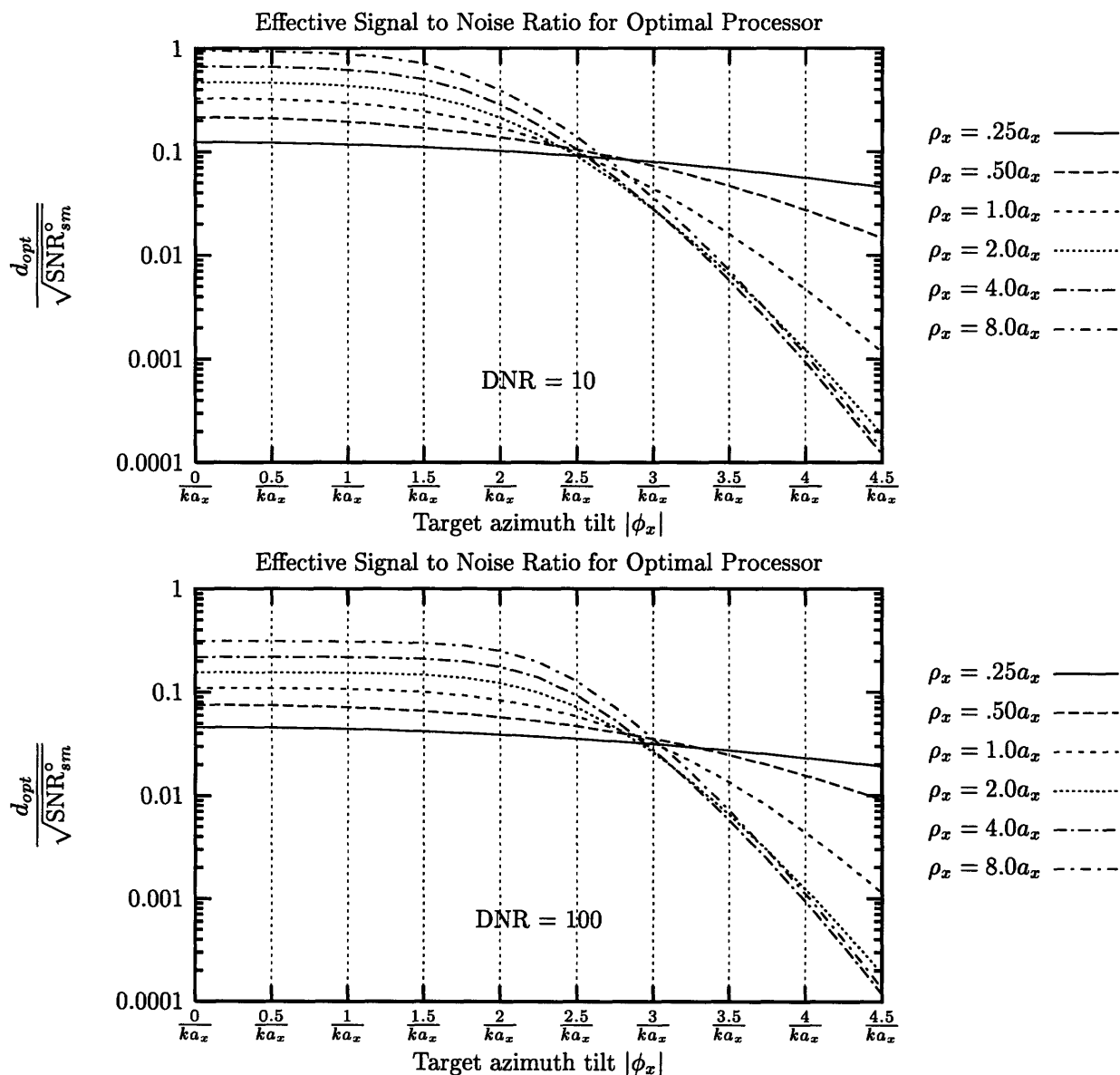


Figure 5-6: Normalized d_{opt} as a function of tilt $|\phi_x|$.

Figure 5-6 shows that these two competing factors roughly annihilate each other at a small tilt angle, and then the advantage of the chirp frequency shift is finally subdued in the receiver-noise limited high-tilt region.

For a small specular mirror (ρ_x small compared to a_x), it will take a high tilt for d_{opt}^2 to attenuate because a small specular mirror's return is less directional (having a wider backscattering pattern) than that of a larger specular mirror, hence mitigating the attenuation due to the mismatch of the radar's look angle and the mirror's normal direction (3.28). The result is that the curves in Figure 5-6 appear flatter for smaller mirrors, and the curves for larger targets roll off faster at high

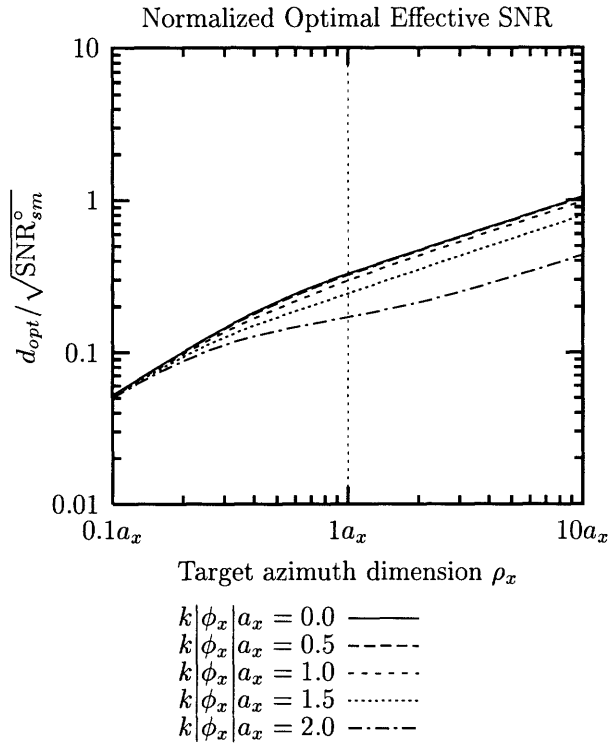
tilts.

The same phenomenon can be seen in Figure 5-7: the vertical spacing between curves is much smaller in the small ρ_x region than that in the large ρ_x region because a large mirror is more effective in giving a directional return.

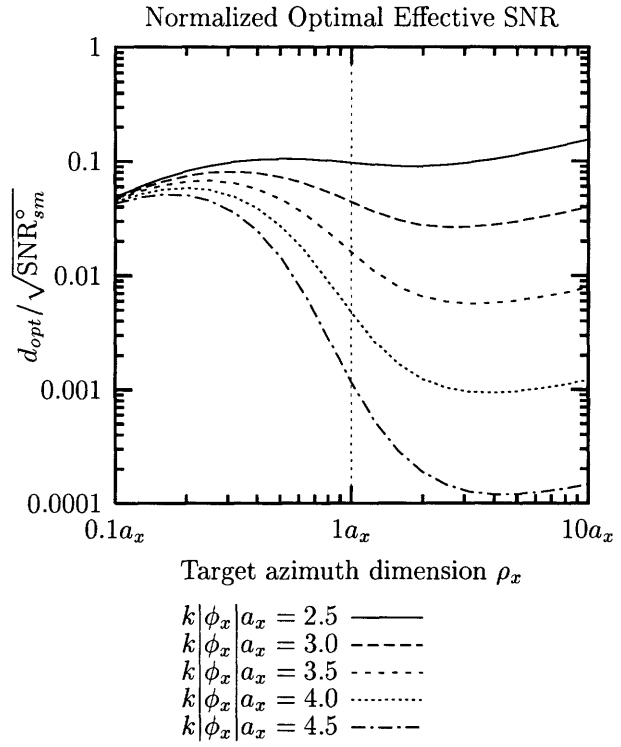
In addition, a large tilt yields a downward-bending curve as the mirror size increases, indicating the disadvantage of tilt as the mirror is large enough to deflect the impinging beam from the down-looking radar by the Snell's law of reflection. We also see that the directionality effect of the specular mirror fully reaches the geometric optics limit at approximately

$$\rho_x \approx 3.0a_x, \frac{2\rho_x^2}{2\rho_x^2 + a_x^2} \approx 0.95 \quad (5.29)$$

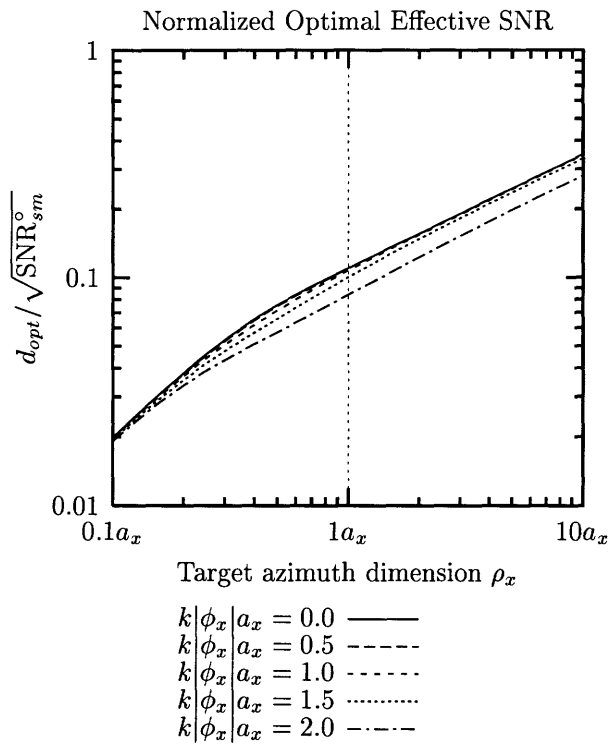
and the reflection does not become much more directional for a larger mirror. Therefore, large mirrors of all tilt levels give parallel curves merely because SNR_{sm} is an increasing function of the mirror's area.



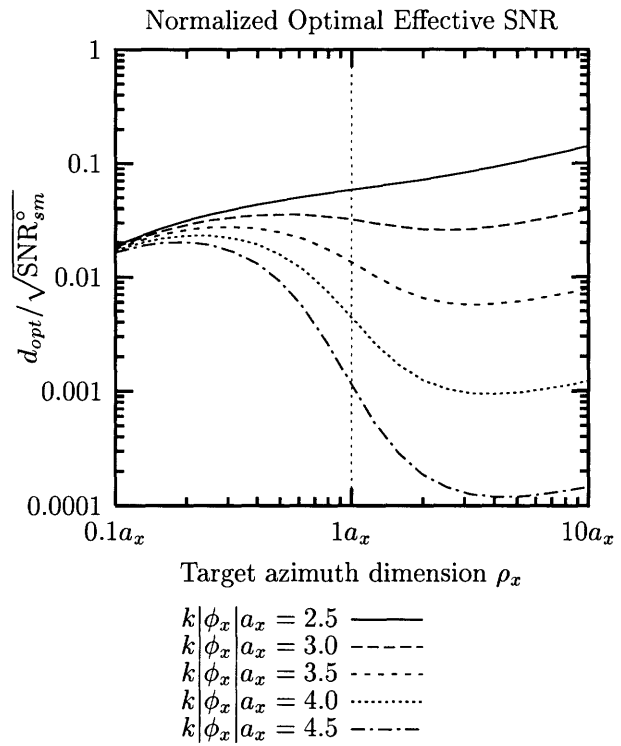
(a) DNR = 10



(b) DNR = 10



(c) DNR = 100



(d) DNR = 100

Figure 5-7: Normalized d_{opt} as a function of target azimuth dimension ρ_x .

5.1.3 Conventional Processor: Full-dwell-time Imager

The conventional imager-receiver introduced in the previous chapter (4.6) has the structure shown in Figure 5.1.3. In order to maximize the probability of detection given any probability of false

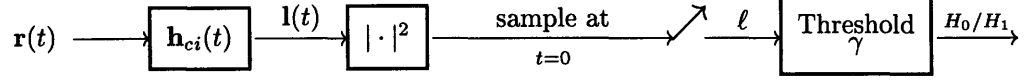


Figure 5-8: Conventional imager-receiver

alarm, we shall sample the output of $\mathbf{h}_{ci}(t)$ at its peak, $\mathbf{l} \equiv \mathbf{l}(t = 0)$, corresponding to where the target would be if it were present. The performance of this receiver in terms of its P_D and P_F is also characterized by (5.8), (5.10) and Marcum's Q -function, but the effective SNR takes on a new value, d_{ci}^2 .

$$d_{ci}^2 \equiv \frac{|\langle \mathbf{l} | H_1 \rangle - \langle \mathbf{l} | H_0 \rangle|^2}{\text{var}(\mathbf{l} | H_0 \text{ or } H_1)} \quad (5.30)$$

$$= \frac{|\langle \mathbf{l} | H_1 \rangle|^2}{\langle \mathbf{l} | H_0 \rangle} \quad (5.31)$$

$$= \frac{\left| \int \mathbf{y}_{sm}(t) \mathbf{h}_{ci}(-t) dt \right|^2}{\int [S_w(f) + S_{y_{uc}}(f)] |\mathbf{H}_{ci}(f)|^2 df} \quad (5.32)$$

$$= \frac{\text{SNR}_{sm}}{1 + \text{DNR} \frac{1}{\sqrt{2}}} \frac{\sqrt{2\bar{\rho}_x^2 + a_x^2}}{a_x} \sqrt{\frac{1 + \left(\frac{k\rho_x^2}{R_x}\right)^2}{\left(\frac{\rho_x^2}{a_x^2} + 1\right)^2 + \left(\frac{k\rho_x^2}{R_x}\right)^2}} \exp \left[-(k\phi_x a_x)^2 \left(\frac{2\bar{\rho}_x^2}{\bar{\rho}_x^2 + a_x^2} - \frac{2\bar{\rho}_x^2}{2\bar{\rho}_x^2 + a_x^2} \right) \right] \quad (5.33)$$

and $\mathbf{H}_{ci}(f)$ is the Fourier transform of $\mathbf{h}_{ci}(t)$. We would like to see how much performance advantage we gain from using the optimal processor instead of the conventional one. That is, we are interested in

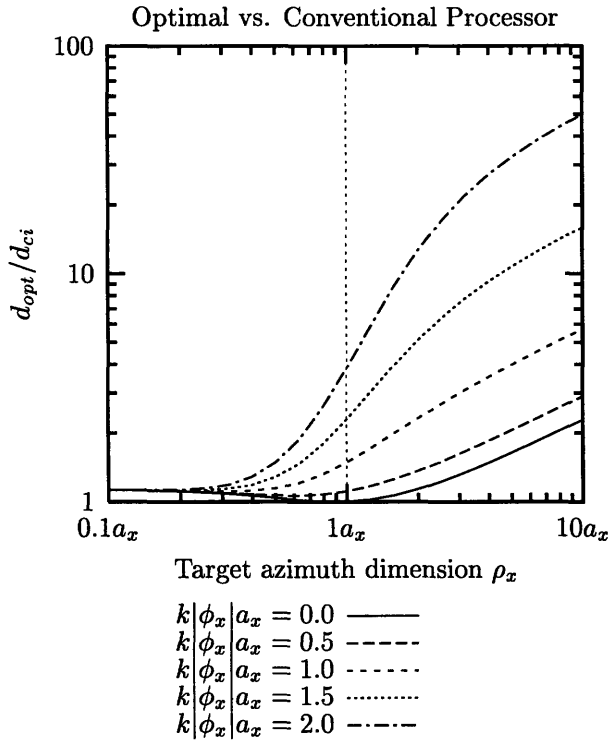
$$\frac{d_{opt}^2}{d_{ci}^2} = \frac{1 + \frac{1}{\sqrt{2}} \text{DNR}}{\sqrt{\pi}} \sqrt{\frac{a_x^2}{2\bar{\rho}_x^2 + a_x^2}} \sqrt{\frac{\left(\frac{\rho_x^2}{a_x^2} + 1\right)^2 + \left(\frac{k\rho_x^2}{R_x}\right)^2}{1 + \left(\frac{k\rho_x^2}{R_x}\right)^2}} \exp \left[(k\phi_x a_x)^2 \left(\frac{2\bar{\rho}_x^2}{\bar{\rho}_x^2 + a_x^2} - \frac{2\bar{\rho}_x^2}{2\bar{\rho}_x^2 + a_x^2} \right) \right] \int \frac{\exp \left[- \left(f' + k\phi_x \frac{2\bar{\rho}_x^2}{\sqrt{2\bar{\rho}_x^2 + a_x^2}} \right)^2 \right]}{1 + \text{DNR} \exp \left[- \frac{a_x^2}{2\bar{\rho}_x^2 + a_x^2} f'^2 \right]} df' \quad (5.34)$$

In the following plots, we see that the optimal processor out-performs the conventional imager-receiver in two major ways. From Figure 5-9, it is clear that the performance gain of the optimal

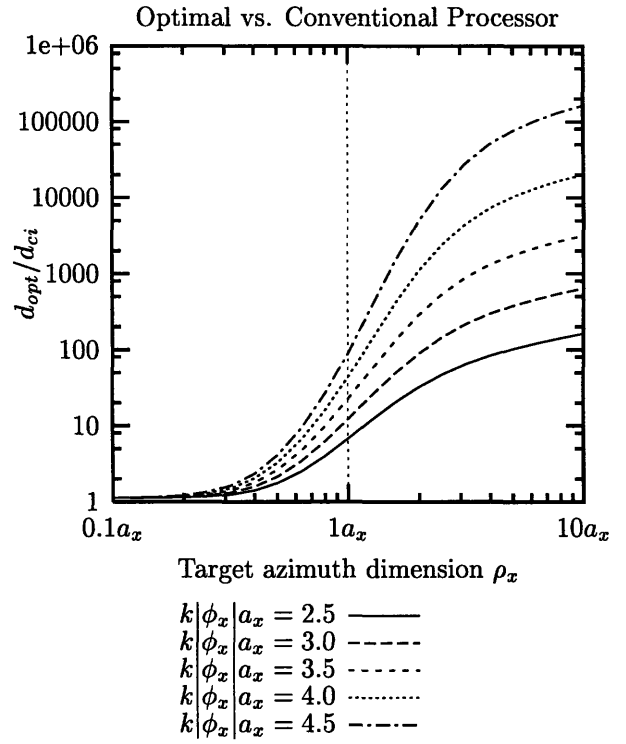
receiver over the conventional one is generally an increasing function of the target size,² due to the chirp bandwidth mismatch between the conventional-imager filter and the specular mirror return. From Figure 5-10, we see that the performance gain is also an increasing function of the tilt, because the conventional receiver suffers from not being able to shift its chirp frequency band to match that of the target return. The combination of these two effects imply that the conventional receiver is severely sub-optimal for detecting a large tilted specular mirror.

We are also going to explore how the curvature affects our detection performance. The effect of increasing curvature is essentially one of reducing the effective size of the mirror. In the case of a high tilt, this implies we lose performance gain as the curvature increases. In the case of an untilted mirror, we lose performance gain only for a large mirror ($\rho_x = 4a_x, \rho_x = 8a_x$ in the plots) because of the effect explained by the footnote on the previous page and the graph in Figure 5-9 (c).

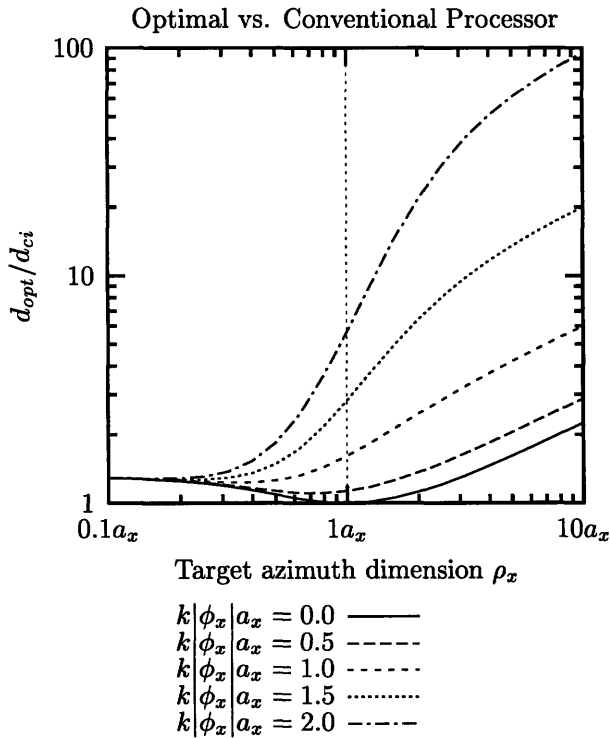
²There is an exception for the low-tilt small-target region – the performance gain decreases a little as the target size grows, until the target reaches the size roughly equal to that of the aperture. In order to understand this, let us consider a specular mirror without tilt. When the target is of negligible size, i.e. $2\rho_x^2 \ll a_x^2$, the bandwidth of the target return is approximately the same as that of the uniform clutter, $\frac{v}{a_x}$, and occupies the same bandwidth around the center frequency ($f = 0$.) Increasing the target size in this region would shrink the target signal's bandwidth, causing it to be more concentrated around $f = 0$ where the uniform clutter's energy is the strongest. This reduction in the effective SNR due to an increase in clutter energy inclusion is inevitable for the optimal receiver, and $\frac{d_{opt}}{d_{ci}}$ continues to decrease until the target size reaches a point (almost the size of the aperture for this case) when the advantage of the optimal processor over the conventional processor from correctly matching the chirp bandwidth supersedes the disadvantage the optimal processor suffers from due to more clutter energy inclusion, and the performance gain $\frac{d_{opt}}{d_{ci}}$ increases again beyond this point. Note that this effect is more prominent under a high DNR. Also, this is an effect of $\frac{d_{opt}}{d_{ci}}$ and not an effect of d_{opt} , i.e. only the relative performance between the optimal and the conventional receiver for detecting a specular mirror of the same size shows up as a decreasing function of ρ_x over this region; the actual value of d_{opt} is an increasing function of ρ_x in the same region as shown in Figure 5-7.



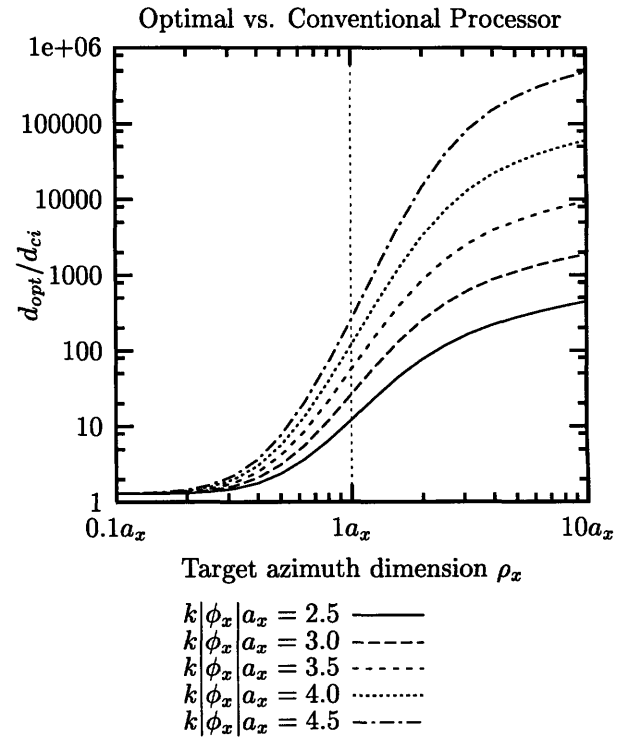
(a) DNR = 10, $R_x \rightarrow \pm\infty$



(b) DNR = 10, $R_x \rightarrow \pm\infty$



(c) DNR = 100, $R_x \rightarrow \pm\infty$



(d) DNR = 100, $R_x \rightarrow \pm\infty$

Figure 5-9: Effective signal-to-noise ratio comparison (against target size ρ_x) of optimal processor vs. conventional processor

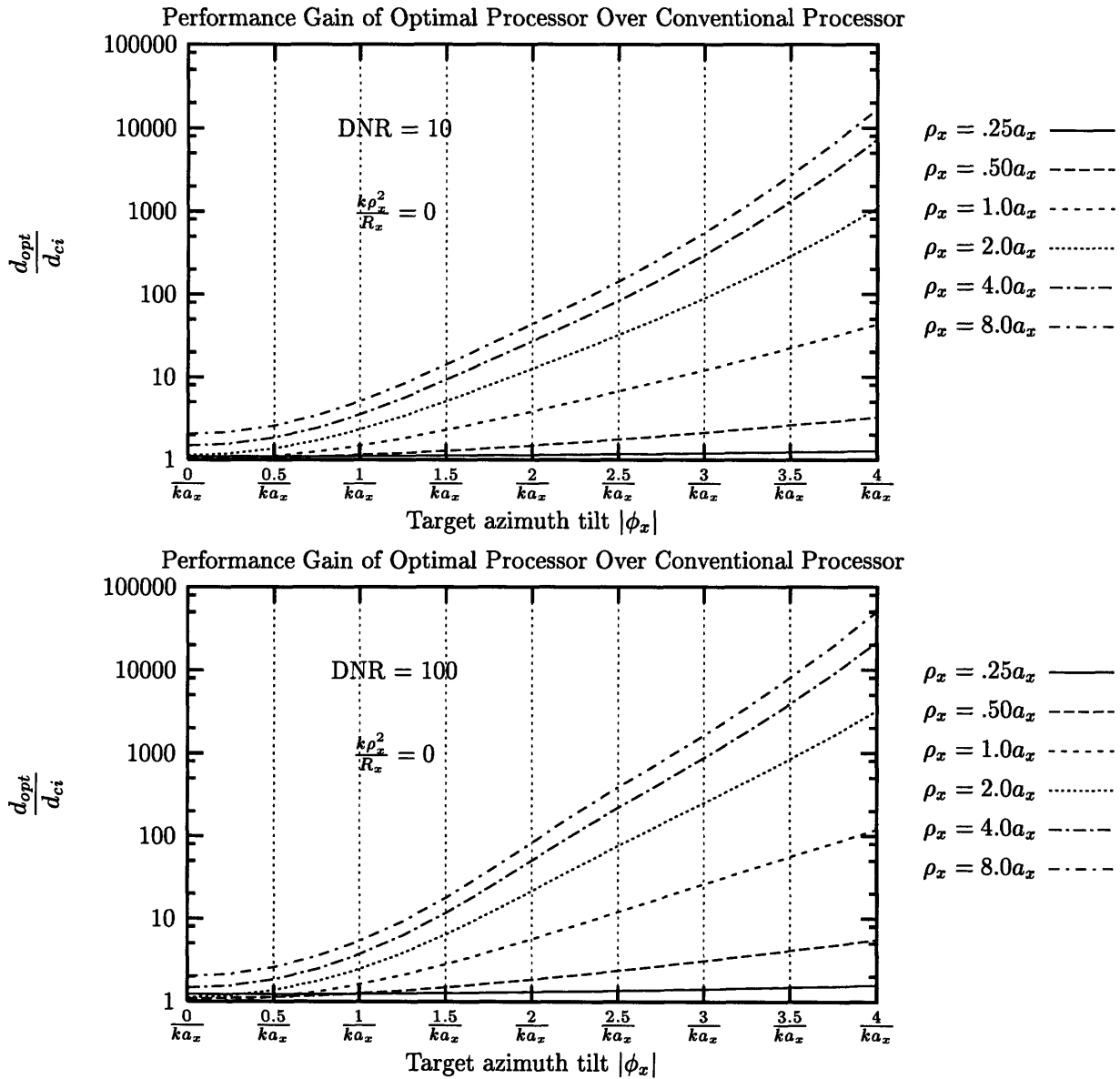


Figure 5-10: Effective signal-to-noise ratio comparison (against target tilt $|\phi_x|$) of optimal processor vs. conventional processor

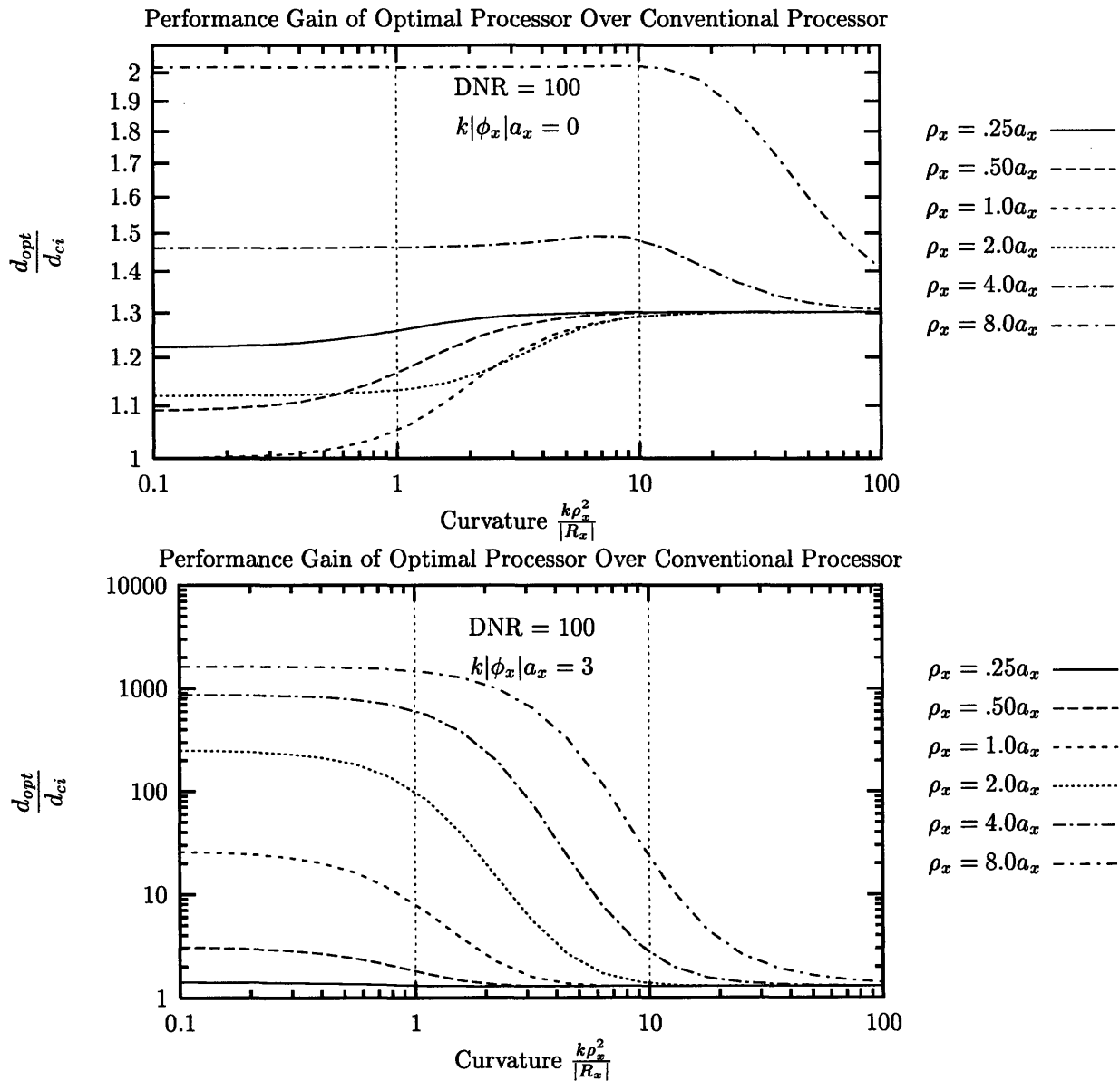


Figure 5-11: Effective signal-to-noise ratio comparison (against target curvature $\frac{k\rho_x^2}{|R_x|}$) of optimal processor vs. conventional processor

5.1.4 Adaptive (Optimized) Multi-resolution Processor

The conventional imager's performance suffers severely due to its inability to account for either the mismatch of the integration time with the specular mirror return duration, or the separation of the chirp and intensity time centers of the specular mirror return. We would like to modify our multi-resolution receiver to address these issues. We now define the adaptive MR filter as,

$$\mathbf{h}_{mr*}(t) = \exp \left[-j \frac{kv^2}{L} (t - t_c)^2 - \frac{k^2 a_x^2 v^2}{2L^2} \frac{1}{\kappa^2} (t - t_i)^2 \right] \quad (5.35)$$

where t_i and t_c are given by the specular mirror return (3.30) and κ is chosen to match the return duration Δt_{sm} ,

$$\kappa = \frac{a_x}{\sqrt{2\bar{\rho}_x^2 + a_x^2}} \quad (5.36)$$

such that in the absence of the uniform clutter, this adaptive MR processor would exactly match the specular mirror return (up to a constant scale) and therefore would be the optimal processor. i.e. The only difference between this adaptive MR processor and the optimal processor is that we have omitted the whitening filter in the former. We can also think of the adaptive MR processor as the best processor one could use without sufficient knowledge about the clutter to build such a whitening filter, because in reality, we may not have much prior information about either the clutter's geometry or its statistics. So, by omitting the whitening filter, we avoid the danger of degrading our signal-to-noise ratio by incorrectly filtering the radar return.

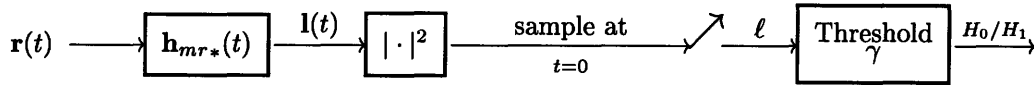


Figure 5-12: Adaptive multi-resolution receiver structure

This way, we find the effective SNR using

$$d_{mr}^2 \equiv \frac{|\langle \mathbf{1} | H_1 \rangle - \langle \mathbf{1} | H_0 \rangle|^2}{\text{var}(\mathbf{1} | H_0 \text{ or } H_1)} = \frac{|\langle \mathbf{1} | H_1 \rangle|^2}{\langle \ell | H_0 \rangle} \quad (5.37)$$

where $\mathbf{l} = \mathbf{l}(t = 0)$. Then

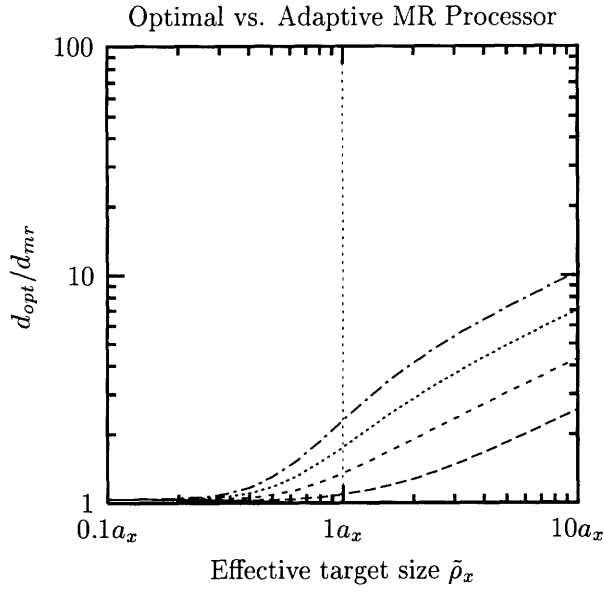
$$d_{mr}^2 = \frac{\left| \int |y_{sm}(t)|^2 dt \right|^2}{\int [S_w(f) + S_{y_{uc}}(f)] |Y_{sm}(f)|^2 df} \quad (5.38)$$

$$= \frac{\text{SNR}_{sm}}{1 + \text{DNR} \sqrt{\frac{2\tilde{\rho}_x^2 + a_x^2}{2\tilde{\rho}_x^2 + 2a_x^2}} \exp \left[-(k\phi_x a_x)^2 \frac{2\tilde{\rho}_x^4}{(\tilde{\rho}_x^2 + a_x^2)(2\tilde{\rho}_x^2 + a_x^2)} \right]} \quad (5.39)$$

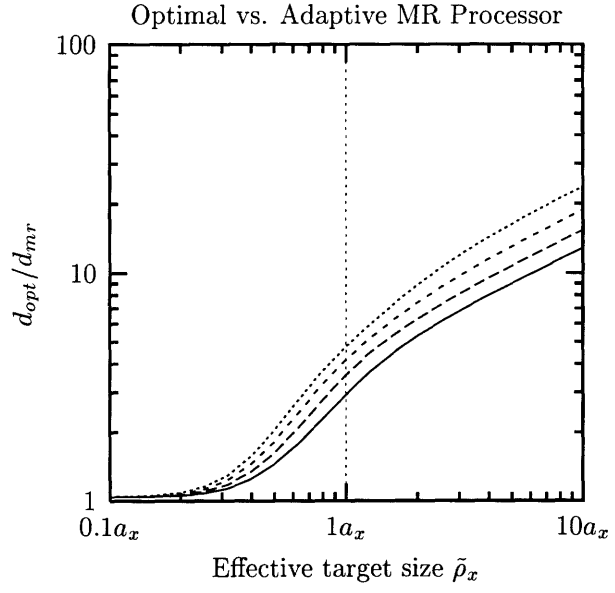
How much uniform clutter degradation is incurred on the specular mirror return depends on the tilt (numerator of the above expression). But when the clutter is absent ($\text{DNR} \ll 1$), d_{mr}^2 approaches SNR_{sm} .

The improvement of using the optimal processor over the adaptive MR processor is not dramatic. In particular, for either a specular mirror with a high tilt or a large effective dimension, the clutter will behave like white noise (the frequency spectrum of the clutter is essentially flat for the frequency band of the specular mirror return (Figure 5-5), and the advantage of using the whitening filter in the optimal filter over the adaptive MR processor is greatly reduced.

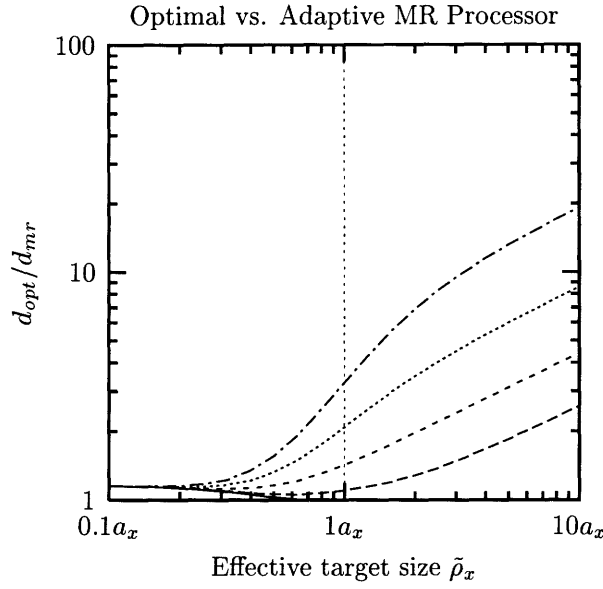
In conclusion, the optimal processor has prior information about the target geometric parameters to best match the target return's chirp bandwidth and shift, as well as the noise statistics of the clutter to compensate for the detection. However the whitening filter in the optimal filter may not be essential, depending on the geometry of the specular mirror.



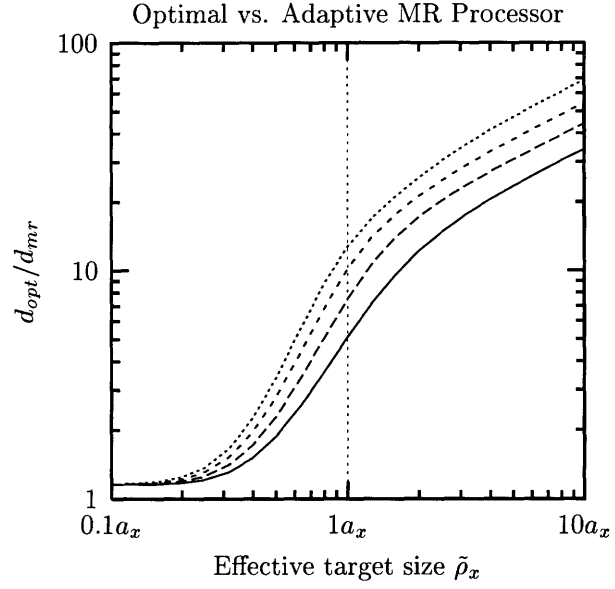
(a) DNR = 10



(b) DNR = 10



(a) DNR = 100



(b) DNR = 100

Figure 5-13: Effective signal-to-noise ratio comparison (against effective target size $\tilde{\rho}_x$) of optimal processor vs. adaptive MR processor

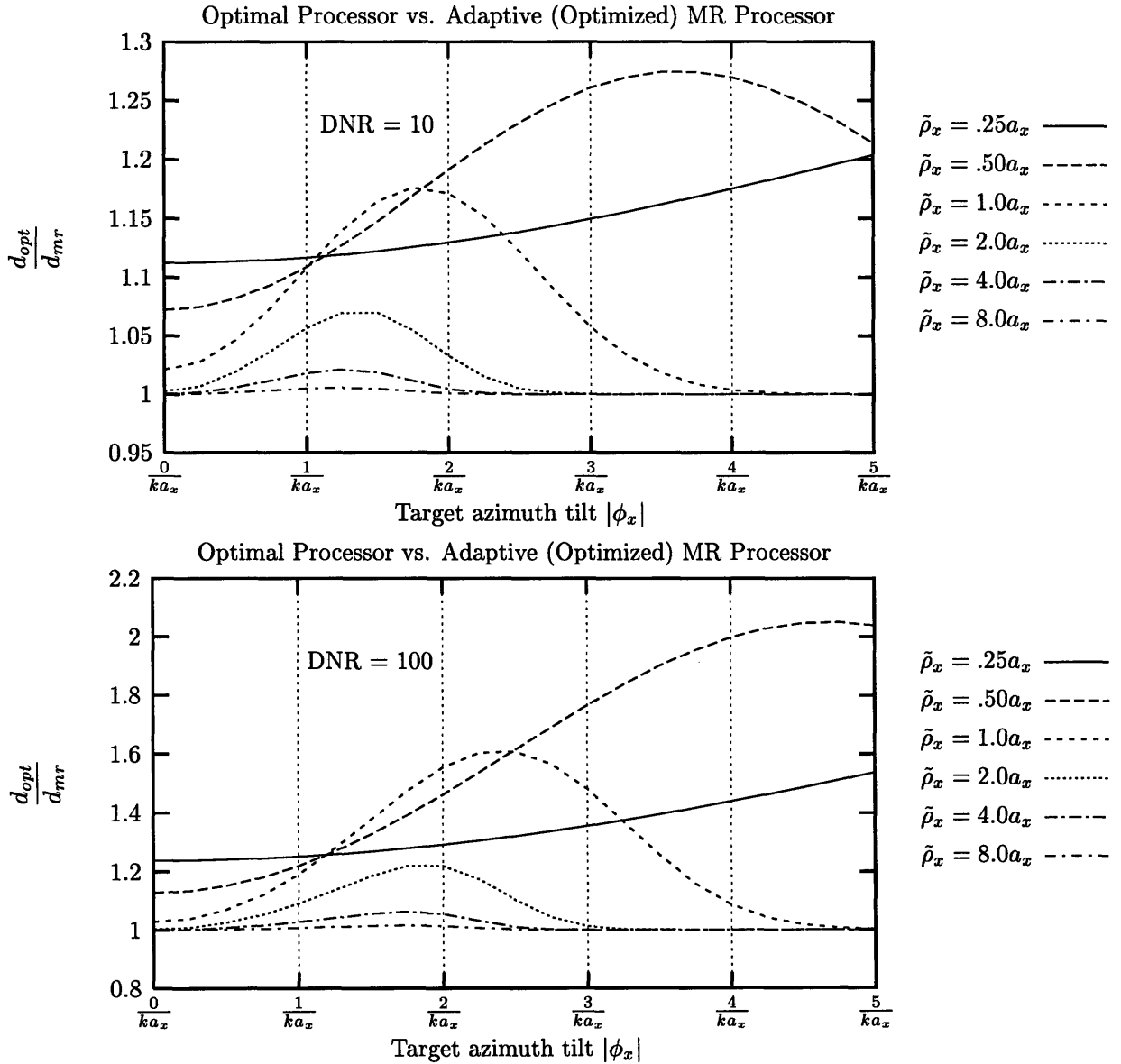


Figure 5-14: Effective signal-to-noise ratio comparison (against target tilt $|\phi_x|$) of optimal processor vs. adaptive MR processor

5.2 Detection of a Diffuse Target

After comparing how well an optimal system and the conventional/MR receivers perform for detecting the man-made target in uniform diffuse clutter in the presence of receiver noise, we would like to repeat the problem for a man-made clutter. At the time of this writing, we have not solved some of the challenging technicalities involved in evaluating the performance of the optimal system for this problem. We shall take the reasonable compromise of examining a special case when the uniform diffuse clutter's energy is negligible compared to the receiver noise ($\text{DNR} \ll 1$), and therefore we can omit the diffuse clutter in the target model for our problem.

5.2.1 Idealized Binary Hypothesis Test

In an idealized situation, our man-made clutter, or diffuse target is located at the origin of the target terrain. Receiver noise with identical statistics is present under both hypothesis H_0 and hypothesis H_1 . Under our null hypothesis H_0 , the diffuse target is absent, and under hypothesis H_1 , the diffuse target is present.

$$\begin{aligned} H_0 : \quad \mathbf{T}(\bar{\rho}) &= 0 \\ H_1 : \quad \mathbf{T}(\bar{\rho}) &= \mathbf{T}_{dt}(\bar{\rho}) \end{aligned} \tag{5.40}$$

where $\mathbf{T}_{dt}(\bar{\rho})$ was defined in Chapter 3. The received radar return is

$$\begin{aligned} H_0 : \quad \mathbf{r}(t) &= \mathbf{w}(t) \\ H_1 : \quad \mathbf{r}(t) &= \mathbf{y}_{dt}(t) + \mathbf{w}(t) \end{aligned} \tag{5.41}$$

where

$\mathbf{y}_{dt}(t)$ = return from diffuse target located at origin

$\mathbf{w}(t)$ = receiver noise with spectral height N_o

With the diffuse target replacing the specular mirror, the problem formulation is exactly in parallel with that in the previous section. The only exception is that we have left out the uniform diffuse clutter. This hypothesis testing problem is about detecting a non-stationary Gaussian signal from white Gaussian noise.

5.2.2 Optimal Processor

The optimal Neyman-Pearson processor for this type of detection problem is derived in [27]. We shall apply the general results to our problem without proof.

Receiver Structure

A time-varying linear filter is required to optimally detect the non-stationary random signal. In our particular case, the impulse response of this filter cannot be represented by a closed form expression.

We have to resort to a characterization using the Karhunen-Loève (K-L) expansion.

$$\begin{aligned} \langle \mathbf{y}_{dt}(t)\mathbf{y}_{dt}^*(u) \rangle &= C_{tr}C_{dt} \exp \left[-\frac{k^2\rho_x^2v^2}{2L}(t-u)^2 \right] \\ &\quad \exp \left[-\left(\frac{k^2\alpha_x^2v^2}{2L^2} - j\frac{kv^2}{L} \right) t^2 - \left(\frac{k^2\alpha_x^2v^2}{2L^2} + j\frac{kv^2}{L} \right) u^2 \right] \end{aligned} \quad (5.42)$$

$$= \sum_{n=0}^{\infty} \lambda_n \phi_n(t)\phi_n^*(u) \quad (5.43)$$

where the $\{\phi_n(t)\}$ are orthogonal and have unity-square integrals,

$$\int \phi_m(t)\phi_n^*(t)dt = \begin{cases} 1, & m = n \\ 0, & m \neq n \end{cases} \quad (5.44)$$

and the expected energy is

$$\langle E_{\mathbf{y}_{dt}} \rangle = \int \langle \mathbf{y}_{dt}(t)\mathbf{y}_{dt}^*(t) \rangle dt = \sum_{n=0}^{\infty} \lambda_n \quad (5.45)$$

The results are³

$$\lambda_n = C_{tr} C_{dt} \sqrt{2\pi} \frac{L}{kv} \frac{(a_x^2 + \rho_x^2 - a_x \sqrt{2\rho_x^2 + a_x^2})^{n/2}}{(a_x^2 + \rho_x^2 + a_x \sqrt{2\rho_x^2 + a_x^2})^{(n+1)/2}}, \quad n = 0, 1, 2, \dots \quad (5.46)$$

$$= \langle E_{y_{dt}} \rangle \sqrt{2} \left[1 + \frac{\rho_x^2}{a_x^2} + \sqrt{\frac{2\rho_x^2}{a_x^2} + 1} \right]^{-1/2} \left(\frac{a_x^2 + \rho_x^2 - a_x \sqrt{2\rho_x^2 + a_x^2}}{a_x^2 + \rho_x^2 + a_x \sqrt{2\rho_x^2 + a_x^2}} \right)^{n/2} \quad (5.47)$$

$$\phi_n(t) = \sqrt{\frac{kv}{L} \frac{1}{2^n n!}} \left(\frac{a_x \sqrt{2\rho_x^2 + a_x^2}}{\pi} \right)^{1/4} \exp \left[\left(j \frac{kv^2}{L} - \frac{k^2 a_x \sqrt{2\rho_x^2 + a_x^2} v^2}{2L^2} \right) t^2 \right] H_n \left(\frac{k \sqrt{a_x \sqrt{2\rho_x^2 + a_x^2}} v}{L} t \right) \quad (5.48)$$

and $\{H_n(x)\}$ are the Hermite polynomials [10]

$$H_n(x) = (-1)^n e^{x^2} \frac{d^n}{dx^n} (e^{-x^2}). \quad (5.49)$$

We see that the eigenvalues λ_n form a decaying geometrical sequence proportional to the energy of the diffuse target return. Their decay rate, the term inside the parentheses in (5.47), is a monotonically increasing function of the target size ρ_x and has the asymptotic values

$$\lim_{\rho_x \rightarrow 0} \left(\frac{a_x^2 + \rho_x^2 - a_x \sqrt{2\rho_x^2 + a_x^2}}{a_x^2 + \rho_x^2 + a_x \sqrt{2\rho_x^2 + a_x^2}} \right)^{1/2} = 0 \quad (5.50)$$

$$\lim_{\rho_x \rightarrow \infty} \left(\frac{a_x^2 + \rho_x^2 - a_x \sqrt{2\rho_x^2 + a_x^2}}{a_x^2 + \rho_x^2 + a_x \sqrt{2\rho_x^2 + a_x^2}} \right)^{1/2} = 1 \quad (5.51)$$

Therefore, given a fixed expected energy $\langle E_{y_{dt}} \rangle$, ρ_x affects how the energy of the target return is distributed among the different eigenfunctions $\phi_n(t)$. We see from the stationary part of (5.42) that an increasing ρ_x shortens the correlation time of the target return $y_{dt}(t)$. It is no surprise that a large ρ_x implies that the energy of the return is spread out among many of the eigenfunctions (λ_n decays slowly) because this is just the uncertainty principle carried over to a non-stationary stochastic signal.

³By using (8.957.1) or (7.374.8) in [10], we can solve the Fredholm equation in question,

$$\int C_{tr} C_{dt} \exp \left[-\frac{k^2 \rho_x^2 v^2}{2L} (t-u)^2 - \left(\frac{k^2 a_x^2 v^2}{2L^2} \right) (t^2 + u^2) \right] \psi_n(u) du = \lambda_n \psi_n(t),$$

Then,

$$\phi_n(t) = \exp \left[j \frac{kv^2}{L} t^2 \right] \psi_n(t)$$

The λ_n are arranged in decreasing order forming a geometric sequence.

The likelihood ratio test can now be written out in terms of the K-L expansion, i.e., as a summation of weighted and magnitude-squared independent complex Gaussian random variables

$$\ell = \ln \frac{p(\mathbf{r}(t) | H_1)}{p(\mathbf{r}(t) | H_0)} = \frac{1}{N_o} \sum_{n=0}^{\infty} \frac{\lambda_n}{\lambda_n + N_o} |\mathbf{r}_n|^2 \underset{H_0}{\overset{H_1}{>}} \gamma \quad (5.52)$$

where

$$\mathbf{r}_n = \int \mathbf{r}(t) \phi_n^*(t) dt \quad (5.53)$$

and the threshold γ is chosen to satisfy the desired false alarm probability. There are several ways to implement a system to compute this likelihood ratio. We will state two ways here.

The first implementation is a rather straightforward estimator-correlator which has the interpretation of correlating the return signal with a minimum-mean-squared-error (MMSE) estimate of the target return $\hat{\mathbf{y}}_{dt}(t)$, given by the output of the filter $\mathbf{h}_{dt}(t, u)$. That is, ⁴

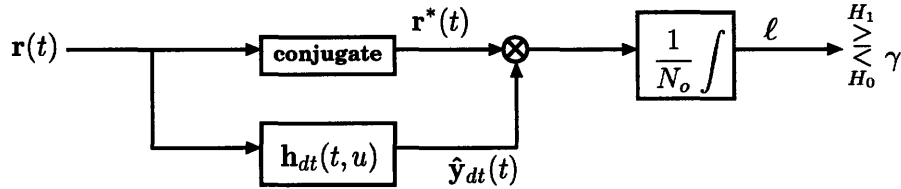


Figure 5-15: Estimator-correlator realization for optimal detection of diffuse target in white receiver noise

$$\ell = \frac{1}{N_o} \int \int \mathbf{r}^*(t) \mathbf{h}_{dt}(t, u) \mathbf{r}(u) dt du \underset{H_0}{\overset{H_1}{>}} \gamma \quad (5.54)$$

where

$$\mathbf{h}_{dt}(t, u) = \sum_{n=0}^{\infty} \frac{\lambda_n}{\lambda_n + N_o} \phi_n(t) \phi_n^*(u) \quad (5.55)$$

Another way to compute ℓ is by filtering the returned signal with the functional square-root of $\mathbf{h}_{dt}(t, u)$

$$\mathbf{g}_{dt}(t, u) = \sum_{n=0}^{\infty} \sqrt{\frac{\lambda_n}{\lambda_n + N_o}} \phi_n(t) \phi_n^*(u) \quad (5.56)$$

⁴The optimal filter $\mathbf{h}_{dt}(t, u)$ chosen here is not only time-varying but also non-causal, but again, we are not concerned about causality because off-line processing can be assumed. There is also a causal counterpart of this estimator-correlator receiver structure listed in [27].

Then taking the squared magnitude and integrating the output, we get

$$\ell = \frac{1}{N_o} \int dz \left| \int \mathbf{g}_{dt}(z, t) \mathbf{r}(t) dt \right|^2 \underset{H_0}{\overset{H_1}{>}} \gamma. \quad (5.57)$$

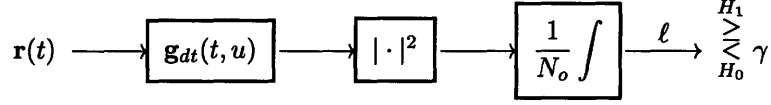


Figure 5-16: Filter-squarer-integrator realization for optimal detection of diffuse target in white receiver noise

Since the eigenvalues converge to 0 geometrically, we may make approximations by truncating all the above summations at an n such that that the resulting error in the energy (5.45) from such an approximation is bounded by a chosen tolerance. We may simplify the actual implementations of $\mathbf{h}_{dt}(t, u)$ or $\mathbf{g}_{dt}(t, u)$ this way.

Performance of Optimal Receiver

The log-likelihood ratio (5.52) is a weighted sum of $|\mathbf{r}_n|^2$, which are independent, exponentially distributed random variables,

$$\begin{aligned} \langle |\mathbf{r}_n|^2 | H_0 \rangle &= N_o, & p_{|\mathbf{r}_n|^2}(x | H_0) &= \frac{1}{N_o} \exp\left(-\frac{x}{N_o}\right), & x \geq 0 \\ \langle |\mathbf{r}_n|^2 | H_1 \rangle &= N_o + \lambda_n, & p_{|\mathbf{r}_n|^2}(x | H_1) &= \frac{1}{N_o + \lambda_n} \exp\left(-\frac{x}{N_o + \lambda_n}\right), & x \geq 0 \end{aligned} \quad (5.58)$$

Equivalently, let

$$\ell_n \equiv \frac{1}{N_o} \frac{\lambda_n}{N_o + \lambda_n} |\mathbf{r}_n|^2 \quad (5.59)$$

such that

$$\ell = \sum_{n=0}^{\infty} \ell_n \quad (5.60)$$

$$\begin{aligned} \langle \ell_n | H_0 \rangle &= \frac{\lambda_n}{N_o + \lambda_n}, & p_{\ell_n}(x | H_0) &= \frac{N_o + \lambda_n}{\lambda_n} \exp\left(-\frac{N_o + \lambda_n}{\lambda_n} x\right), & x \geq 0 \\ \langle \ell_n | H_1 \rangle &= \frac{\lambda_n}{N_o}, & p_{\ell_n}(x | H_1) &= \frac{N_o}{\lambda_n} \exp\left(-\frac{N_o}{\lambda_n} x\right), & x \geq 0 \end{aligned} \quad (5.61)$$

Again since the eigenvalues λ_n are a decaying geometric sequence, we can approximate the log-

likelihood ratio by a finite summation.

$$\ell \approx \ell(N) \equiv \sum_{n=0}^N \ell_n \quad (5.62)$$

The resulting detection and false alarm probabilities are (Appendix B),

$$P_F = \int_{\gamma}^{\infty} p_{\ell}(x | H_0) dx \approx \int_{\gamma}^{\infty} p_{\ell(N)}(x | H_0) dx = \sum_{i=0}^N \left(\prod_{\substack{j=0 \\ j \neq i}}^N \frac{1}{1 - \frac{\alpha_j}{\alpha_i}} \right) e^{-\alpha_i \gamma} \quad (5.63)$$

$$P_D = \int_{\gamma}^{\infty} p_{\ell}(x | H_1) dx \approx \int_{\gamma}^{\infty} p_{\ell(N)}(x | H_1) dx = \sum_{i=0}^N \left(\prod_{\substack{j=0 \\ j \neq i}}^N \frac{1}{1 - \frac{\beta_j}{\beta_i}} \right) e^{-\beta_i \gamma} \quad (5.64)$$

where

$$\alpha_n = \frac{N_o + \lambda_n}{\lambda_n}, \quad \beta_n = \frac{N_o}{\lambda_n} \quad (5.65)$$

are the inverses of the conditional means of ℓ_n .

For comparison, we will also use the Gaussian approximation expressions developed in [27].

$$P_F \approx \exp \left[\mu(s) - s\dot{\mu}(s) + \frac{s^2}{2}\ddot{\mu}(s) \right] \text{erfc}_* [s\sqrt{\ddot{\mu}(s)}] \quad (5.66)$$

$$P_D \approx 1 - \exp \left[\mu(s) + (1-s)\dot{\mu}(s) + \frac{(s-1)^2}{2}\ddot{\mu}(s) \right] \text{erfc}_* [(1-s)\sqrt{\ddot{\mu}(s)}] \quad (5.67)$$

for $0 \leq s \leq 1$ only, where

$$\text{erfc}_*(x) = \frac{1}{\sqrt{2\pi}} \int_x^{\infty} \exp \left[-\frac{y^2}{2} \right] dy \quad (5.68)$$

$$\mu(s) = \sum_{n=0}^{\infty} \left[(1-s) \ln \left(1 + \frac{\lambda_n}{N_o} \right) - \ln \left(1 + (1-s) \frac{\lambda_n}{N_o} \right) \right] \quad (5.69)$$

and $\dot{\mu}(s), \ddot{\mu}(s)$ are the derivatives of $\mu(s)$ with respect to s . By varying s between 0 and 1, we can obtain an approximate ROC curve for the region of $P_D > 0.5$ and $P_F < 0.5$. (Extension of this Gaussian approximation to all regions of P_D and P_F does exist but is not applied here.)

For our detection results in the following figures, we define a relevant quantity

$$\text{SNR}_{dt} \equiv \frac{\langle E_{y_{dt}} \rangle}{N_o} = \sum_{n=0}^{\infty} \frac{\lambda_n}{N_o} \quad (5.70)$$

which is the signal-to-noise ratio of the diffuse target.

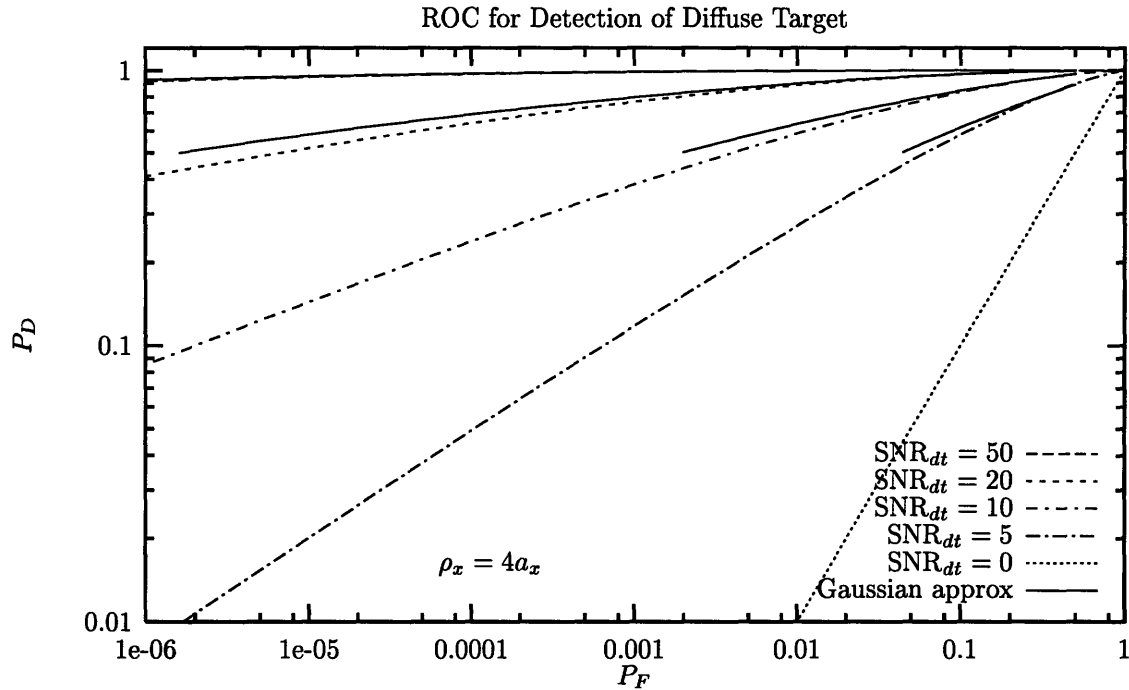
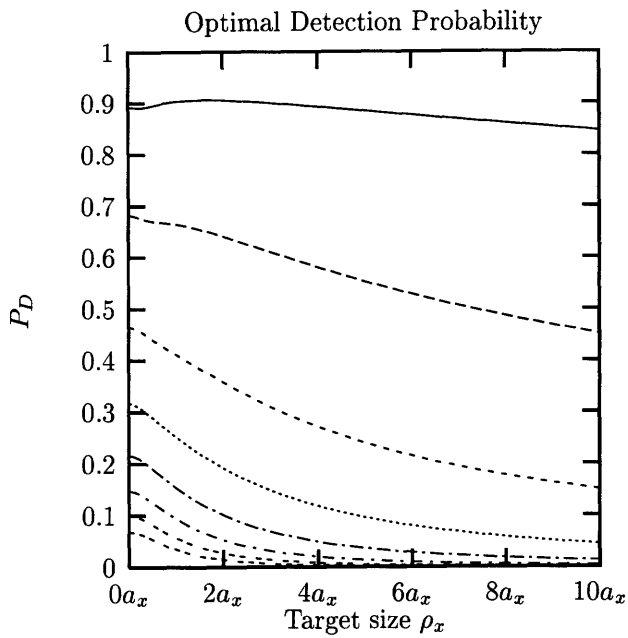


Figure 5-17: Receiver Operating Characteristic for detection of diffuse target return from white receiver noise.

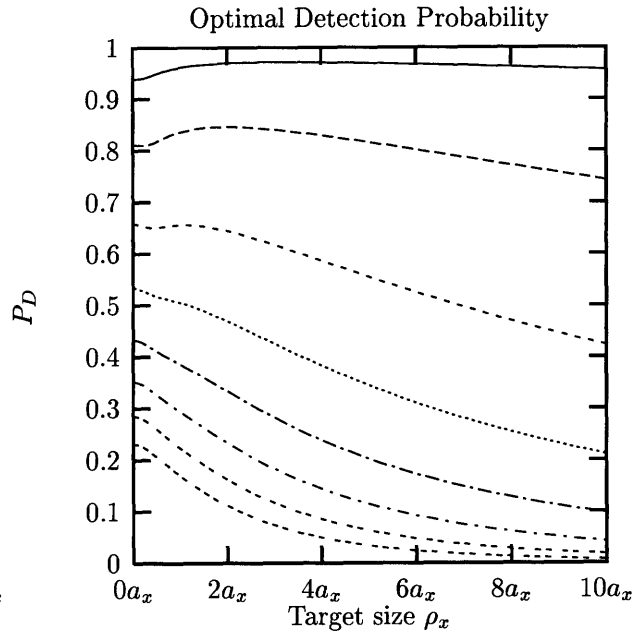
We see from Figure 5-18, especially in the high SNR_{dt} cases, that for a known SNR_{dt} and a fixed desired probability of false alarm, there is an optimal size of the target that yields the highest detection probability. Referring back to (5.47) and (5.51), we see that this phenomenon is related to the diversity problem in communication systems for reliably transmitting orthogonal signals over the optimal number of channels given a power or energy constraint of the transmitted signals [17]. Physically, although a small diffuse target gives a more coherent return than a large one, its intensity is more subject to the risk of random fading due to the smaller possible number of reflecting facets (on the order of a wavelength) on its surface. In order for the target to be “seen” from the radar, it needs to have an appreciable surface area such that very likely, at least a significant portion from the collection of its facets would contribute to the return’s intensity. As the target size increases further, however, the loss of coherence in the target return makes the return behave more like the white receiver noise and detection probability is sacrificed. What exactly the optimal target size is for a particular choice of SNR_{dt} and P_F might be highly subject to the modeling error of the Gaussian-shape intensity assumption of our target.

We can conclude from Figure 5-19 that due to speckle fading, it would take a very high SNR_{dt} to yield a very low miss probability $P_M = 1 - P_D$ for detection of a small diffuse target. This is not the case in detection of a specular mirror in the previous section.

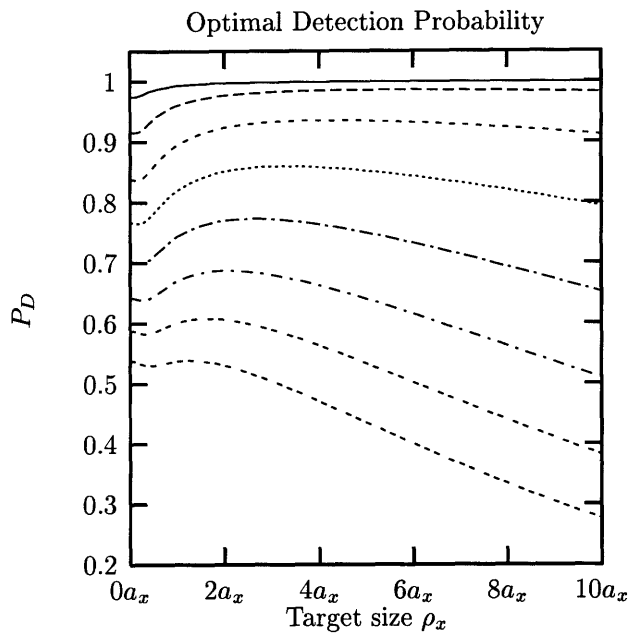
We now proceed to compare the performance of the optimal processor with that of both the conventional processor and the multi-resolution processor. Since we are already familiar with both, and the former is a special case of the latter, we shall go over the MR processor first for convenience.



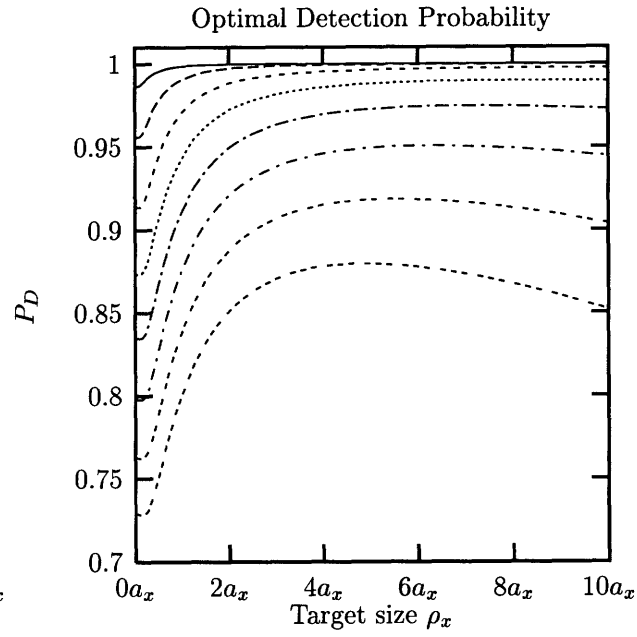
(a) $\text{SNR}_{dt} = 5$



(b) $\text{SNR}_{dt} = 10$



(c) $\text{SNR}_{dt} = 25$

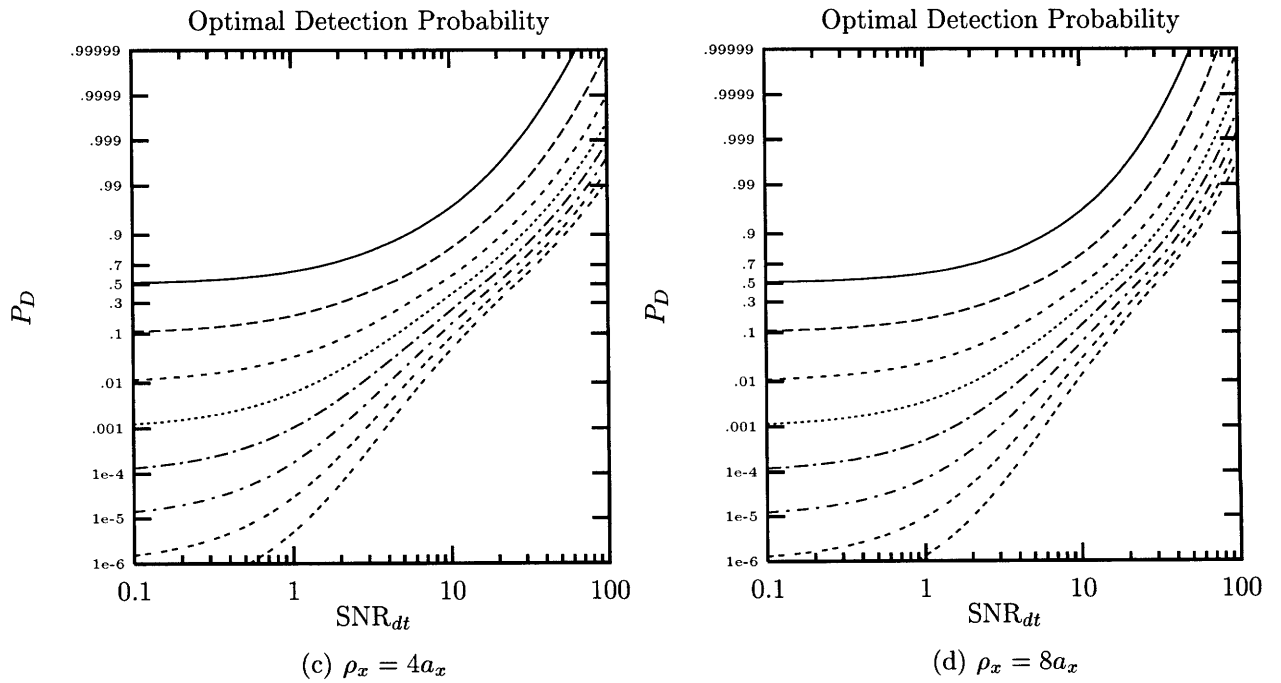
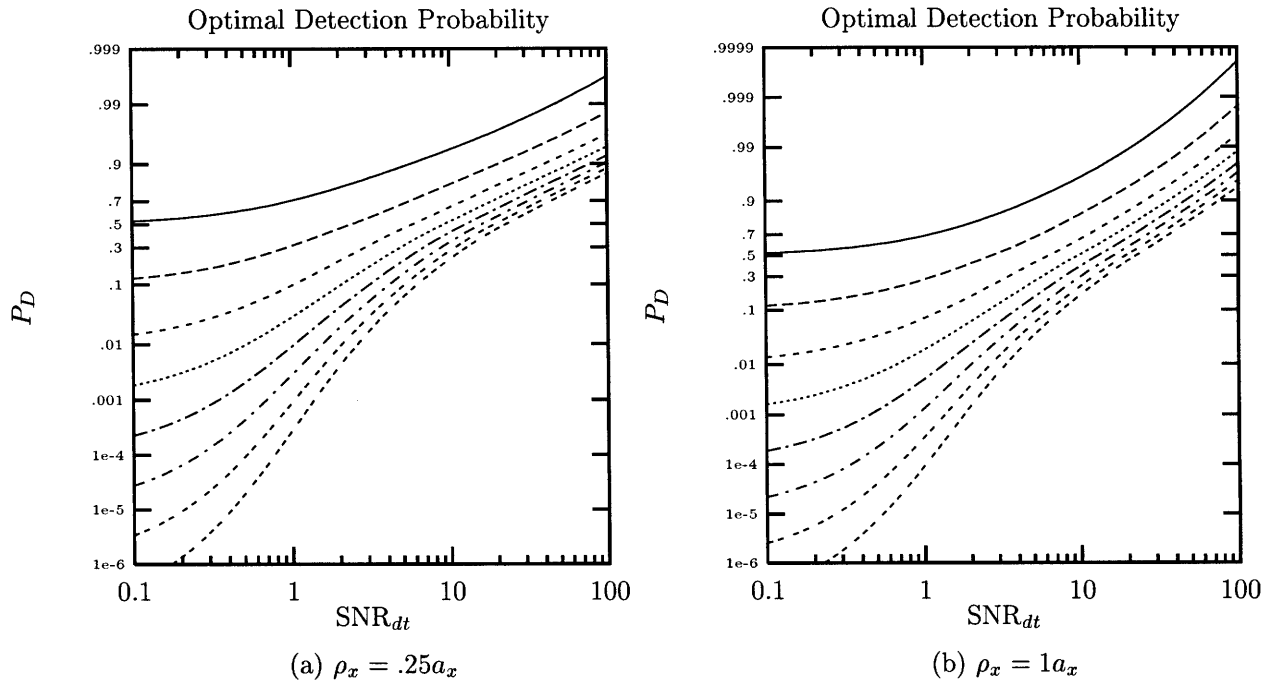


(d) $\text{SNR}_{dt} = 50$

$P_F = .500$ ———
 $P_F = .100$ - - - -
 $P_F = .010$ - · - · -
 $P_F = .001$ ······

$P_F = 1e - 4$ - - - -
 $P_F = 1e - 5$ - - - -
 $P_F = 1e - 6$ - · - · -
 $P_F = 1e - 7$ ······

Figure 5-18: Optimal detection probability versus size of diffuse target ρ_x



$P_F = .500$ ———
 $P_F = .100$ - - - -
 $P_F = .010$ - - - -
 $P_F = .001$ ······

$P_F = 1e - 4$ - - - -
 $P_F = 1e - 5$ - - - -
 $P_F = 1e - 6$ - - - -
 $P_F = 1e - 7$ - - - -

Figure 5-19: Optimal detection probability versus SNR of diffuse target

5.2.3 Adaptive (Optimized) Multi-resolution Imager

In using our multi-resolution imager, we would like to constrain ourselves to forming a SAR-image at one particular κ that would give the best performance, and we always sample at $t = 0$ corresponding

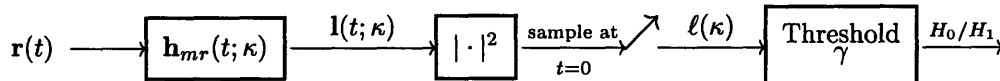


Figure 5-20: Multi-resolution imager with integration period κT_{dw}

to where the target is located and to the peak of $\langle |l_y(t)|^2 \rangle$.

Since our return $\mathbf{r}(t)$ is a Gaussian process, the conditional densities of our sufficient statistic are exponential,

$$p_{l(\kappa)}(x | H_0) = \frac{1}{\ell_w(\kappa)} \exp \left[-\frac{x}{\ell_w(\kappa)} \right], \quad x \geq 0 \quad (5.71)$$

$$p_{l(\kappa)}(x | H_1) = \frac{1}{\ell_y(\kappa) + \ell_w(\kappa)} \exp \left[-\frac{x}{\ell_y(\kappa) + \ell_w(\kappa)} \right], \quad x \geq 0 \quad (5.72)$$

where (using (4.23), (4.21))

$$\ell_y(\kappa) \equiv \langle |l_{y_{dt}}(t = 0; \kappa)|^2 \rangle = E_{y_{dt}} \kappa^2 T_{dw} \frac{2\sqrt{\pi}}{\kappa^2 + 1} (1 + \Re\{\mathbf{P}\} \rho_x^2)^{-1/2} \quad (5.73)$$

$$\ell_w(\kappa) \equiv \langle |l_w(t = 0; \kappa)|^2 \rangle = N_o \sqrt{\pi} \kappa T_{dw} \quad (5.74)$$

and with standard detection results [28],

$$P_F = \exp \left(-\frac{\gamma}{\ell_w(\kappa)} \right) \quad (5.75)$$

$$P_D = \exp \left(-\frac{\gamma}{\ell_y(\kappa) + \ell_w(\kappa)} \right) = (P_F)^{\frac{\ell_w(\kappa)}{\ell_y(\kappa) + \ell_w(\kappa)}} \quad (5.76)$$

Given any P_F , P_D is maximized by minimizing the exponent of the above expression,

$$\kappa_{opt} = \arg \max_{\kappa} P_D = \left(\frac{a_x^2}{2\rho_x^2 + a_x^2} \right)^{1/4} \quad (5.77)$$

such that we are filtering the return with

$$\mathbf{h}_{mr}(t; \kappa_{opt}) = \exp \left[\left(j \frac{kv^2}{L} - \frac{k^2 a_x \sqrt{2\rho_x^2 + a_x^2 v^2}}{2L^2} \right) t^2 \right] \quad (5.78)$$

Within a constant, this is exactly the first eigenfunction of our K-L expansion $\phi_0(t)$ (5.48). This has

the intuitively pleasing interpretation that the adaptive MR processor tries to mimic the optimal filter $\mathbf{h}_{dt}(t, u)$ by using only the first term of the expansion (The functional form of $\mathbf{h}_{mr}(t; \kappa)$ forbids the MR processor mimicking any of the other eigenfunctions, regardless of any κ used.) That is,

$$\ell(\kappa_{opt}) = \left| \int \mathbf{r}(t) \phi_0^*(t) dt \right|^2 \quad (5.79)$$

$$= \int \int \mathbf{r}^*(t) \phi_0(t) \phi_0^*(u) \mathbf{r}(u) dt du \quad (5.80)$$

which is clearly proportional to the first term expansion of (5.54) or the first term in (5.52). Therefore, we can anticipate that if very few of the eigenvalues of our kernel (5.42) are significant compared to the receiver noise energy, corresponding to either a low SNR_{dt} or a small ρ_x , or both, the MR processor will perform nearly as well as the optimal filter. The MR processor is exactly optimal for a point target.

When we substitute κ_{opt} back into (5.76), we get

$$P_D = (P_F) \left[1 + \text{SNR}_{dt} \frac{2a_x}{a_x + \sqrt{2\rho_x^2 + a_x^2}} \right]^{-1} \quad (5.81)$$

We shall now use this result to compare the performance of the optimal diffuse target processor and that of the MR processor in the following plots.

The performance gain of the optimal processor over the MR processor is a monotonically increasing function of the target size ρ_x , confirming our conjecture (Figure 5-21). In Figure 5-22, we see that as SNR_{dt} increases, the detection probability of the MR processor approaches that of the optimal processor. This is because at a certain SNR_{dt} the optimal processor's detection probability slows down its improvement with respect to an increase in SNR_{dt} (Figure 5-19) compared to that of the MR filter. Also, the MR processor is essentially optimal for a high false alarm probability, because the MR processor can achieve the high P_F with the first eigenfunction alone in the target return where the most signal energy is.

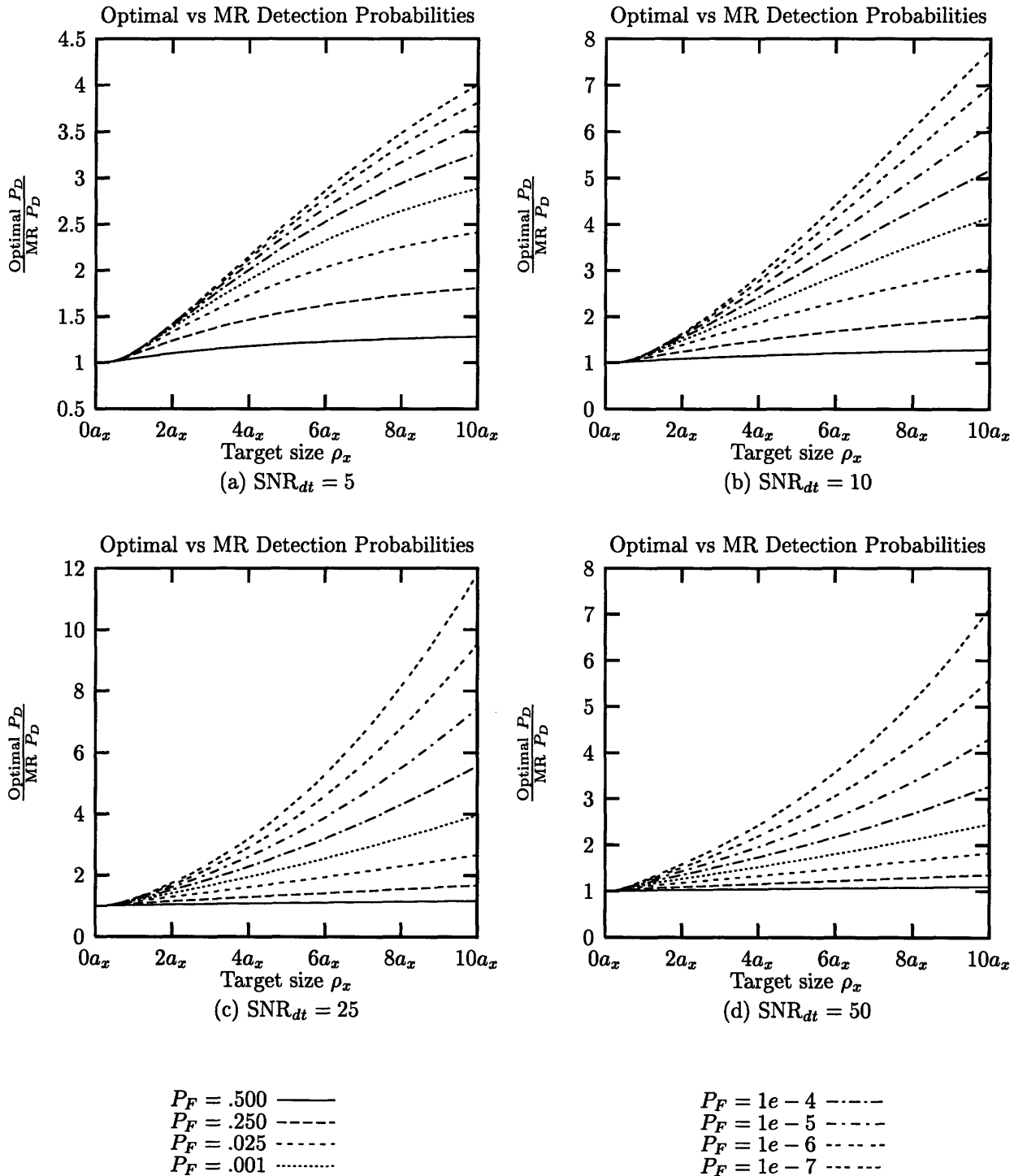


Figure 5-21: Comparison of optimal and MR detection probabilities of a diffuse target (as a function of ρ_x)

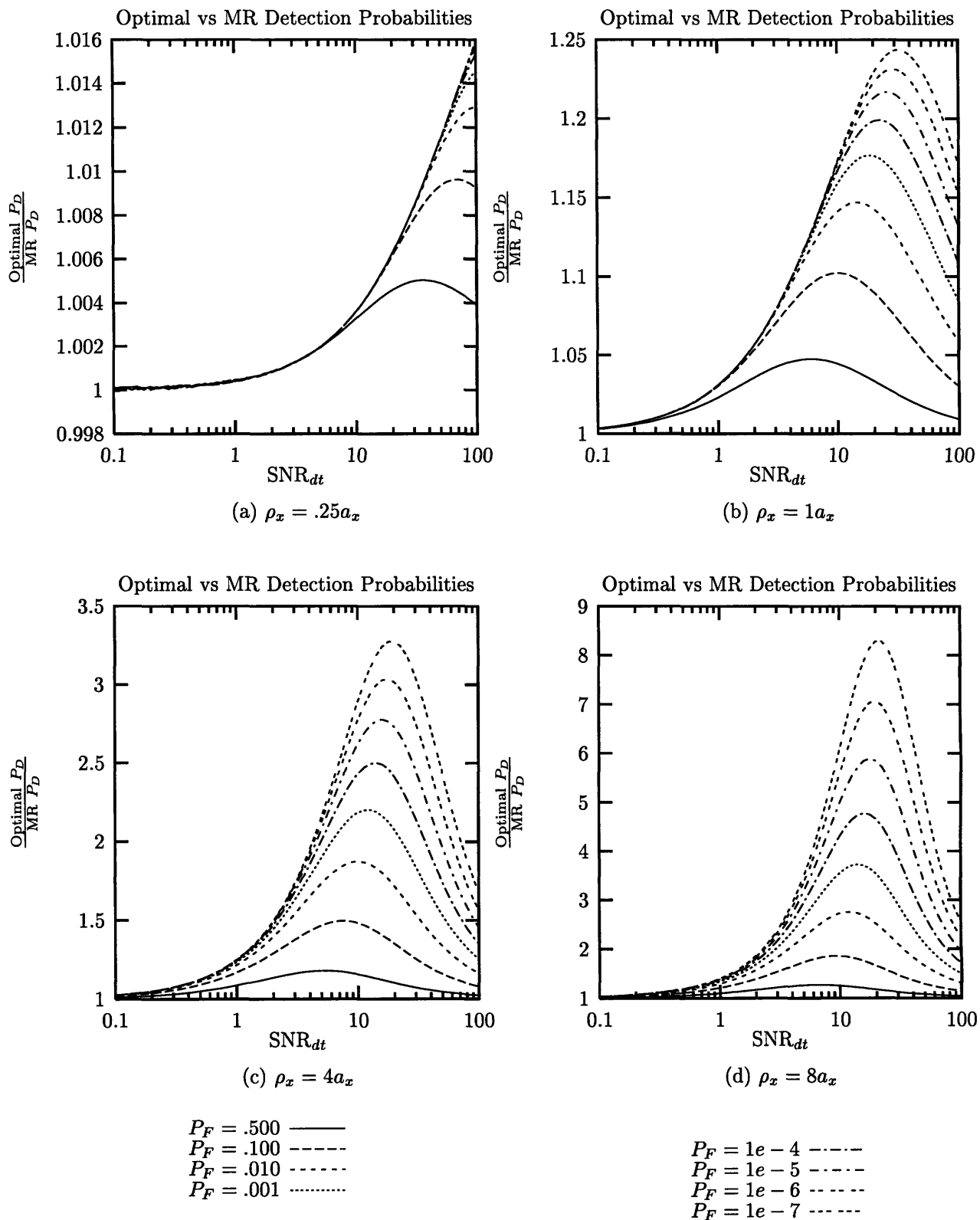


Figure 5-22: Comparison of optimal and MR detection probabilities of a diffuse target (as a function of SNR)

5.2.4 Conventional Processor: Full-dwell-time Imager

The conventional processor is only a special case of the MR processor.

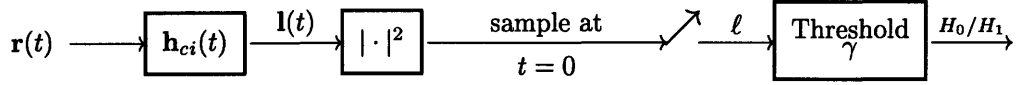


Figure 5-23: Conventional imager with full dwell time integration period T_{dw}

When we substitute $\kappa = 1$ into (5.76), we obtain

$$P_D = (P_F) \left[1 + \text{SNR}_{dt} \frac{a_x}{\sqrt{\rho_x^2 + a_x^2}} \right]^{-1} \quad (5.82)$$

Note that the conventional imager processor is essentially optimal for a small target, because κ_{opt} in the previous section approaches 1 as the target size approaches 0. We also see for a large diffuse target, the conventional processor is moderately worse than the MR processor.

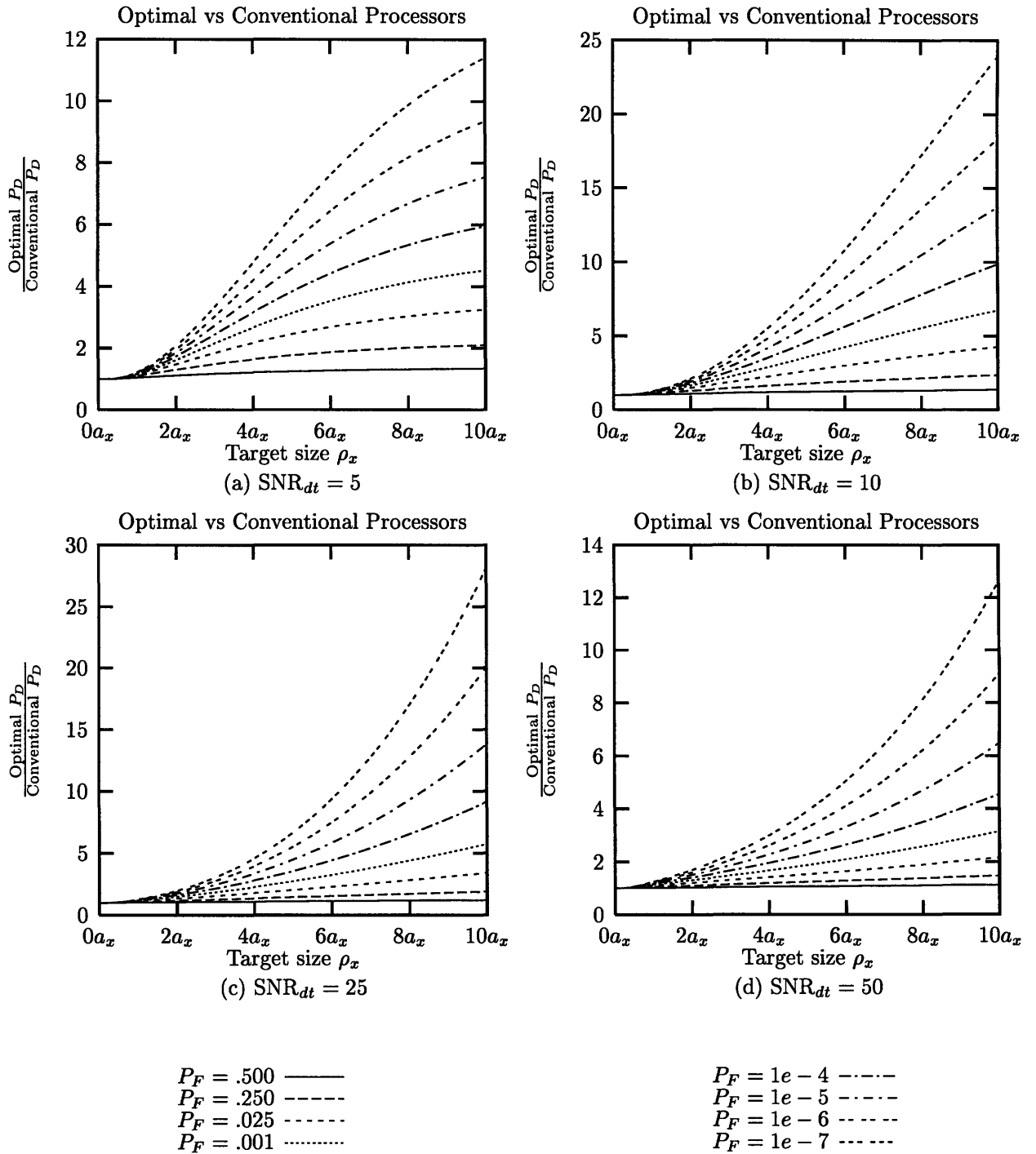


Figure 5-24: Comparison of optimal and conventional detection probabilities of a diffuse target (as a function of ρ_x)

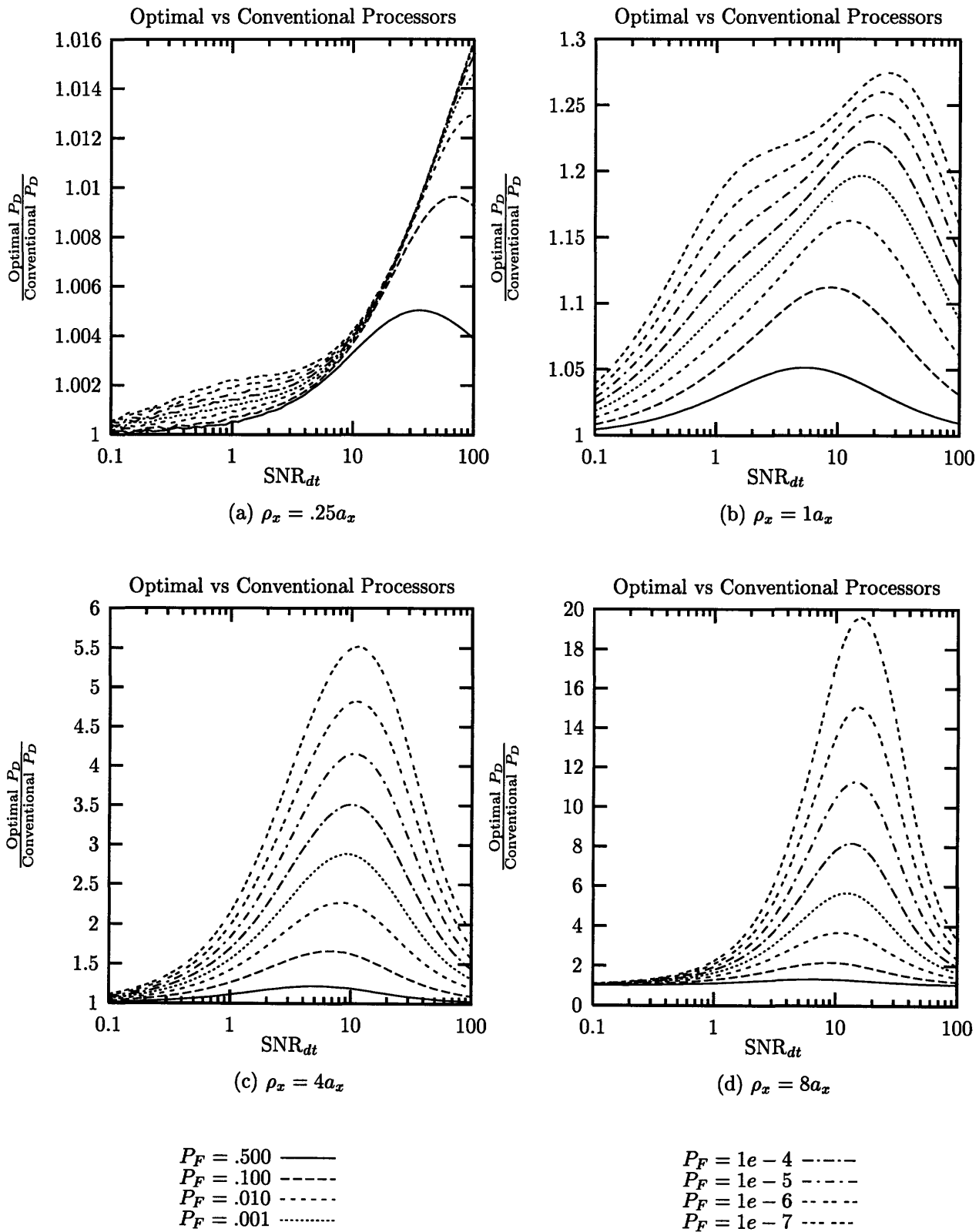


Figure 5-25: Comparison of optimal and conventional detection probabilities of a diffuse target (as a function of SNR)

5.3 Summary

In this chapter, we have explored in depth two idealized detection problems relevant to actual practice. As in all theoretical assessments, we do not expect reality to give us the benefit of all the assumptions and idealizations we made, but we hope to understand and develop intuition for the fundamental issues in actual practice through the simpler theoretical problems, and to answer some of the questions quantitatively. In particular, we shall discuss the possible inherent limitations of the conventional and the MR SAR processors via these two detection problems.

With a directional transmitted beam, the specular mirror's smooth surface gives a directional reflection, or a narrow-angle target return. This is the first way in which the conventional SAR imager is disadvantaged – it processes the signal with the full dwell time of the target (the filter has full-dwell bandwidth) and allows more noise at high chirp frequencies to degrade the signal. The MR processor can easily adapt to solve this problem by varying the integration time.

Second, the combined uniform clutter and receiver noise is colored, and neither the conventional imager or the MR processor can perform the function of the whitening filter needed in the optimal system to best combat the colored noise. This is, however, not a big issue for a large target because its return will be narrowband in frequency and essentially sees the clutter as white noise over the frequencies of interests. For a small target, the whitening effect is probably not negligible but the performance that the optimal processor gains over the MR filter due to the mismatch in the target return duration is now small. Therefore, the MR filter is sub-optimal but not very much so.

Third, a specular mirror with tilt gives rise to aspect dependence in the target return. The tilt can significantly deflect the reflected beam from the radar's line-of-sight and shifts the chirp frequency content of the return. The result is the separation of the chirp center from the intensity center of the return. The conventional imager cannot address this problem and the result is a large attenuation of the processed signal and poor detection performance. This is the biggest problem to improve upon for SAR systems with detection of specular targets in mind. The adaptive MR processor can account for this problem and is essentially optimal for a highly tilted or large mirror.

The optimal processor for diffuse target detection also depends on the size of the target as in the specular case, and the optimal scheme utilizes with the fact that a larger target decorrelates the target return. The MR processor adapts by mimicking the optimal filter as best it can, rather than simply matching the target return's duration. Due to the incoherent nature of the diffuse-target return, the performance difference between the optimal receiver and either the conventional or MR processor is generally not as significant as that for a specular mirror with tilt.

We further notice that given a fixed SNR, the target size does not affect the optimal detection probabilities of a specular mirror in the absence of diffuse clutter (5.16), but there is an optimal target size of which a diffuse target can be detected most reliably.

The performance of the conventional and the MR processor are summarized in Table 5.1. The

conventional imager is only optimal for a point or small target in all cases.

Target	Performance of conventional imager for large target	Optimal condition for adaptive MR processor
Diffuse target (without clutter)	fair	point or small target; or high false alarm probability; or low SNR_{dt}
Untilted mirror in clutter	bad	large mirror; or low clutter energy
Tilted mirror in clutter	severely poor	large mirror; or high tilt; or low clutter energy

Table 5.1: Conditions for optimality of the adaptive MR processors

We have obtained a number of exact expressions in this chapter for analyzing these two detection problems and they should serve as the foundation for future extensions on similar detection problems.

Chapter 6

Conclusion

In this thesis, we have proposed a repertoire of diffuse and specular target models, and examined their target returns in a continuous wave 1-D SAR setting. We have first seen that a multi-resolution (MR) SAR processor can exhibit certain properties in targets of interest that cannot be shown by the conventional imager. At the same time, by posing and solving two optimal detection problems, we also come to realize what fundamental shortcomings the SAR processor inherits from the structure that is derived largely from the assumption of a point scatterer.

In any case, the MR processor can be considered as a general system that can be easily implemented by extending on the architecture of the conventional imager, and can, in both detection problems we considered, improve the performance over the conventional imager significantly. It is interesting to note that in these detection problems, the MR processor adapts by best matching itself to the optimal processors, which for the diffuse target detection problem, is not the obvious means of simply matching the target return duration (which the conventional imager has already done!) The optimal integration durations used for the specular mirror and the diffuse target are different because there are inherent differences in target characteristics between the two. In both detection problems, the optimal receivers call for a shorter-than-dwell-time integration duration – an integration duration longer than the dwell time would obviously include parts of the radar return in which only the receiver noise and not the target return is present. What exactly the optimal durations are depend on the target geometry and whether the target is diffuse or specular. This motivates, at least for the single target detection problem, a system similar to the one in [15] which can be trained to recognize the different MR signatures of targets.

6.1 Directions for Future Work

For future extensions, we can work on three aspects of our research: more elaborate target models, radar models, and signature assessments.

We have examined a small number of simple reflectors by themselves and would like to construct a scenario in which a combination of these targets are present simultaneously. As discussed in Chapter 2, both specular and diffuse targets are only the extreme cases for a target and there exist composite targets with both specular and diffuse components that are yet to be explored.

We could extend our stripmap analysis to a 2-D SAR or a spotlight mode SAR system because, as one can expect, many targets should display different properties when the impinging waves of the radar come from various directions. Polarization, which we have failed to account for with our scalar wave analysis, will be a crucial factor in the actual characteristics of a dihedral because of the double-bounce nature of its reflection. In addition, radar frequency would also give the same targets different scattering properties. Perhaps optimal imaging or detection schemes of combining information from several radar systems can also be examined.

We still have to pose and solve other relevant hypotheses testing problems – such as the diffuse target in uniform clutter versus the uniform clutter itself, and specular versus diffuse targets with the uniform clutter present under both hypotheses. We could also pose and solve generalized detection and estimation problems in which the parameters of the targets are not known *a priori*. Finally, we can try applying our preliminary results to either synthesized [29] or real SAR data [11] to test their validity.

Appendix A

Gaussian-Schell Model

The Gaussian-Schell Model of coherence [19] can be used to give another interpretation of the diffuse model.

We define the degree of coherence of a target as below.

$$\mu(\bar{\rho}, \bar{\rho}_1) \equiv \frac{\langle \mathbf{T}(\bar{\rho}), \mathbf{T}^*(\bar{\rho}_1) \rangle}{\langle \mathbf{T}(\bar{\rho})\mathbf{T}^*(\bar{\rho}) \rangle^{1/2} \langle \mathbf{T}(\bar{\rho}_1)\mathbf{T}^*(\bar{\rho}_1) \rangle^{1/2}} \quad (\text{A.1})$$

It a measure of how far $\bar{\rho}_1$ has to be away from $\bar{\rho}$ to let $\mathbf{T}(\bar{\rho})$ give little information about what $\mathbf{T}(\bar{\rho}_1)$ is (or vice versa.) As a physical necessity, the coherence generally has to ultimately decrease with increasing separation between $\bar{\rho}$ and $\bar{\rho}_1$. The Schell model assumes that within a target of finite size, such a coherence function is parameterized by only the difference transverse vector $\bar{\rho} - \bar{\rho}_1$ (i.e. an extension of homogeneity for finite-size targets.) The Gaussian-Schell model further assumes that $\mu(\bar{\rho}, \bar{\rho}_1)$ is a spatial Gaussian, which forces the coherence to decay monotonically for increasing distance separation $|\bar{\rho} - \bar{\rho}_1|$.

$$\mu(\bar{\rho}, \bar{\rho}_1) = \exp\left(-\frac{|\bar{\rho} - \bar{\rho}_1|^2}{\rho_c^2}\right) \quad (\text{A.2})$$

where ρ_c is called the coherence length of the target, because the complex reflection coefficient $\mathbf{T}(\bar{\rho})$ becomes incoherent when the separation $|\bar{\rho} - \bar{\rho}_1|$ is greater than ρ_c . Now

$$\langle \mathbf{T}(\bar{\rho})\mathbf{T}^*(\bar{\rho}_1) \rangle = \langle \mathbf{T}(\bar{\rho})\mathbf{T}^*(\bar{\rho}) \rangle^{1/2} \langle \mathbf{T}(\bar{\rho}_1)\mathbf{T}^*(\bar{\rho}_1) \rangle^{1/2} \exp\left(-\frac{|\bar{\rho} - \bar{\rho}_1|^2}{\rho_c^2}\right). \quad (\text{A.3})$$

Let

$$\langle \mathbf{T}(\bar{\rho})\mathbf{T}^*(\bar{\rho}) \rangle = \mathcal{T}(\bar{\rho}), \quad \text{where } \mathcal{T}(\bar{\rho}) \geq 0 \quad (\text{A.4})$$

because the magnitude-squared of the reflection coefficient is always a positive function. Now (A.3) becomes

$$\langle \mathbf{T}(\bar{\rho})\mathbf{T}^*(\bar{\rho}_1) \rangle = \sqrt{\mathcal{T}(\bar{\rho})}\sqrt{\mathcal{T}(\bar{\rho}_1)} \exp\left(-\frac{|\bar{\rho} - \bar{\rho}_1|^2}{\rho_c^2}\right) \quad (\text{A.5})$$

In all applications, we need to observe the target terrain through some deterministic system, probably a linear system. Let us restrict ourselves to a linear space-invariant system which transforms the spatial information in $\mathbf{T}(\bar{\rho})$ to a time signal because this is what our synthetic-aperture radar system does.

$$\mathbf{l}_d(t) = \int \mathbf{T}(\bar{\rho})\mathbf{g}(t, \bar{\rho})d\bar{\rho} \quad (\text{A.6})$$

where $\mathbf{g}(t, \bar{\rho})$ is a combination of our diffraction and propagation model $\mathbf{h}_L(\bar{\rho})$ as well as the radar return processing filter $\mathbf{h}(t)$. In addition to knowing that $\mathbf{l}_d(t)$ will be zero-mean because it is integration over the zero-mean random process $\mathbf{T}(\bar{\rho})$, we are interested in the correlation function of $\mathbf{l}_d(t)$ because this is necessary for processing using classical detection and estimation theory.

$$\langle \mathbf{l}_d(t)\mathbf{l}_d^*(u) \rangle = \left\langle \int \mathbf{T}(\bar{\rho})\mathbf{g}(t, \bar{\rho})d\bar{\rho} \int \mathbf{T}^*(\bar{\rho}_1)\mathbf{g}^*(u, \bar{\rho}_1)d\bar{\rho}_1 \right\rangle \quad (\text{A.7})$$

$$= \int \int \langle \mathbf{T}(\bar{\rho})\mathbf{T}^*(\bar{\rho}_1) \rangle \mathbf{g}(t, \bar{\rho})\mathbf{g}^*(u, \bar{\rho}_1) d\bar{\rho} d\bar{\rho}_1 \quad (\text{A.8})$$

$$= \int \int \sqrt{\mathcal{T}(\bar{\rho})}\sqrt{\mathcal{T}(\bar{\rho}_1)} \exp\left(-\frac{|\bar{\rho} - \bar{\rho}_1|^2}{\rho_c^2}\right) \mathbf{g}(t, \bar{\rho})\mathbf{g}^*(u, \bar{\rho}_1) d\bar{\rho} d\bar{\rho}_1 \quad (\text{A.9})$$

Because a diffuse target fluctuates widely and randomly in surface height (over $\bar{\rho}$), the coherence length ρ_c will be very short, on the order of the transmitted wavelength. The functions $\mathcal{T}(\bar{\rho})$ and $\mathbf{g}(t, \bar{\rho})$ at any two points in space farther apart than ρ_c will give very little contribution to the integrals. At the same time, both $\mathcal{T}(\bar{\rho})$ and $\mathbf{g}(t, \bar{\rho})$ are relatively smooth functions of $\bar{\rho}$ compared to the Gaussian, so we can approximate them with their values at the middle points of $\bar{\rho}$ and $\bar{\rho}_1$.

$$\langle \mathbf{l}_d(t)\mathbf{l}_d^*(u) \rangle \approx \int \int \sqrt{\mathcal{T}(\bar{\rho}_+)}\sqrt{\mathcal{T}(\bar{\rho}_+)} \exp\left(-\frac{|\bar{\rho} - \bar{\rho}_1|^2}{\lambda^2}\right) \mathbf{g}(t, \bar{\rho}_+)\mathbf{g}^*(u, \bar{\rho}_+) d\bar{\rho} d\bar{\rho}_1 \quad (\text{A.10})$$

where

$$\bar{\rho}_+ = \frac{1}{2}(\bar{\rho} + \bar{\rho}_1). \quad (\text{A.11})$$

With the additional change of variables

$$\bar{\rho}_- = \bar{\rho} - \bar{\rho}_1 \quad (\text{A.12})$$

$\bar{\rho}_+, \bar{\rho}_-$ become the sum-and-difference coordinates to which we can transform our integration. This transformation can be easily shown to have a unit Jacobian. We find that

$$\langle \mathbf{l}_d(t) \mathbf{l}_d^*(u) \rangle \approx \int \int \mathcal{T}(\bar{\rho}_+) \exp\left(-\frac{|\bar{\rho}_-|^2}{\lambda^2}\right) \mathbf{g}(t, \bar{\rho}_+) \mathbf{g}^*(u, \bar{\rho}_+) d\bar{\rho}_+ d\bar{\rho}_- \quad (\text{A.13})$$

$$\approx \int \pi \lambda^2 \mathcal{T}(\bar{\rho}_+) \mathbf{g}(t, \bar{\rho}_+) \mathbf{g}^*(u, \bar{\rho}_+) d\bar{\rho}_+ \quad (\text{A.14})$$

Thus we realize that the end result would be approximately the same if we have replaced (A.5) with

$$\langle \mathbf{T}(\bar{\rho}) \mathbf{T}^*(\bar{\rho}_1) \rangle \approx \lambda^2 \mathcal{T}(\bar{\rho}) \delta(\bar{\rho} - \bar{\rho}_1) \quad (\text{A.15})$$

right from the start.

As a final comment, this derivation from the Gaussian-Schell model, as with any other model which contains a δ -function should be treated with care. In particular, the model only exists *in the limit* after integration because the function $\delta(\bar{\rho} - \bar{\rho}_1)$ is infinite when $\bar{\rho} = \bar{\rho}_1$.

Appendix B

Statistics for a Finite Sum of Exponential Random Variables

The objective of this appendix is to derive the density for the truncated log-likelihood ratio used in detecting a diffuse target in white receiver noise. We will also give a closed-form expression for the detection and false alarm probabilities.

The truncated log-likelihood ratio is

$$\ell(N) = \sum_{i=0}^N \ell_i \tag{B.1}$$

where ℓ_i is an exponential random variable with density

$$p_{\ell_i}(x) = \alpha_i e^{-\alpha_i x}, \quad x \geq 0 \tag{B.2}$$

That is $\ell(N)$ is a sum of N independent exponentially distributed random variables with means $\frac{1}{\alpha_i}$. Because of the independent summation, the moment generating function of $\ell(N)$ can be easily shown to be the product of the moment generating function of each individual ℓ_i [7],

$$\mathbf{M}_{\ell(N)}(s) = \int_0^{\infty} p_{\ell(N)}(x) e^{-sx} dx \tag{B.3}$$

$$= \prod_{i=0}^N \frac{\alpha_i}{s + \alpha_i} \tag{B.4}$$

For our particular interest, the α_i are distinct, or $\alpha_i \neq \alpha_j$ for $i \neq j$. We can then collect residues of (B.4) and write

$$\mathbf{M}_{\ell(N)}(s) = \sum_{i=0}^N \frac{m_i}{s + \alpha_i} \quad (\text{B.5})$$

where the residues m_i are

$$m_i = \frac{\prod_{j=0}^N \alpha_j}{\prod_{\substack{j=0 \\ j \neq i}}^N (\alpha_j - \alpha_i)} \quad (\text{B.6})$$

After taking the inverse transform of (B.5), the density of $\ell(N)$ can be concisely written as

$$p_{\ell(N)}(x) = \left(\prod_{i=0}^N \alpha_i \right) \sum_{i=0}^N \frac{e^{-\alpha_i x}}{\prod_{\substack{j=0 \\ j \neq i}}^N (\alpha_j - \alpha_i)}, \quad x \geq 0 \quad (\text{B.7})$$

Furthermore, using (B.7),

$$\Pr\{\ell(N) \geq \gamma\} = \int_{\gamma}^{\infty} p_{\ell(N)}(x) dx \quad (\text{B.8})$$

$$= \left(\prod_{i=0}^N \alpha_i \right) \sum_{i=0}^N \frac{e^{-\alpha_i \gamma} / \alpha_i}{\prod_{\substack{j=0 \\ j \neq i}}^N (\alpha_j - \alpha_i)} \quad (\text{B.9})$$

$$= \sum_{i=0}^N \left(\prod_{\substack{j=0 \\ j \neq i}}^N \frac{1}{1 - \frac{\alpha_i}{\alpha_j}} \right) e^{-\alpha_i \gamma} \quad (\text{B.10})$$

which is in a form that can be computed with good numerical stability as long as no two means α_i and α_j are too close together.

We can extend the result to handle repeated means by modifying the residue series expansion in B.5. The resulting density will be a weighted sum of exponential and erlang densities.

Bibliography

- [1] G. J. A. Bird, editor. *Radar Precision and Resolution*. John Wiley & Sons, New York, 1974.
- [2] J. K. Bounds. “The Infrared Airborne Radar Sensor Suite”. Technical Report 610, Research Laboratory of Electronics, Massachusetts Institute of Technology, December 1996.
- [3] E. Brookner, editor. *Radar Technology*. Artech, Dedham, 1977.
- [4] R. D. Chaney, A. S. Willsky, and L. M. Novak. “Coherent aspect-dependent SAR image formation”. In *SPIE Conference on Algorithms for Synthetic Aperture Radar*. SPIE, April 1994. Orlando, FL.
- [5] J. C. Curlander and R. N. McDonough. *Synthetic Aperture Radar Systems and Signal Processing*. Remote Sensing. Wiley, New York, 1991.
- [6] J. C. Dainty, editor. *Laser Speckle and Related Phenomenon*. Springer-Verlag, Berlin, 1975.
- [7] W. Feller. *An Introduction to Probability Theory and Its Applications*, volume II. John Wiley & Sons, New York, 2nd edition, 1971.
- [8] J. P. Fitch. *Synthetic Aperture Radar*. Springer-Verlag, New York, 1988.
- [9] J. W. Goodman. *Introduction to Fourier Optics*. Mc-Graw Hill, 1968.
- [10] I. S. Gradshteyn and I. M. Ryzhik. *Table of Integrals, Series, and Products*. Academic Press, London, 1965.
- [11] T. J. Green, Jr., S. Marcus, and B. D. Colella. “Synthetic-aperture-radar Imaging with a Solid-state Laser”. *Applied Optics*, 34(30):6941–6949, October 1995.
- [12] R. O. Harger. *Synthetic Aperture Radar Systems Theory and Design*. Academic Press, New York, 1970.
- [13] C. W. Helstrom. *Elements of Signal Detection and Estimation*, pages 523–530. Prentice Hall, New Jersey, 1995. Appendix C: Q-Function.

- [14] J. C. Henry. "The Lincoln Lab 35 GHz Airborne Synthetic Aperture Radar Imaging Radar System". In *IEEE National Telesystems Conference*, March 1991. Atlanta, GA.
- [15] W. W. Irving, A. S. Willsky, and L. M. Novak. "Multiresolution approach to discriminating targets from clutter in SAR imagery". *Proceedings SPIE Algorithms for Synthetic Aperture Radar Imagery II*, 2487(1):272–299, April 1995.
- [16] A. V. Jelalian. *Laser Radar Systems*. Artech House, Norwood, MA, 1992.
- [17] R. S. Kennedy. *Fading Dispersive Communication Channels*. Wiley, New York, 1969.
- [18] J. A. Kong. *Electromagnetic Wave Theory*, chapter 5, pages 388–402. Wiley, New York, 2nd edition, 1990.
- [19] L. Mandel and E. Wolf. *Optical Coherence and Quantum Optics*. Cambridge University Press, 1995.
- [20] L. M. Novak, G.J. Owirka, and C.M. Netishen. "Performance of a High-Resolution Polarimetric SAR Automatic Target Recognition System". *Lincoln Laboratory Journal – Special Issue on Automatic Target Recognition*, 6(1), Spring 1993.
- [21] D. Park. *High-Resolution Laser Radar Performance Analysis*. PhD thesis, Massachusetts Institute of Technology, January 1988.
- [22] R. K. Raney. "Transfer functions for partially coherent SAR systems". *IEEE Transactions on Aerospace Electronic Systems*, 19(5):740–750, 1983.
- [23] R. K. Raney. "Theory and Measure of Certain Image Norms in SAR". *IEEE Transactions on Geoscience and Remote Sensing*, GE-23(3):343–348, 1985.
- [24] J. H. Shapiro. "Target Reflectivity Theory for Coherent Laser Radars". *Applied Optics*, 21(18):3398–3407, September 1982.
- [25] J. H. Shapiro, B. A. Capron, and R. C. Harney. "Imaging and Target Detection with a Heterodyne-Reception Optical Radar". *Applied Optics*, 20(19):3292–3313, October 1981.
- [26] M. Skolnik, editor. *Radar Handbook*. McGraw-Hill, New York, 1970.
- [27] H. L. Van Trees. *Detection, Estimation and Modulation Theory*. Wiley, New York, 1971. Part III: Radar-Sonar Signal Processing and Gaussian Signals in Noise.
- [28] H. L. Van Trees. *Detection, Estimation and Modulation Theory*. Wiley, New York, 1971. Part I: Detection, Estimation, and Linear Modulation Theory.

- [29] P. W. Vachon, R. K. Raney, and W. J. Emery. "A simulation for spacebourne SAR imagery of a distributed, moving scene". *IEEE Transactions on Geoscience and Remote Sensing*, 27(1):67–77, January 1989.
- [30] S. M. Verbout, W. W. Irving, and A. S. Hanes. "Improving a Template-Based Classifier in a SAR Automatic Target Recognition System by Using 3-D Target Information". *The Lincoln Laboratory Journal*, 6(1):53–, 1993.
- [31] J. G. Verly. "Physical Optics Polarization Scattering Matrix for a Right-Angle Dihedral". Technical Report 1008, Lincoln Laboratory, February 1995.